CURRENT ESTIMATION AND PATH FOLLOWING FOR AN AUTONOMOUS UNDERWATER VEHICLE BY USING A MODEL-BASED NONLINEAR OBSERVER

by

Eonjoo Kim
B.E. (Hons) in Marine Offshore Engineering
University of Tasmania,2015

Submitted in fulfilment of the requirements
for the Degree of Doctor of Philosophy
in Maritime Engineering

National Centre for Maritime Engineering and Hydrodynamics
Australian Maritime College (AMC)
University of Tasmania

March, 2021

Declaration of Originality

I declare that this thesis contains no material which has been accepted for a degree or diploma by the University or any other institution, except by way of background information and duly acknowledged in the thesis, and that, to the best of my knowledge and belief, this thesis contains no material previously published or written by another person, except where due acknowledgement is made in the text of the thesis.

Signed: ______________________________
Eonjoo Kim

Date: 26/03/2021

Statement regarding published work

Signed: ______________________

Eonjoo Kim

Date: 26/03/2021

Statement of Co-Authorship

The following people and institutions contributed to the publication of work undertaken as part of this thesis:

- Eonjoo Kim, Australian Maritime College/University of Tasmania,(**Candidate**).
- Prof. Dr. Neil Bose, Memorial University, Newfoundland, (**Author 1**).
- Dr. Hung Nguyen, Australian Maritime College/University of Tasmania, (**Author 2**).
- Dr. Shuangshuang Fan, School of Marine Sciences, Sun Yat-sen University, (**Author 3**).

Chapter 2

- Paper 2 - E. Kim, S. Fan, and N. Bose, Estimating Water Current Velocities by Using a Model-Based High-Gain Observer for an Autonomous Underwater Vehicle, *IEEE Access Journal*, 2018, [1].

Candidate was the primary author who conducted the design and analysis of the work while all co-authors assisted with refinements and presentation.
[Candidate: 80%, Author 1: 10%, Author 3: 10%]

Chapter 3

- Paper 1 - E. Kim, S. Fan, and N. Bose, Autonomous Underwater Vehicle Model-Based High-Gain Observer for Ocean Current Estimation, *2018 IEEE/OES Autonomous Underwater Vehicle (AUV) Workshop*, 2018, [2].

Candidate was the primary author who conducted the design and analysis of the work while all co-authors assisted with refinements and presentation.
[Candidate: 80%, Author 1: 10%, Author 3: 10%]

Chapter 4

- Paper 3 - E. Kim et al, Path Following for an Autonomous Underwater Vehicle (AUV) by Using a High-Gain Observer based on an AUV Dynamic Model", *IFAC-PapersOnLine*, 2019, [3].

Candidate was the primary author who conducted the design and analysis of the work while all co-authors assisted with refinements and presentation.
[Candidate: 70%, Author 1: 10%, Author 2: 10%, Author 3: 10%]

- Paper 4 - E. Kim et al. Current Estimation and Path Following for an Autonomous Underwater Vehicle (AUV) by Using a High-Gain Observer Based on an AUV Dynamic Model, *International Journal of Control, Automation and Systems*, 2020, [4].

Candidate was the primary author who conducted the design and analysis of the work while all co-authors assisted with refinements and presentation.
[Candidate: 70%, Author 1: 10%, Author 2: 10%, Author 3: 10%]

Signed: ____

Dr. Hung Duc Nguyen, Primary Supervisor
Australian Maritime College,University of Tasmania

Signed: ____

Dr. Neil Bose, Co-Supervisor
Memorial University of Newfoundland

Signed: ____

Dr. Shuangshuang Fan, Academic advisor
School of Marine Sciences, Sun Yat-sen University

We, the undersigned, endorse the above stated contribution of work undertaken for each of the published (or submitted) peer-reviewed manuscripts contributing to this thesis:

Signed: ______________________ Date: 26/03/2021

Eonjoo Kim
Candidate
Australian Maritime College, University of Tasmania

Signed: ______________________ Date: 26/03/2021

Dr. Hung Duc Nguyen
Primary Supervisor
Australian Maritime College, University of Tasmania

Signed: ______________________ Date: 26/03/2021

Dr. Vikram Garaniya
Director
National Centre for Maritime Engineering and Hydrodynamics,
Australian Maritime College, University of Tasmania

ABSTRACT

The objective of this thesis is to contribute to Autonomous Underwater Vehicle (AUV) navigation by estimating the prevalent ocean currents and improving the path following guidance system. The Inertial Navigation System (INS) based localisation solution is vulnerable to uncertainties derived from double integration of the inherent errors within the INS acceleration measurements. This can be aided by the velocity measurement using the Doppler Velocity Log (DVL), but DVL aid is unavailable when the distance between the AUV to the seabed is larger than the DVL range. However, the vehicle's velocity can be estimated by a model-aided observer which predicts a dynamic motion response of the vehicle. The benefits from using a more precise AUV model is compelling as the application of underwater vehicles expand into more complicated and harsher environments.

In terms of the AUV motion model, however, the effect of current on the vehicle dynamics is often ignored when the AUV motion model is used for control, navigation and estimation. As a solution for this, an AUV dynamic model-based, nonlinear observer design is introduced, which is complemented with the development of an AUV dynamic model in nonuniform and unsteady current and the high-gain observer (HGO). The gain for the HGO is obtained by solving a Linear Matrix Inequality (LMI) representing the estimation error dynamic. The HGO is a robust tool for observer design and well-used in nonlinear feedback control, which has been studied for several decades. Motivated by the design method of the HGO, the current disturbance is considered as the uncertainties of the vehicle dynamic system, and current velocity is estimated in an indirect way. The current velocity is determined by calculating the differences between the vehicle velocities over the ground and the vehicle velocities through the water estimated by the model-based observer. The HGO based on the AUV dynamic model established in this research was validated using experimental data from a set of field manoeuvres using a Gavia class AUV and the performance was compared against other commonly used navigation methods.

In terms of the path following problem, an accurate path following guidance system plays an important role for an AUV in oceanic surveys and exploration. The path-following guidance system includes a guidance law, an update law and a proportional and integral controller. This thesis presents a three-dimensional path following guidance logic which ensures the vehicle path converges into the predefined desired path. The desired straight and curved path are represented by using a Serret-Frenet frame which propagates along the curve. The path-following guidance system, 'PPNAPG (Pure Proportional Navigation and Pursuit Guidance)' is developed by combining the pure proportional navigation guidance (PPNG) law and pursuit guidance (PG) law, which are widely used in the missile community. The performance of the proposed path-following guidance system, PPNAPG is validated via both simulation and experiment using the MUN (Memorial University of Newfoundland) Explorer AUV.

One of the primary benefits of the nonlinear observer based on the AUV dynamic model and the path following guidance system is that it could be employed on any type of AUV platforms without any elaboration. Furthermore, the proposed techniques require no additional sensors beside the typically available AUV navigation sensors such as global positioning, accelerometers and gyroscopes in the Initial Measurement Unit (IMU).

Overall, this thesis suggests that the nonlinear observers based on an AUV dynamic model and the PPNAPG is an effective combination to estimate and compensate for the current and complete a path-following mission. These outcomes and methods enable other researchers and students in the field of AUV control and navigation systems to adapt and extend the methods to other AUV models without using an ADCP to measure the current. The insight gained from this study can also be of assistance to an oceanographic mission by optimising the guidance law to reduce mission completion time.

ACKNOWLEDGMENTS

First and foremost, I would like to express my sincere gratitude to my supervisors Prof. Neil Bose, Dr. Shuangshuang Fan and Dr. Hung Nguyen for their continuous support for my PhD research. Their expert guidance, practical advice and not to mention friendly company have been very precious throughout all stages of the study. I have no doubt that any of this challenging journey would not have been successful without them.

Secondly, I would like to thank Craig Bulger, Gina Miller, Bo Thanyamanta, Yaomei Wang and Xi Chen from Memorial University of Newfoundland in Canada not only for their enormous support for the MUN Explorer AUV sea test but also for the warm company in an unfamiliar country. A special recognition must be made to Dr. Supun A. T. Randeni P. for his helpful academic advice and resources as a colleague who inspired and enlightened me at the beginning of my research. Also, I adorably thank my colleagues at AMC who were not only co-workers, but also good friends who shared a meaningful moment and supported each other through the toughest times at AMC.

A special thanks to my family. I express my thanks to my sister Myunghee, and brother Jeayoon for their selfless love, care and dedicated effort which contributed a lot for completion of my thesis. I owe thanks to a very special person, my fiancé, Steffen for his continued and unfailing love, support and understanding during my pursuit of the Ph.D. degree that made the completion of my thesis possible. I greatly value his contribution and deeply appreciate his belief in me. Finally, I acknowledge the people who mean a lot to me, my parents, Sangwoo and Guiyoung, for showing faith in me and giving me liberty to choose what I desired. I would never be able to pay back the love and affection they show to me. I dedicate this thesis to my mom and dad.

Contents

List of Tables

List of Figures

ACRONYMS

ADCP	acoustic Doppler current profiler
AUV	autonomous underwater vehicle
CFD	computational fluid dynamics
DOF	degrees of freedom
DVL	Doppler velocity log
EKF	extended Kalman filter
GNC	guidance, navigation and control system
GPS	global positioning system
HGO	high-gain observer
ILOS	integral line-of-sight
IMU	initial measurement unit
INS	inertial navigation System
ISE	International Submarine Engineering Ltd.
LAUV	long range AUV
LBL	long base line system
LMI	linear matrix inequality
LOS	line-of-sight
MUN	Memorial University of Newfoundland
PEM	prediction error method (PEM) optimisation techniques
PF	particle filter
PG	pursuit guidance law
PPNAPG	pure proportional navigation and pursuit guidance
PPNG	pure proportional navigation guidance law
RLS	recursive least squares method
SCC	surface control console
UKF	unscented Kalman filter
USBL	ultra short base line system
VCC	vehicle control computer
VF	vector field guidance law

Chapter 1

Introduction

1.1 Background

An autonomous underwater vehicle (AUV) is a specific robotic platform with a certain degree of autonomy [5]. The usage of AUVs is rapidly increasing thanks to the thriving needs of commercial, military and scientific organisations [6]. AUVs are used for underwater tasks that range from surveys, inspection of submerged structures (e.g., pipelines), searching for downed aircraft, tracking oceanographic features, laying undersea cables, undersea mapping, and finding mines, to name a few [7].

Oceanic survey measurements need both accurate sensing technology and localisation. In other words, a measurement only has value if its time, location and orientation are accurately known. When using AUVs to conduct such measurements, it is very important to have accurate knowledge of position and orientation to be temporally synced with each acquired measurement. Inaccurate localisation could result in the vehicle travelling away from the pre-planned mission route while assuming it is on the correct track, thereby resulting in an incorrectly geo-located dataset and a compromised mission. In the most severe examples of this, mission failure could result leading to a potentially damaged or lost AUV.

However, meeting these requirements is formidable to achieve since traditional methods of localisation rely on the global positioning system (GPS) which is unavailable underwater due to the high attenuation of electromagnetic signals in water [8].

One of the conventional underwater localisation methods is to triangulate the position of an AUV using acoustic triangulation; i.e., using a Long Base Line (LBL) system or Ultra Short Base Line (USBL) system [9]. LBL systems are one of the most accurate and precise localisation techniques, but the range of an LBL beacon is limited. As a result, an array of the devices is required for a long range AUV operation. Furthermore, LBL systems demand surface vessel support and deployment of moored equipment, which make it a less favoured option for AUV localisation, especially for deep water offshore operations [10]. USBL systems have been increasingly used in last decade, but they require a dedicated supporting vessel at the surface to keep the AUV in range throughout its mission, which is a major drawback.

A motion control system for the marine vehicle is usually constructed as three independent blocks denoted as the guidance, navigation and control (GNC) system [11]. These systems interact with each other via data and signal transmission as illustrated in Figure 1.1. The guidance, navigation and control (GNC) system of autonomous underwater vehicles studied in this thesis focuses on the state observer and the path-following guidance system in an attempt to estimate and thereafter compensate for the current.

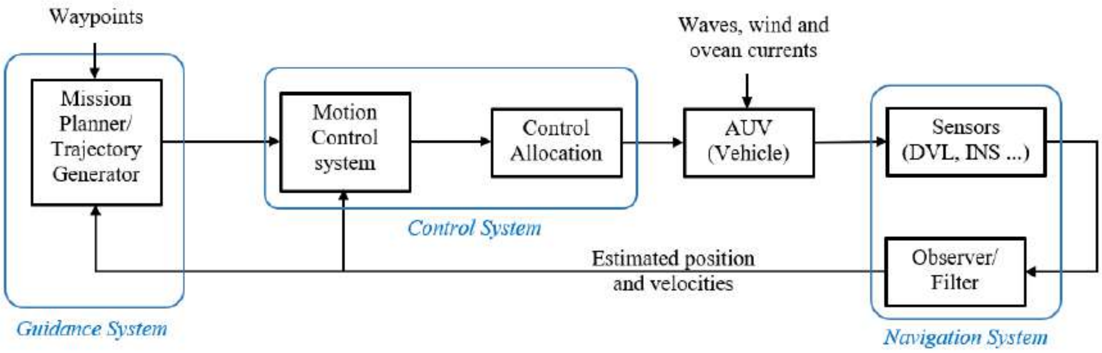

Figure 1.1: *Guidance, navigation and control* (GNC) system signal flow [11].

Guidance is the action or the system that continuously conputes the reference (desired) position, velocity and acceleration of the vehicle to be used by the motion control system. These data are usually provided to the human operator and the navigation system.

Control system is the action of determining the necessary control forces and moments to be provided by the vehicle in order to satisfy a certain control objective. The desired control objective is usually seen in conjunction with the guidance system.

Navigation system is the science of directing a vehicle by determining its position, attitude, course and distance travelled. An Inertial Navigation System (INS) is one of the most generally used instruments for AUV localisation and navigation. The linear accelerations and angular rates of the vehicle relative to inertial space are measured by the accelerometers and gyroscopic sensors of the Inertial Measurement Units (IMUs) within the INS [12]. Consequently, the measurements from the IMU are integrated to calculate the velocity, attitude and position of the vehicle, but IMU measurements include uncertainties induced by inherent errors of their sensors. Therefore, an unbounded drift is accumulated in the position and velocity solutions as time goes by. This can be solved by updating the true position and/or velocity measurement of the vehicle from the INS position estimate via a predictor-corrector model such as a Kalman filter [13]. To prevent this position drift in the INS, the vehicle velocity measurements from a Doppler Velocity Log (DVL) with a bottom-tracking mode are generally used to aid the INS localisation solution.

However, when the distance between the AUV to seabed is greater than the DVL range, DVL aid is unavailable, which leads to increased localisation error. Also, the large physical size and high cost of the DVL make them unsuitable for the small and portable AUVs.

The AUV's velocity can be estimated by a model-aided INS which predicts the dynamic motion response of the vehicle consisting of the mass, hydrostatics and hydrodynamic properties. The advantages of a model-aided INS is that no additional sensor is required besides a typical AUV navigation payload and it can be easily built into the vehicle's firmware with a relatively minor modification.

Even though the localisation from the model-aided INS is not as precise as the DVL-aided INS, its accuracy is higher than an unaided INS and the water-track mode DVL-aided (or ADCP-aided) INS. The capacity of the AUV motion model to predict the velocity depends greatly on the accuracy of the parameters representing the AUV characteristics that mostly differ from the vehicle configuration and ballast condition.

1.2 Problem Definition

In terms of the AUV motion model, however, the effect of current on the vehicle dynamics is typically ignored when the AUV motion model is used for control, navigation and estimation [14].

It is crucial to consider time-varying and non-uniform currents when modelling AUV motion because underwater vehicles often operate in currents and conditions which can lead to problems with dynamic positioning and tracking of AUVs. The report on the Theseus campaign [15] tells the story of the Canadian-made AUV that completed a record-breaking under-ice mission off the northern coast of Ellesmere Island in the spring of 1996. During Project Spinnaker, which was a joint Canada-US defence project, Theseus encountered a significant crosscurrent one kilometre from First Base. Theseus was trying to get back onto its line as the northeastward current was pushing the vehicle off to the right. Ultimately, the path-following controller failed and the Mission Executor switched to Homing. Then the homing controller began a hard right turn to compensate for the half-knot crosscurrent. The lesson here is that it is important to consider the impact of currents during a mission and to carefully consider the expected range of speeds and direction. Although the consideration of time-varying and nonuniform currents for an AUV dynamic model is important for control and navigation, the full verification of such conditions was outside the scope of this study due to limited resources. Accordingly the case study only focused on nonuniform currents. In this work, an exponential observer for the current was developed to provide current disturbance information for control compensation. However, the observer was derived at only the kinematic level while the current was considered as constant.

As applications of AUVs broaden to more dynamic and constrained environments such as shallow, coastal areas, more explicit dynamic models for control and estimation have compelling advantages. With a more precise dynamic model for an underwater vehicle in currents, more current flow characteristics can be identified by an observer. The current information identified in this way can improve the navigation accuracy and enhance the control performance, which ultimately lead to higher quality data for the ocean scientist.

1.3 Objectives and Research Question

This project aims to improve the localisation and navigation accuracy in AUV operations by estimating the prevalent ocean current based on the AUV's dynamic model and by designing an advanced guidance system for the task of path following. Thus, the specific research question for this project is:

"How can nonlinear observers be used to enhance the localisation of AUVs and can guidance systems be improved for the path-following tasks?"

In order to answer the overall research question, the thesis is going to answer the breakdown research questions corresponding to the published papers and thesis chapters as follows:

- How is a dynamic model of AUV developed using online system identification algorithm and used for an observer algorithm design? (Chapter 2)
- How can the high-gain observer based on AUV dynamic model be used to estimate unsteady and non-uniform current and compensate AUV motion? (Chapter 3)
- How can the path-following guidance system be extended to achieve an AUV 3D path-following in unsteady and non-uniform current with combination of current observer? (Chapter 4)
- How to evaluate and validate the performance of the proposed AUV guidance systems and the extended Kalman fiter for current estimator? (Chapter 5)

1.4 Methodology

The methodology utilised to solve the research question of this project was broken down into four main phases:

- Phase 1: Conducting a study on existing nonlinear observer applications in underwater vehicles and on AUV dynamic models in ocean currents.
- Phase 2: To validate the feasibility of the high-gain observer based on an AUV dynamic model by using the Gavia class AUV. This process involved:
  - Introduction of a Recursive Least Squares (RLS) method to identify the hydrodynamic coefficients of the Gavia AUV for a simulation model.
  - Incorporating the identified AUV model with the high-gain observer to estimate ocean currents and validate the accuracy by comparing the estimate with the measured current.
- Phase 3: Establishing a methodology to estimate ocean currents using the high-gain observer based on the AUV's dynamic model in currents. This process involved:
  - Development of an AUV dynamic model in currents in terms of the vehicle's relative velocity.
  - Introduce the high-gain observer based on the AUV's dynamics motion model in currents by using LMI to solve the error dynamic system.
- Phase 4: To enhance the performance of the path-following guidance system by using a 'Pure Proportional Navigation and Pursuit Guidance (referred to as the 'PPNAPG'), and by carrying out the following sub tasks for further evaluation:
  - Development of a dynamic model of the MUN (Memorial University of Newfoundland) Explorer AUV to establish a simulator.
  - Introduction of the "Pure Proportional Navigation and Pursuit Guidance (PPNAPG)' system.
  - Validation of the developed AUV model and guidance system by carrying out open water testing.

1.5 Novel Aspects of the Research

The novel aspects of this research are derived from the usage of the nonlinear observers based on the AUV dynamic model for the current estimation from the underwater vehicle and the improved guidance system that combines the pure proportional navigation and pursuit guidance system. The research has explored the feasibility of application of a nonlinear observer on an underwater vehicle and the results can be categorised as:

1. This is a pioneering study where for the first time the high-gain observer was applied to an underwater vehicle with the observer gain obtained by solving the LMI (linear matrix inequality) which represented the estimate error dynamics. Previous studies have developed a linear observer based on glider dynamics in currents, but the non-linear dynamics of the vehicle have been lost in the linear observer, which results in a discrepancy between the true and the estimated flow gradients [16]. The novelty of this work is that the high-gain observer based on the AUV dynamic model in currents is developed to increase the accuracy of the estimated results.

2. In the missile community, the pure proportional navigation guidance (PPNG) law and Pursuit guidance (PG) law have been widely used to focus on an enemy target [17]. This study is the first instance where a combination of the PPNG law and PG law has been used for an underwater vehicle guidance system to improve the performance of a path-following mission.

3. An AUV numerical model is required to develop and validate the feasibility and capability of the developed high-gain observer and the proposed PPNAPG system. Therefore, the final original contribution of this research is to develop the AUV numerical model using both a RLS (Recursive Least Square) based system identification method and the 'component-build-up' method. The numerical model can be used to accurately determine the relative velocity of the vehicle and ultimately estimate the ocean current velocities.

1.6 Scope and Limitation of Project

This section is to identify and acknowledge the scope and limitations of this project. The scope of this study is

1. To develop a high-gain observer based on AUV's dynamic model,

2. To develop an AUV's dynamic model for different AUVs, and

3. To develop a PPNAPG based path following algorithm.

The limitation of this study is following as:

- Since chapter 2 to 4 are based on the publication, there are duplicated parts for formulating the vehicle model and the high-gain observer.
- Due to the accessibility of the AUV model by the time of the research, three different AUV models were used in this thesis as shown in Table 1.1.
- Design of the controller is not scope of this study and the PID controller was used in the simulators.

Table 1.1: AUV models used in the thesis

Chapter	AUV Model	Usage
2	Gavia	The simulator was developed by using system identification approach based on the previous experiment data.
3 and 4	Dolphin	The simulator was developed by using the known hydrodynamic parameters.
5	MUN Explorer	The AUV was used for the experiment and the simulator was developed based on the hydrodynamic parameters.

1.7 Outline of Thesis

This thesis consists of four published scientific papers which follow a structure as outlined below.

Chapter 1: Thesis introduction

Chapter 1 is the preface of this thesis that details the motives for the project, providing necessary background knowledge on AUVs and the problem statement. Subsequently, the project objectives, methodology and the novel outcomes are defined. Chapter 1 also outlines the structure of the thesis, linking together the succeeding chapters that are comprised from academic papers.

Chapter 2: System Identification for the AUV Dynamic Model and Current Estimation by a Model-Based High-Gain Observe
(published in the journal 'IEEE Access, 2018')

This chapter presents a real-time model identification algorithm to identify the nonlinear parameters of the AUV model by utilizing a recursive least squares method. The realtime model identification algorithm allows the AUV model to be continuously updated in response to the operational environment. Furthermore, a high-gain observer based on an AUV dynamics model was introduced to estimate 3D water current velocities. The water current velocities were determined by calculating the differences between the vehicle velocities over the ground measured by a Doppler velocity log-aided inertial navigation system and the vehicle velocities through the water estimated by the model-based observer. Modelling and field trials of a Gavia AUV were used to demonstrate the approach.

Chapter 3: AUV Model-based High-gain Observer
(published in the proceedings of the '2018 IEEE/OES Autonomous Underwater Vehicle Workshop (AUV)')

Chapter 3 presents the high-gain observer based on the AUV dynamic model to obtain the vehicle's velocity relative to the water and estimate the ocean current velocities. While the AUV model was identified using system identification in Chapter 2, the simulator of the Dolphin II AUV in this chapter was created using known hydrodynamic parameters to verify the performance of the proposed observer with the ocean current assumed to be non-uniform. The magnitude of the current velocities was decided from the difference between the vehicle's absolute velocities and the relative velocities estimated by the model-based HGO. The observer gain for the HGO was determined by solving the Linear Matrix Inequality (LMI) describing the estimate error dynamics. By adapting the AUV model-based HGO, the vehicle's relative velocity was estimated, then the current velocity vector was subsequently calculated.

Chapter 4: Path Following for an AUV by Using a High-Gain Observer based on an AUV Dynamic Model
(published in the journal 'International Journal of Control, Automation and Systems' and 'IFAC-PapersOnLine')

A path following problem for AUVs in a nonuniform current is presented in this chapter. A dynamic model of an AUV in a nonuniform flow was adopted to develop a HGO for estimation of the three-dimensional current velocities along the AUV trajectories. The HGO was chosen as a nonlinear estimation algorithm, and the observer gain was computed by solving a Linear Matrix Inequality (LMI) which represented the estimation error dynamics. The current velocities were determined by calculating the differences between the measured absolute velocities of the vehicle and the estimated relative velocities of the vehicle estimated by the observer. For the path following study, the desired curved path was represented by using a Serret-Frenet frame which propagated along the curve. Two cases of numerical simulations were conducted to verify the performance of the path following system combined with the HGO for current compensation.

Chapter 5: Ocean Current Estimation and Design of Path Following Guidance Logic: Simulation and Field Testing

This chapter introduces the 'PPNAPG (Pure Proportional Navigation And Pursuit Guidance)' system for the AUV path following problem. In order to verify the capability of the PPNAPG, both simulation and open water tests were carried out with the MUN Explorer in 2019 in contribution to this thesis. Firstly, the MUN Explorer's dynamic model was built using the component build-up method. A reliable hydrodynamic model is one that can closely predict or reproduce actual operational vehicle scenarios. Thus, it is necessary to conduct sea trials to collect open water experimental data from a real vehicle to validate the model. Secondly, the proposed guidance system combines the pure proportional navigation guidance (PPNG) law and pursuit guidance (PG) law. The performance of the PPNAPG guidance system was quantitatively validated by analysing the cross-track error compared with the counterparts from the experiment.

Chapter 6: Summary, Conclusions and Future work

The closing chapter provides an overall summary of the project, bringing together the outcomes of the individual chapters. It also provides conclusions on the key findings and outcomes. Recommendations for future work are detailed in this section.

Chapter 2

System Identification for the AUV Dynamic Model and Current Estimation by a Model-Based High-Gain Observer

This chapter is based on the journal article 'Estimating Water Current Velocities by Using a Model-Based High-Gain Observer for an Autonomous Underwater Vehicle' published in the journal '*IEEE Access*'. The citation for the article is:

E. Kim, S. Fan, and N. Bose, Estimating Water Current Velocities by Using a Model-Based High-Gain Observer for an Autonomous Underwater Vehicle, *IEEE Access Journal*, 2018, [1].

For accurate control and navigation of an AUV it is critical to know the water current velocities around the vehicle body. The AUV-onboard acoustic doppler current profilers are unable to measure the current near to the vehicle due to their blanking distance, so an AUV model-based observer can serve the purpose of estimating the current velocities surrounding the vehicle. In this chapter, a high-gain observer based on an AUV dynamics model was used to estimate 3D water current velocities. The water current velocities were determined by calculating the differences between the vehicle velocities over the ground measured by a Doppler velocity log-aided inertial navigation system and the vehicle velocities through the water estimated by the model-based observer. Modelling and field trials of a Gavia AUV were used to demonstrate the approach. This chapter presents a real-time model identification algorithm to identify the nonlinear parameters of the AUV model by utilizing a recursive least squares method. The realtime model identification algorithm allows the AUV model to be continuously updated in response to the operational environment. A high-gain observer was chosen as a nonlinear estimation algorithm to obtain the vehicle velocities through the water, and the Lyapunov stability of the estimation error dynamics was investigated. The observer gain was computed by solving the linear matrix inequality which represented the error dynamics. By utilizing the observer in the AUV dynamic model, the vehicle's velocity vector through the water was estimated, then the current velocity vector was calculated. The results showed that the current estimation found by using the model-based observer was improved compared with the previous water current estimation method, which found the water velocity components in a turbulent water column from the AUV motion response.

2.1 Introduction

AUVs have been used as specialised tools for ocean missions such as seabed observation, environmental monitoring and oceanographic measurement. These tasks involve high-resolution, georeferenced optical/acoustic ocean floor mapping as well as water column sampling such as currents, temperature and salinity [18]. Georeferencing is critical for AUVs to register navigational information and to revisit a previous mission site. Since the 1970s, the navigation and control subsystems of AUVs have been progressively and continuously improved. One of the major challenges is to achieve accurate localisation and navigation in regions where the DVL is out of range of the bottom [19].

Inertial navigation systems (INS) are one of the essential pieces of equipment used to localise and navigate AUVs. By utilising an Inertial Measurement Unit (IMU), the INS estimate the position, orientation and velocity of the vehicle relative to the inertial frame. However, a navigational system based solely on an INS has a relatively large position error drift and this can be reduced through an externally aided bottom tracking DVL [20]. Furthermore, DVL aiding is either intermittently or completely unavailable when the vehicle-to-seabed distance is larger than the transmission range of DVL's acoustic frequency as illustrated in Figure 2.1. In this case, the vehicle's velocity can be approximated using a mathematical model which characterises the hydrostatic and hydrodynamic properties of the AUV; i.e. a model-aided INS [21]. Even though the localisation from the model-aided INS is not as precise as the DVL-aided INS, its accuracy is higher than an unaided INS and the water-track mode DVL-aided INS [22]. Therefore, this chapter presents an approach to estimate the vehicle's velocity by using an AUV model-based observer for the case when the vehicle operates in the midwater zone or loses the bottom track due to very rough bathymetry in deep water.

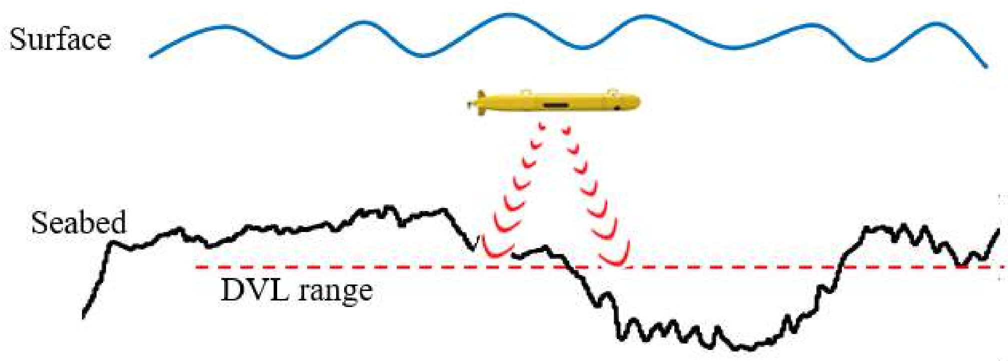

Figure 2.1: Illustration of an AUV temporarily operating beyond the DVL range.

The capability of a mathematical model for predicting AUV velocity depends on the accuracy of the parameters representing hydrodynamic, hydrostatic, environmental and external forces and the mass properties of the AUV. Since the hydrodynamic forces acting on AUVs are highly nonlinear, mathematical models should have high-order hydrodynamic coefficients to represent these nonlinear characteristics. Numerous methods for identifying linear and nonlinear hydrodynamic coefficients have been introduced for marine vehicles. For example, captive model experiments [23], computational fluid dynamics (CFD) simulation [24] and system identification utilising field experiment data [25].

In many cases it is necessary or useful to have a model of the system with the model coefficients available on-line in real time while the system is in operation. The model coefficients should be obtained based on the observations up to the current time. The on-line computation of the model coefficients must also be done in such a way that the processing of the measurements from one sample can be completed during one sampling interval. Otherwise the model computations cannot keep up with the information flow. Identification techniques that comply with this requirement will be called recursive identification methods, since the measured input-output data are processed recursively (sequentially) as they become available

[26].

The linear and nonlinear parameters of an AUV motion response prediction mathematical model are presented here by utilising the Recursive Least Squares (RLS) and the prediction error method (PEM) optimisation techniques in [19]. The difference between velocity prediction uncertainties of the models identified using the Recursive Least Squares (RLS) and PEM are negligibly small. That is, both identification algorithms are equally capable of estimating the parameters of the model. The determined velocities were used to aid the INS position estimate using a Kalman filter data fusion algorithm when external aiding was unavailable. The model is able to estimate the position of the AUV within an uncertainty range of around 1.5 % of the distance travelled, significantly improving the localisation accuracy.

In addition to the prediction of the motion response, an AUV's mathematical model can also be used to calculate the water velocity components of a turbulent water column in three dimensions using the AUV's motion response [27]. The water column velocities are determined by calculating the differences between the motion responses of the vehicle in calm and turbulent water environments. In [27], the calculated water column velocity components show good agreement with the current measurements from an ADCP mounted on the AUV.

In practice, perfect observation of the system state is unavailable, as either it is costly, technically unfeasible, or the measurement quality is low. Therefore, there is a need for a systematic approach for the evaluation or estimation of the system state using the information available. For a linear system, the idea that a stabilising controller can consist of a state estimator plus state feedback, called the separation principle, is a valid approach. However, for a nonlinear system, the separation principle does not hold since it is nearly impossible to estimate the error dynamics. Hence many nonlinear estimation algorithms have been developed such as the extended Kalman Filter (EKF) [28], unscented Kalman filter (UKF) [29], particle filter (PF) [30] and high-gain observer [31].

The high-gain observer distinguishes itself from other methods by its simple structure since it only consists of a copy of the system dynamics with a corrective term involving the product of the output observation error by the observer gain. As a result high-gain observers have been used extensively in the feedback control design for nonlinear systems; see Khalil and Praly [32] for example. The high-gain observer not only recovers stability achieved under state feedback, but also recovers its performance in the sense that the trajectories of the system under output feedback, approach those under state feedback as the observer gain increases [33] [34].

As ocean current or water column information might enhance navigation precision and control performance, current velocities were estimated by a nonlinear observer based on the AUV dynamic model in a current by Fan, et al. [18]. In the AUV dynamic model, the current was assumed to be composed of unsteady and nonuniform components. While the current disturbances were taken as the uncertainties of the vehicle dynamic system, a nonlinear observer was used to estimate the unmeasured state, which was fed back to the control system. However, as the most critical parameter, the observer gain matrix in [14] is preliminarily optimized by utilising the pole placement method to place the eigenvalues of the closed-loop system in some desired regions of the complex plane, it is inferred that there is enormous room to improve the robustness and precision of the observer by adopting advanced algorithms to optimize the observer gain matrix.

The issue of selecting a high gain arises from the demand of accounting for the nonlinearities in the error dynamics which are typically represented as a Lipschitz function. Alessandri and Rossi [35] present a time-varying increasing-gain observer for a nonlinear system. In the first time instant, the gain is small, but it increases over time up to its maximum value and then is kept constant. The selection of design parameters is produced by solving a set of the LMI.

LMI theory has recently gained great attention since a wide variety of control problems can be reduced to a few standard convex optimization problems including LMIs. Consequently, optimisation problems with convex objective functions and LMI constraints are solvable relatively efficiently with off-the-shelf software. The form of an LMI is very general. Linear inequalities, convex quadratic inequalities, matrix norm inequalities, and various constraints from control theory, such as Lyapunov and Riccati inequalities, can be all be written as LMI. Thus, LMIs are a useful tool for solving a wide variety of optimisation and control problems [36], so LMI was adapted in this chapter to obtain a gain for the observer design.

This chapter presents a real-time system identification algorithm to determine the nonlinear parameters of an AUV dynamic model utilising the RLS. The identified real-time dynamic model coefficients allowed the AUV model to keep up with the information flow and to be continuously updated in response to the operational environment. Moreover, the high-gain observer based on the AUV dynamic model was developed to estimate the vehicle velocities through the water flow which were only intermittently unavailable from the DVL when the vehicle was operating in the midwater zone. The current velocities were consequently determined by using the estimated vehicle velocities through the water flow which let the AUV control and navigation system know the current velocities around the vehicle body.

This chapter is organised as follows: Section 3.2 is devoted to clarify the methodology including the details of the instrumentation, AUV dynamics modelling and high-gain observer development. Results are presented in Section 3.3 and conclusions in Section 3.4.

2.2 Methodology

The water current velocity can be obtained from the difference between the vehicle velocity over the ground and the vehicle velocity through the water as illustrated simply in 1-D in Figure 2.2.

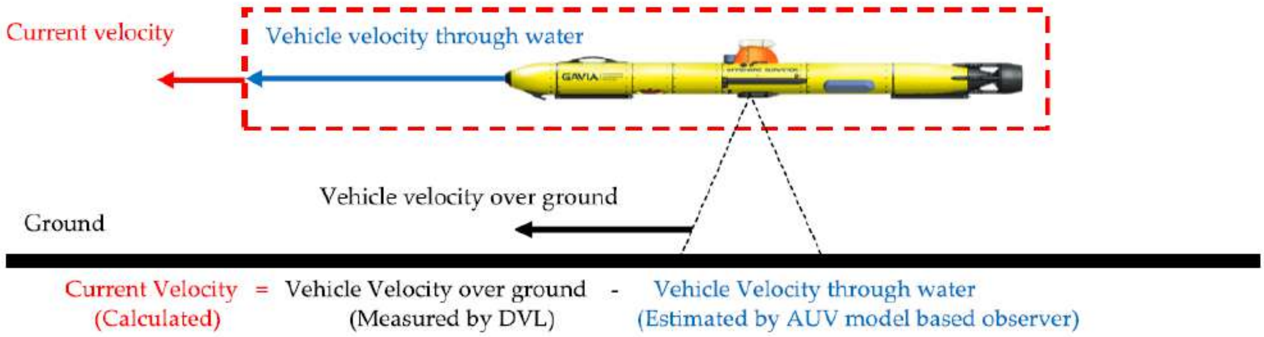

Figure 2.2: Illustration of current velocity, vehicle velocity through water and over ground.

In this study, the current components close to the AUV were obtained in 3-principal directions by calculating the differences between the vehicle velocities over the ground measured by the DVL-aided INS during the field test and the vehicle velocities through the water estimated by using the AUV model-based high-gain observer. Equation 2.1 gives this calculation in the vector form.

$$\vec{V}_{current} = \vec{V}_{OG} - \vec{V}_{TW} \tag{2.1}$$

where $\vec{V}_{current}$ is the current velocity vector ; $\vec{V}_{OG}$ is the vector of the vehicle's absolute velocity over the ground measured from field test using DVL-aided INS; and $\vec{V}_{TW}$ is the vector of vehicle's relative velocity through the water column obtained from AUV dynamic model. A notorious challenge with AUV state estimation is the lack of ground truth for speed measurements. A Doppler velocity log (DVL) is an acoustic sensor that measures velocity relative to the sea bottom, and so a DVL-aided INS may be used to acquire high-accuracy absolute velocity measurements [37]. During the field tests, the AUV underwent a straight-line, constant altitude mission while the water current velocities were measured through the AUV-onboard ADCP. The ADCPs were programmed to profile approximately 10 m of water column in 0.5 m range bins. The closest bin was 0.44 m away from the vehicle which referred as a blanking distance. Then water velocity components relative to the AUV in the body-fixed coordinate system in 3D were measured in each bin.

In order to analyse the motion of the AUV in 6 DOF, two coordinate frames, an inertial reference frame $\{x_i, y_i, z_i\}$ and a body-fixed frame $\{x_b, y_b, z_b\}$, were defined as indicated in

Figure 2.3. While the Earth-fixed frame was used as the inertial reference, the body-fixed reference frame was fixed to the AUV. The origin $\boldsymbol{O}$ of the body-fixed reference frame was chosen at the centre of buoyancy of the vehicle.

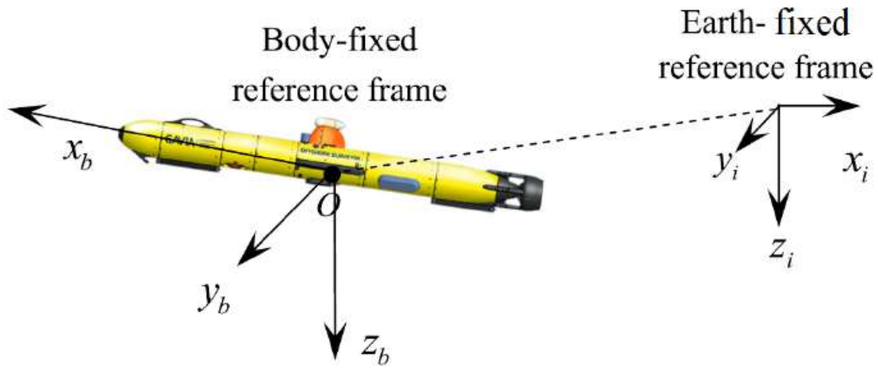

Figure 2.3: AUV's body-fixed and Earth-fixed reference frames.

Without current compensation, the AUV control system only provides commands to keep the AUV on a straight-line motion in the absence of current. However, the truth is that the vehicle is also moving under the current disturbances. In this case, the vehicle cannot keep the desired straight-line trajectory within the given control inputs. Thus, the motion difference can be used for current estimation. In order to compensate for the disturbances caused by any turbulent or unsteady flow and keep the prescribed straight-line path, the AUV's control system is required to control the propeller RPM and control surface angles. These control commands were recorded in the vehicle log and used as inputs for the AUV model-based observer to estimate the AUV velocities through the water. As a result of the estimation, the current velocities could be determined by calculating the differences between the vehicle velocities over the ground recorded through DVL-aided INS and the estimated vehicle velocities through the water. This process of current estimation is illustrated as a flow chart in Figure 2.4.

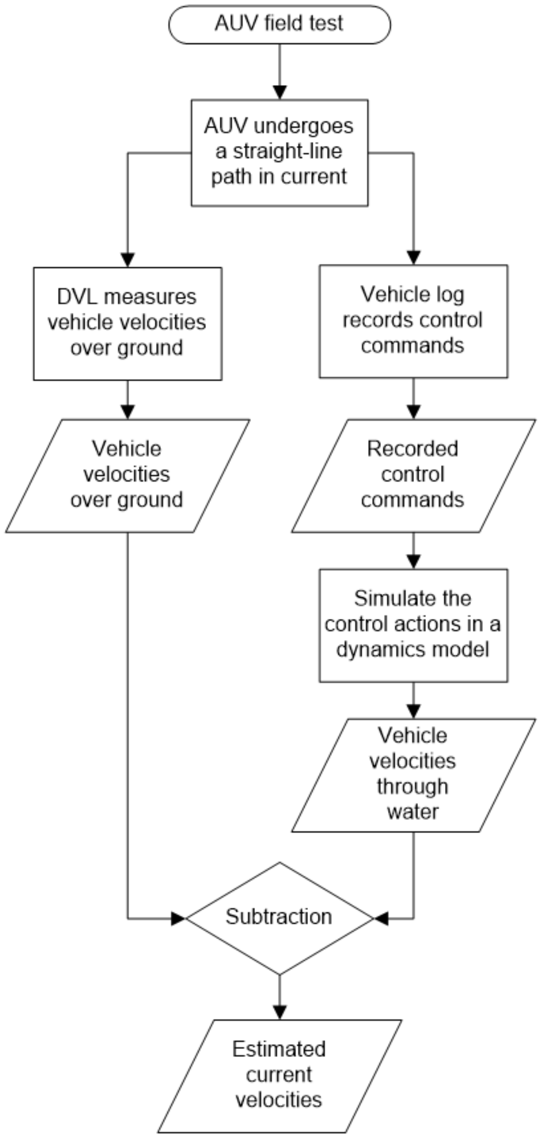

Figure 2.4: Flowchart to predict current velocities.

2.2.1 Vehicle Specifications

In order to validate the performance of the AUV model based observer for current estimation, field tests from a Gavia-class modular AUV were used. Its configuration is shown in Figure 2.5. The AUV consisted of a nose cone, battery module, interferometry sonar module (GeoSwath Plus Kongsberg Maritime AS), 1200 kHz Teledyne RD Instruments, ADCP/DVL module, Kearfott T24 INS module, control module and a propulsion module. The overall length of the vehicle was 2.7 m, the diameter was 0.2 m, and the dry weight in air was approximately 70 kg. The DVL-aided INS was used to derive the position of the AUV [27].

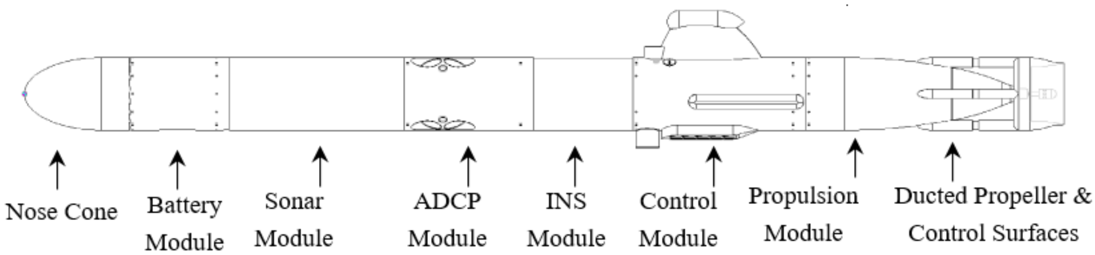

Figure 2.5: Configuration of the tested Gavia AUV .

In the ADCP module, there were two 1200 kHz Teledyne RD Instruments ADCPs/DVLs which were installed in upward-looking and downward-looking configurations respectively. Both the upward-looking and downward looking transducers could collect water column velocity data relative to the AUV (i.e., in ADCP mode), but the downward-looking transducers could also measure the vehicle velocity over the ground (i.e., in DVL mode).

The aim of this study was to validate the applicability of the AUV model based high-gain observer for current estimate by comparing the measured vehicle velocities over ground and the estimated vehicle velocities relative to the water column from an AUV model based high-gain observer.

Consequently, the estimated current velocities are compared and validated by the current velocity measurements from the on-board ADCP. The field test was conducted in the Tamar estuary where there was a dominant tidal current flow and a straight-line run was conducted against the flow direction. Test details are published by Randeni, et al. [27].

2.2.2 AUV Dynamic Model

The rigid body dynamics and hydrodynamics of the Gavia AUV were modelled according to the method formulated by Fossen [11] using MATLAB Simulink software. Referring to [11], the 6-DOF motion of an underwater vehicle can be expressed by Equation (2) and the mathematical equations in this chapter are based on the notation as given in Table 1.

$$\begin{aligned} &M\dot{\nu} + C(\nu)\nu + D(\nu)\nu + g(\eta) = t_{control} \\ &M = M_{RB} + M_A \\ &C(\nu) = C_{RB}(\nu) + C_A(\nu) \end{aligned} \tag{2.2}$$

where M is the system inertia matrix; $C(\nu)$ is the Coriolis-centripetal matrix; $D(\nu)$ is the damping matrix; $g(\eta)$ is the vector of the gravitational/buoyancy forces and moments; $t_{control}$ is the vector of body forces and moments; ν is the velocity vector (i.e., $[u\ v\ w\ p\ q\ r]$ where p,q and r are the angular velocities around the x,y and z axes); η is the vector of position/Euler angles (i.e., $[x\ y\ z\ \phi\ \theta\ \psi]$) where ϕ, θ and ψ are the roll, pitch and yaw angles respectively; M_{RB}

is the rigid-body inertia matrix, $C_{RB}(\nu)$ is the rigid-body Coriolis and centripetal matrix, and finally M_A and $C_A(\nu)$ are their added mass components.

Table 2.1: THE 6-DOF NOTATION FOR MARINE VESSELS

Degree-of Freedom	Forces and Moments	Linear and Angular Velocity	Position and Euler Angles
Motions in the x -direction (surge)	X	u	x
Motions in the y -direction (sway)	Y	v	y
Motions in the z-direction (heave)	Z	w	z
Motions in the x-direction (roll)	K	p	ϕ
Motions in the y-direction (pitch)	M	q	θ
Motions in the z-direction (yaw)	N	r	ψ

In response to the time series of control commands, the vehicle velocities through the water were reproduced by developing a motion model including inputs of propeller rotational rate (N) , pitch angle (θ), pitch rate (q), pitch acceleration ($\dot{q}$), yaw rate (r) and yaw acceleration ($\dot{r}$). Instead of deriving the rolling, pitching and yawing motions, these were directly given as model inputs which allowed the mathematical model to be simplified to 3-DOF (i.e. into linear motions along the x ,y and z directions) without modelling the angular motions. In this study, Equation 2.2 which represents the 6-DOF dynamic equation of motion was reduced to 3-DOF and simplified by assuming:

Assumption: Products of inertia (i.e., I_{xy}, I_{xz} and I_{yz}) are assumed to be zero since they are negligibly small compared to the moments of inertia (i.e., I_{xx}, I_{yy} and I_{zz}) of the vehicle [38].
Then Equation 2.2 can be expanded and rearranged as:

$$\begin{aligned}(m - X_{\dot{u}})\dot{u} + mz_g\dot{q} + my_g\dot{r} = (W - B)sin(\theta) + X_{u|u|}u|u| + (X_{wq} - m)wq \\ + (X_{qq} + mx_g)q^2 + (X_{vr} + m)vr \\ + (X_{rr} - mx_g)r^2 + X_nN^2\end{aligned} \tag{2.3}$$

$$\begin{aligned}(m - Y_{\dot{v}})\dot{v} + (mx_g + Y_{\dot{r}})\dot{r} = Y_{v|v|}v|v| + Y_{r|r|}r|r| + (Y_{ur} - m)ur \\ + Y_{uv}uv + mz_gqr\end{aligned} \tag{2.4}$$

$$\begin{aligned}(m - Y_{\dot{w}})\dot{w} - (mx_g + Z_{\dot{q}})\dot{q} = (W - B)cos(\theta) + Z_{w|w|}w|w| + Z_{q|q|}q|q| \\ + (Z_{uq} + m)uq + Z_{uw}uw\end{aligned} \tag{2.5}$$

where, N is the propeller revolutions per minute (RPM) and X_n is the thrust coefficient, which is 95×10^{-6} for the Gavia AUV according to the estimation by Porgilsson [39]. The acceleration terms in the equations of motion were separated on the left-hand side while the right-hand sides included the hydrostatic, hydrodynamic damping and control forces.

$$u - \dot{X_n} \times N^2 = \alpha_1\dot{q} + \alpha_2\dot{r} + \alpha_3 u|u| + \alpha_4 wq + \alpha_5 q^2 + \alpha_6 vr + \alpha_7 r^2 + \alpha_8 sin(\theta) \tag{2.6}$$

$$\dot{v} = \beta_1\dot{r} + \beta_2 v|v| + \beta_3 r|r| + \beta_4 r^2 + \beta_5 ur + \beta_6 ur + \beta_7 qr \tag{2.7}$$

$$\dot{w} = \gamma_1\dot{q} + \gamma_2 w|w| + \gamma_3 q|q| + \gamma_4 wq + \gamma_5 uw + \gamma_6^2 + \gamma_7 rq + \gamma_8 cos)\theta \tag{2.8}$$

The coefficients (e.g., $m, X_{\dot{u}}$ and z_g) in Equations 2.3 - 2.5 were superimposed in unknown parameters (α_{1-8}, β_{1-7}, and γ_{1-8}) in Equation 2.6 - 2.8, which eliminated the need to measure them. While the vehicle's linear accelerations (i.e.,$\dot{u}$,$\dot{v}$ and $\dot{w}$) were rearranged on the left hand sides of Equation 2.6 - 2.8, unknown parameters on the right hand sides were to be identified by using the Recursive Least Squares (RLS) algorithm approach.

In Equations 2.9, the system output vector $y_{(t)}$ was comprised of a regressor vector $\Gamma_{(t)}$ and a parameter vector $Phi_{(t)}$, and accordingly Equation 2.6 - 2.8 were represented in TABLE 2.

$$y_{(t)} = \Gamma_{(t)}\Phi_{(t)} \tag{2.9}$$

Table 2.2: $y_{(t)}$,$\Gamma_{(t)}$ AND $\Phi_{(t)}$ VECTORS FOR REPRESENTATION OF EQUATION 2.6 - 2.8.

Axis	Outcome, $y_{(t)}$	Regressor, $\Gamma_{(t)}$	Parameter, $\Phi_{(t)}$
x	$\dot{u} - X_n N^2$	$[\dot{q} \quad \dot{r} \quad u\|u\| \quad wq \quad q^2 \quad vr \quad r^2 \quad \sin(\theta)]$	$[\alpha_1\ \alpha_2\ \alpha_3\ \alpha_4\ \alpha_5\ \alpha_6\ \alpha_7\ \alpha_8]$
y	$\dot{v}$	$[\dot{r} \quad v\|v\| \quad r\|r\| \quad r^2 \quad ur \quad uv \quad qr]$	$[\beta_1\ \beta_2\ \beta_3\ \beta_4\ \beta_5\ \beta_6\ \beta_7]$
z	$\dot{w}$	$[\dot{q} \quad w\|w\| \quad q\|q\| \quad uq \quad uw \quad \cos(\theta)]$	$[\gamma_1\ \gamma_2\ \gamma_3\ \gamma_4\ \gamma_5\ \gamma_6\ \gamma_7\ \gamma_8]$

In highly dynamic environments, the parameters of the mathematical model fluctuate with time due to environmental forces [19]. Therefore, in this study, a real-time model identification algorithm was utilised to identify the dynamics parameters with continuous updates, which allowed the AUV model to produce the vehicle's motion response in the present environment. Unknown parameter vectors were identified in real-time by utilising the Recursive Least Squares (RLS) estimation block set up in the MATLAB Simulink Identification toolbox. The identified parameters were varied while the simulation was running as shown in Figure 2.6, and parameters at the end of simulation, for example, are tabulated in Table 3.

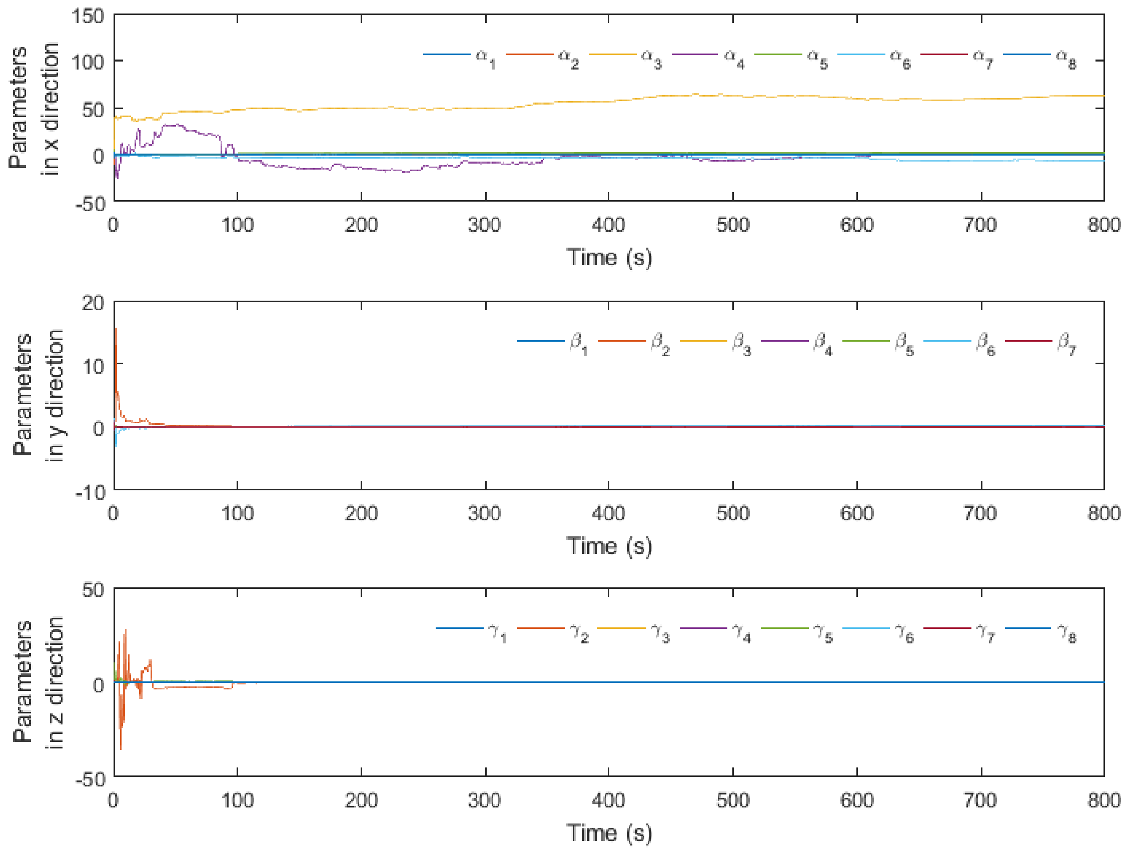

Figure 2.6: Dynamics model parameters identified by the real-time RLS method during the simulation.

Table 2.3: IDENTIFIED PARAMETER VALUES AT THE END OF SIMULATION

	1	2	3	4	5	6	7	8
α_{1-8}	-0.3335	0.0699	62.5408	-1.8373	1.8108	-3.3354	0.0856	33.3374
β_{1-7}	-0.0120	-0.0250	-0.0022	0.0012	0.0500	0.1757	0.0012	-
γ_{1-8}	0.0129	-0.1582	-0.0042	-0.0196	0.4036	0.0004	0.0003	-0.0096

In order to obtain the AUV's linear velocities, the linear acceleration terms from Equations 2.6 - 2.8 were solved in the AUV dynamic model by using the recorded input values as shown in the flow chart in Figure 2.7. Six inputs were recorded, such as: propeller rotation rate(N), pitch angle (θ), pitch rate (q), pitch acceleration ($\dot{q}$), yaw rate (r) and yaw acceleration ($\dot{r}$). Integrating the linear accelerations with respect to time produced the linear velocities in the body-fixed reference frame.

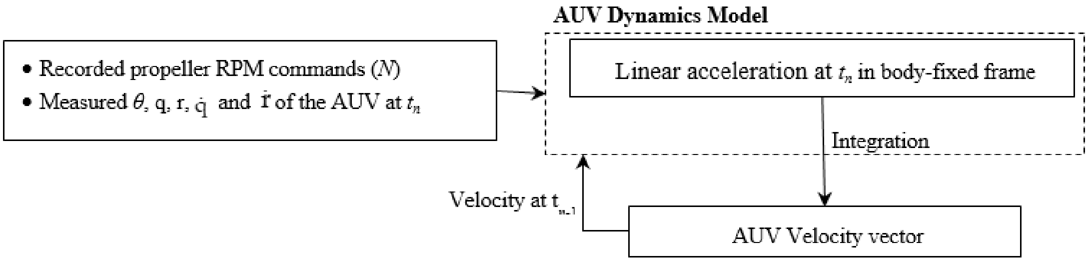

Figure 2.7: Model-based velocity calculation flowchart. The acceleration at t_n was obtained with recorded RPM(N), measured variables (θ,q, r, $\dot{q}$ and $\dot{r}$) as well as velocity vector at t_{n-1}. Then AUV velocity vector is solved by integrating the acceleration vector with respect to time.

2.2.3 High-Gain Observer Design

In this section, a high-gain observer based on the AUV dynamic model was designed. In order to set up the nonlinear high-gain observer, a state space model for the AUV is described below:

$$\begin{aligned} \dot{x} &= Ax + f(x,t) \\ y &= Cx \end{aligned} \tag{2.10}$$

where $x \in \mathbb{R}^n$ is the state vector; $y(t) \in \mathbb{R}^n$ is the measurement output vector; and, $A \in \mathbb{R}^{n\times n}$ $C \in \mathbb{R}^{m\times n}$, and the function f is defined as follows:

$$x(t) = [\phi \quad \theta \quad \psi \quad u_r \quad v_r \quad w_r]$$

$$C = \begin{bmatrix} 0 & 0 & 0 & 1 & 0 & 0 \\ 0 & 0 & 0 & 0 & 1 & 0 \\ 0 & 0 & 0 & 0 & 0 & 1 \end{bmatrix}$$

$$f(x,t) := \begin{bmatrix} f_1(x_1,t) \\ f_2(x_1,x_2,t) \\ \vdots \\ f_{n-1}(x_1,x_2,\cdot,x_{n-1},t) \\ f_n(x_1,x_2,\cdot,x_n,t) \end{bmatrix}$$

To estimate $\hat{x}(t)$, the observer was considered as follows:

$$\dot{\hat{x}} = A\hat{x} + \hat{f}(\hat{x},u) + G(\gamma)(y - C\hat{x}) \tag{2.11}$$

where $\hat{x}(t)$ is the estimate of $x(t)$ at time t; the observer gain, $G(\gamma, K) := [\gamma k_1 \; \gamma k_2 \; \cdots \; \gamma k_n]^T$ with $K := [k_1 \; k_2 \; \cdots \; k_n]^T$ and $k_i \in \mathbb{R}, i = 1, \; 2, \; \cdots \; n$ [35]. The estimation error ($\hat{e} := x - \hat{x}$) dynamics were derived from Equation 2.10 and 2.11 as follows:

$$\dot{\hat{e}}(t) = (A - GC)\hat{e}(t) + f(x(t),t) - \hat{f}(x(t) - \hat{e}(t),t) \tag{2.12}$$

Instead of studying the stability of the estimation error, variables were transformed $\hat{e} := T(\gamma)e, e \in \mathbb{R}^n$ with $T(\gamma) = diag(\gamma, \; \gamma^2, \; \cdots \; \gamma^n)$ resulting Equation 2.13 as follows:

$$\dot{\hat{e}}(t) = T(\gamma)^{-1}(A - GC)T(\gamma)e(t) + T(\gamma)^{-1}\{f(x(t),t) - f(x(t) - T(\gamma)e(t),t)\} \tag{2.13}$$

Because of the particular observer structure, the previous equation was rewritten as follows:

$$\dot{\hat{e}}(t) = \gamma(A - GC)e(t) + T(\gamma)^{-1}f(x(t), t) - f(x(t) - T(\gamma)e(t), t) \tag{2.14}$$

The stability of the error dynamics was investigated via a Lyapunov function. Furthermore, based on the fact that (A,C) is observable, there exist $\lambda > 0,\ K \in \mathbb{R}^n$ and a symmetric positive matrix $P \in \mathbb{R}^{n\times n}$ such that

$$(A - KC)^T P + P(A - KC) + \lambda I < 0 \tag{2.15}$$

with $K := [k_1\ k_2\ \cdots\ k_n]^T$. The above equation could be treated by solving the equivalent LMI:

$$A^T P + PA - C^T Y^T - YC + \lambda I < 0 \tag{2.16}$$

where the unknowns are $\lambda > 0,\ Y = PK \in \mathbb{R}^n$ and $P > 0$.
In order to compute the solution to a given system of LMIs, a number of MATLAB functions were used as tabulated in Table 4. Before starting the description of a new LMI system, a function `setlmis` was used to initialise its internal representation. The function `limvar` defined new matrix variables and in the LMI system currently described. The variable matrix was defined as a symmetric matrix while was defined as a rectangular matrix. One of the gain parameters, was defined as a constant. By using a function `limterm`, the term contents of an LMI one term at a time. The LMI term referred to the elementary additive terms involved in the block-matrix expression of the LMI. For example, in order to express the Equation 2.16, three terms were required as shown in Table 4.4. For more details for the `limterm` function description, see [40]. After completing the description of a given LMI system with lmivar and `limterm`, its internal representation `lmisys` was obtained with the command `getlims`. The function `feasp` computed a solution `xfeas` of the system of LMIs described by `lmisys`. The vector `xfeas` was a particular value of the decision variables for which all LMIs were satisfied. Finally, a function `dec2mat` computed the corresponding value `valx` of the matrix variable with identifier X given the value `decvars` of the vector of decision variables. As a result, matrix variables – P, Y and λ in the LMI system were obtained, then P and Y were used to calculate the one of gain parameter K.

Table 2.4: MATLAB FUNCTIONS USED TO FIND THE GAIN MATRIX AND ITS DESCRIPTION [40]

-	MATLAB function	Function description
1	`setlmis([])`	Initialize description of LMI system
2	`lmivar(type,struct)`	Specify matrix variables in LMI problem.
	Type = 1: Symmetric matrices with a block-diagram structure.	
	Type = 2: Full m-by-n rectangular matrix.	
	`P=lmivar(1,[6 1])`	Specify matrix P (6×6)
	`Y=lmivar(2,[6 1])`	Specify matrix Y (6×3)
	`λ=lmivar(1,[1 1])`	Specify matrix λ (1×1)
3	`lmiterm(termID,A,B,flag)`	Specify term content of LMIs for Equ. (3.16) .
	`lmiterm([1 1 1 P],1,A,'s')`	$A^T P + PA$
	`lmiterm([-1 1 1 Y],1,C,'s')`	$C^T Y^T - YC$
	`lmiterm([1 1 1 lambda],1,1)`	λI
	`lmiterm([-2 1 1 P],1,1)`	$P > 0$
	`lmiterm([-3 1 1 lambda],1,1)`	$\lambda > 0$
4	`lmisys=getlmis`	Internal description of LMI system.
5	`[tmin,xfeas]=feasp(lmisys)`	Compute solution (xfeas) to given system of LMIs.
6	`valX=dec2mat(lmisys,decvars,X)`	Given values of decision variables, derive corresponding values of matrix variables.
	`P=dec2mat(lmisys,xfeas,P)`	Solution for Matrix P
	`Y=dec2mat(lmisys,xfeas,Y)`	Solution for Matrix Y
	`λ=dec2mat(lmisys,xfeas,λ)`	Solution for Matrix λ
7	`K=inv(P)*Y`	Calculation of the gain matrix.

The high-gain observer design was accomplished by solving the LMI problem so the gain $K = P^{-1}Y$ and λ were obtained as follows:

$$\lambda = 2.2707, K = \begin{bmatrix} 1.3383 & 0 & 0:8730 \\ 0 & 0.7599 & 0 \\ 0.2967 & 0 & 0.8041 \\ 0 & 0.1586 & 0 \\ 0.5121 & 0 & 0.7589 \\ 0 & -0.1884 & 0 \\ -8.0381 & 0 & 34503 \\ 0 & 2.1625 & 0 \\ 3.2320 & 0 & 3.6946 \end{bmatrix}$$

2.3 Results and Discussion

The proposed high-gain observer design was validated by comparing the estimated current velocities with recorded current velocities from an on-board ADCP. In the field test, the AUV underwent a straight and constant depth mission as illustrated in Figure 2.8 and Figure 2.9

respectively. In order to estimate the current velocities, firstly the vehicle's velocities through the water were estimated by the model-based observer. Then the current velocities could be calculated by subtracting the estimated velocities through the water from the vehicle's velocities over the ground measured by the DVL.

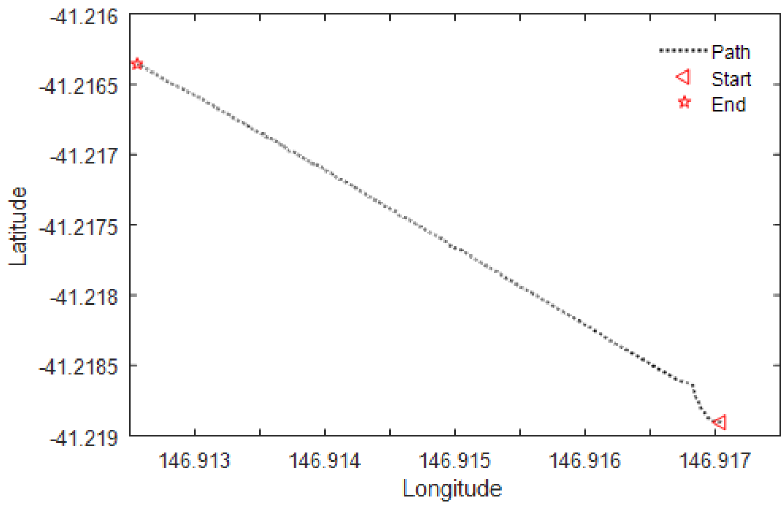

Figure 2.8: Trajectory that the vehicle underwent during the field test.

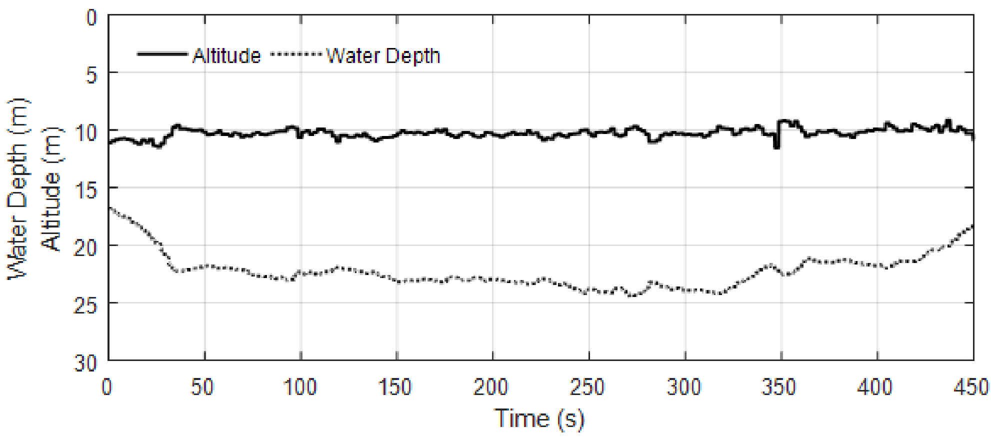

Figure 2.9: Water Depth and AUV's altitude during the field test.

Figure 2.10 shows the vehicle's velocities over the ground recorded by the DVL-aided INS navigation system during the field test and vehicle's velocities through the water estimated by the model-based observer in the x_b, y_b and z_b direction respectively. In the x_b axis, the vehicle velocities over the ground and through the water showed the greatest difference compared to those in the y_b and z_b axes. This difference leads to an estimate of around -1 m/s current velocity in the longitudinal direction. It can be inferred that the straight line that the vehicle followed during the field test was against the tidal flow direction.

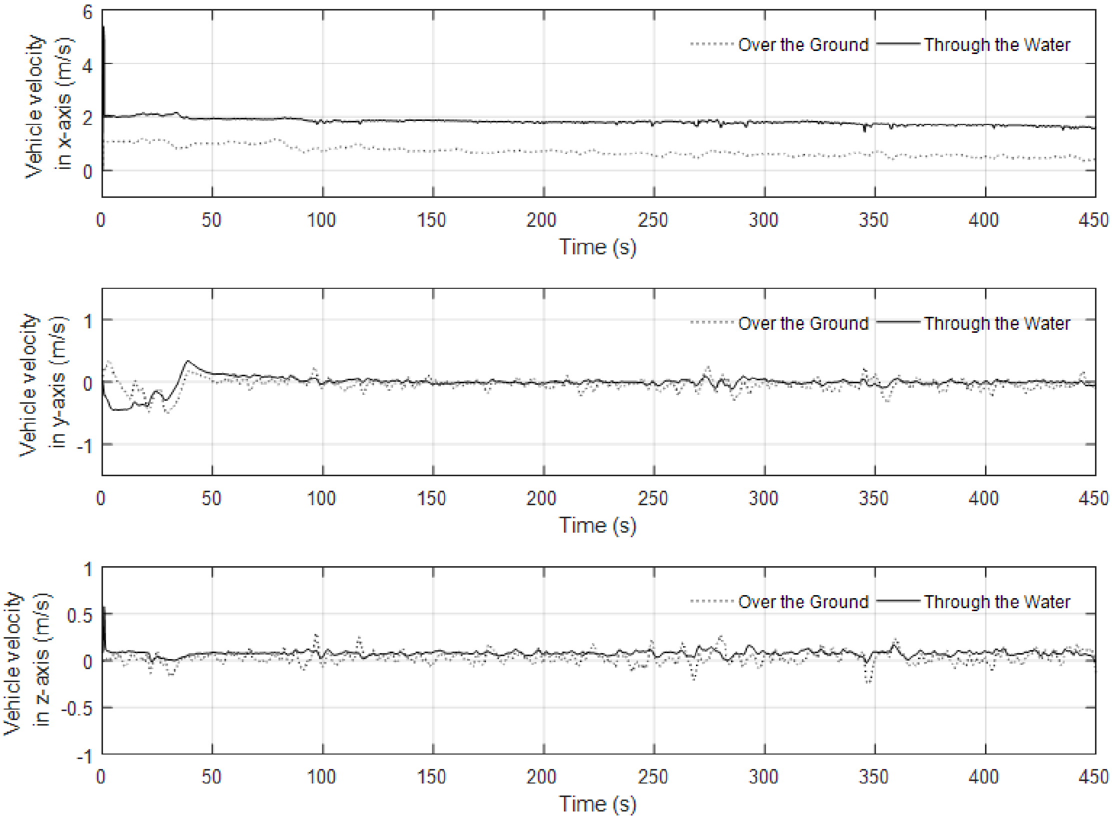

Figure 2.10: The vehicle velocities over ground measured by DVL-aided INS (dotted curves) and velocities through water estimated by AUV model-based high-gain observer (solid curve) along x, y and z axis.

Figure 2.11 shows the current velocities estimated by the AUV model-based observer and measured current velocities from the ADCP in the x_i, y_i and z_i axes directions, respectively. Although the current velocities were measured 0.44 m away from the vehicle due to the ADCP's blanking distance, the estimated current velocities from the observer were closely matched with the measured current velocities.

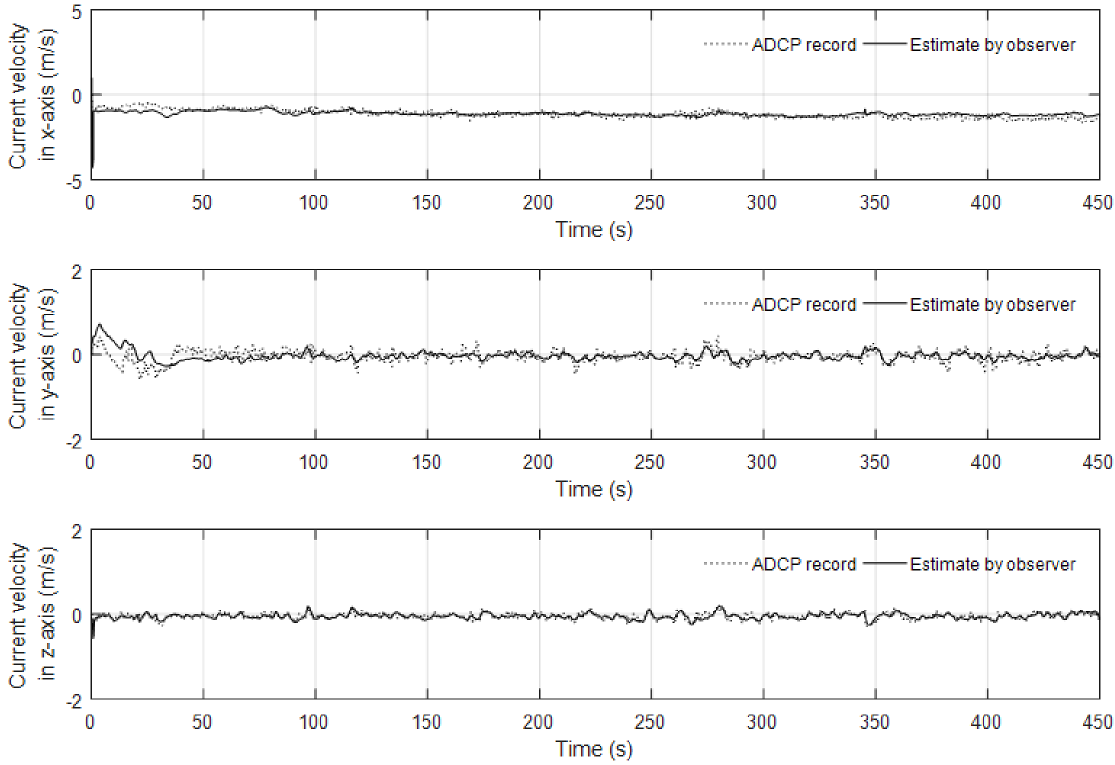

Figure 2.11: The comparison between the current velocities measured by ADCP (dotted curve) and its counterpart which was estimated by the high-gain observer (solid curve) in x, y and z axis.

A peaking phenomenon was found in the estimated current velocity especially in the xi axis as shown in Figure 2.12. Using the high-gain observer results in a peaking phenomenon which shows up as a large estimation gap during the short period right after the initial time. However, the transient period shown in the estimated current velocity was very short relative to the time scale, and the estimated velocities approached the measured current velocities very promptly and closely.

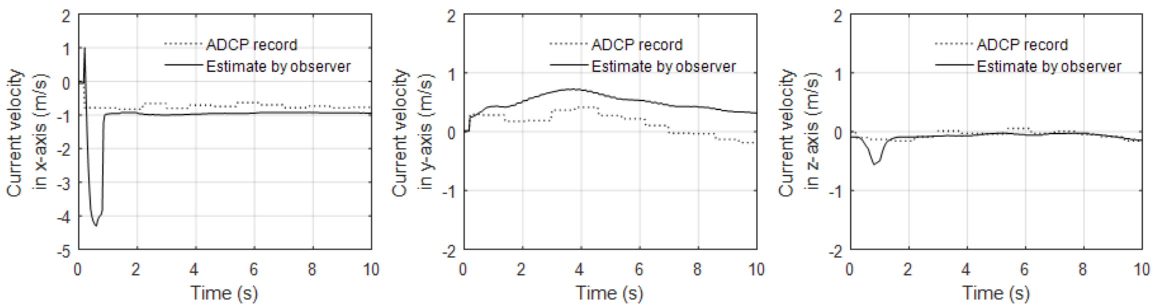

Figure 2.12: Peaking phenomena in current estimation at the beginning of the estimation process (10 second) compared to the current velocities recorded by the ADCP.

In order to investigate the differences between the current velocity estimates from the AUV model-based observer and the current velocities measured by the ADCP, the standard deviations between these two were quantified in Table 2.5. Here, the standard deviation of the current estimate results were 0.0942 m/s, 0.0656 m/s and 0.0323 m/s. The current measurement from the ADCP were taken 0.44 m away from the vehicle while the current estimates from the observer were calculated at the vehicle.

Table 2.5: STANDARD DEVIATION OF CURRENT ESTIMATES

Direction	x - axis	y - axis	z - axis
Standard Deviation	0.0942 m/s	0.0656 m/s	0.0323 m/s
Absolute error	0.108 m/s	0.067 m/s	0.030 m/s

In the research of Randeni, et al. [27], a method is proposed to calculate the water velocity components of a turbulent water column using the AUV motion response (referred to as the 'WVAM method'), for which the current velocities are solved by determining the difference between the motion responses of the vehicle in calm and turbulent water environments. The field test data used in this study was acquired from part of the Randeni, et al. study [27], which allowed a comparison to be made between the respective methods for current velocities estimation. Figure 2.13 shows the comparison between the current measurements from the ADCP, the current velocity estimated from the AUV model-based observer and the current velocity calculated by WVAM method in three dimensions.

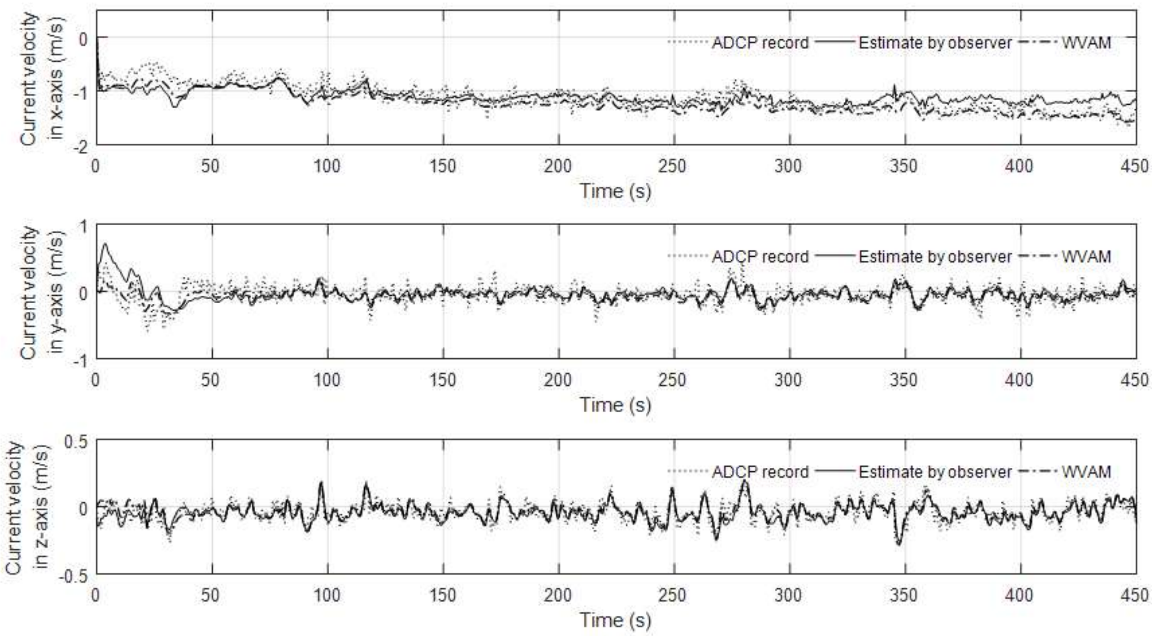

Figure 2.13: Comparison between the current velocities in the z direction between ADCP measurement, estimate from the observer and calculation from WVAM method respectively.

The difference between velocities obtained from the WVAM method and ADCP were calculated by quantifying the standard deviation and these are 0.09 m/s, 0.07 m/s and 0.06 m/s [27]. Compared with the standard deviation of the current estimate results using the high-gain observer, those for the xi and yi axes were similar, but the standard deviation of the current estimation from the high-gain observer in the zi axis was less: 0.0323 m/s.

Furthermore, an estimate of error was calculated by using equation 2.17 to assess the improvement of the proposed AUV model-based observer to estimate the current velocity compared with the WVAM method.

$$estimation\ error\ (\%) = (V_{ADCP} - V_{Est})/V_{ADCP} \times 100 \tag{2.17}$$

where V_{ADCP} is the measured current velocity by ADCP and V_{Est} is the estimated current velocity by the observer and the WVAM method.

Table 2.6: ESTIMATION ERROR MEAN FOR MODEL-BASED OBSERVER AND WVAM METHOD

Estimation Error Mean (%)	x - axis	y - axis	z - axis
Model-based observer	1.222 %	0.810 %	0.370 %
WVAM method	1.283 %	0.778 %	0.395 %
Estimation improvement of model-based observer	+4.992%	-3.951 %	+6.757 %

In Table 2.6, estimation error means of the current estimation results for the model-based observer and WVAM method are tabulated. The estimation error means of the model-based observer was smaller than their counterpart from the WVAM method in both x_i and z_i axes which results in an estimation improvement of 4.992 % and 6.757 % respectively. In the y_i axis, the estimation error mean of the model-based observer was slightly larger than its counterpart from the WVAM method. This could have resulted from a lower number of unknown parameters (β_{1-7}) in the yi axis dynamic equation than the number of parameters in the other two axes (α_{1-8} and γ_{1-8}), while the number of the unknown parameters of each axis had been decided by rearranging and superimposing of the underactuated AUV dynamic motion equation. This could have resulted in the current estimation in y_i axis converged into the measured current velocity more slowly than the other two axes, as is shown in the time period between 0 to 50 second in Figure 2.13, which caused the slightly larger estimation error mean in the yi axis than the counterpart of WVAM method.

In contrast to the WVAM method, estimated current velocities using the AUV model-based observer did not require an additional field test in a calm water environment in order to reproduce the AUV responses in the simulation model.

2.4 Conclusion

In order to verify the capability of the AUV dynamic model-based observer for predicting the water current velocities in this study, the water current velocity components in the x_i, y_i and z_i axes of inertial frame were estimated. The water current velocities were estimated by calculating the difference between the vehicle velocities over ground recorded using the DVL and the vehicle velocities through the water estimated from an AUV model-based observer. A Gavia AUV was utilised to conduct a straight-line, constant depth mission to record the current velocities and vehicle velocities by utilising on-board ADCP and DVL respectively. The AUV dynamics model that represents the Gavia AUV behaviour was developed using MATLAB Simulink. Instead of deriving the roll, pitch and yaw motions, these were directly given as simulation inputs which allowed the AUV dynamics model to be simplified to 3-DOF. For the AUV dynamic model, hydrodynamics parameters were identified by applying real-time system identification utilising the RLS identification method. The RLS identification technique was used as it has the advantages of simple calculation and good convergence properties. The real-time model identification algorithm allowed the AUV model to be continuously updated in response to the operational environment. The high-gain observer was used as a nonlinear estimation algorithm to obtain the vehicle velocities through the water. Stability of the estimation error dynamics was investigated via the Lyapunov function. The observer gain was computed by solving the LMIs (Linear Matrix Inequalities) which represented the error dynamics equation.

During the AUV simulation, the vehicle velocities through the water were obtained by applying the equivalent control commands which were executed during the field test. Once the vehicle velocities through the water were available, the current velocities were calculated by subtracting the vehicle velocities through the water from the vehicle velocities over the ground recorded by the DVL-aided INS. The estimated current velocities in the x_i, y_i and z_i direction were found to be well matched with the measured current from the AUV-onboard ADCP. In order to quantify the differences between the estimated and measured current velocities, standard deviations were calculated as 0.0942 m/s, 0.0656 m/s and 0.0323 m/s for the x_i, y_i and z_i axes components respectively. Furthermore, the current estimation results from the AUV model-based observer were also compared with the estimation results from the WVAM method [27] which utilises motion differences. The estimation error percentages illustrated that the current estimation found by using the model-based observer was improved by as much as 6.8 % in the z_i axis, less in the other directions.

For precise navigation and control of an AUV, it is critical to obtain the current velocities around the boundary layer of the AUV where the ADCP is unable to measure due to its blanking distance. Hence the AUV model-based observer is advantageous to estimate the current velocities either close to or at the vehicle by utilising an AUV dynamics model. Precise hydrodynamics properties can be identified from the real-time measurement.

Chapter 3

AUV Model-Based High-Gain Observer

This chapter is based on the journal article ‘Autonomous Underwater Vehicle Model-Based High-Gain Observer for Ocean Current Estimation’ that is published in the journal ‘*2018 IEEE/OES Autonomous Underwater Vehicle Workshop (AUV)*’. The citation for the article is:

E. Kim, S. Fan, and N. Bose, Autonomous Underwater Vehicle Model-Based High-Gain Observer for Ocean Current Estimation, *2018 IEEE/OES Autonomous Underwater Vehicle (AUV) Workshop*, 2018, [2].

In the previous chapter, the Gavia AUV model parameters were identified by system identification using a recursive least squares method and the high-gain observer based on the AUV dynamic model was introduced. In this chapter, the Dolphin II AUV simulator was developed using known hydrodynamic parameters in order to verify the performance of the proposed high-gain observer for estimating the current. In the simulation, the ocean current was assumed to be non-uniform and unsteady which varies over space and time. The magnitude of the current velocities were decided from the difference between the vehicle's absolute velocities and the relative velocities estimated by the model-based HGO. The observer gain for the HGO was determined by solving the Linear Matrix Inequality (LMI) describing the estimate error dynamics.

3.1 Introduction

AUVs have drawn attention over the past decades through their use for various applications such as seabed mapping, search or rescue and environmental surveys. These missions require georeferencing which is crucial for vehicles to record navigational data and to return to previous mission sites [18]. One of the essential components for localisation and navigation is an Initial Navigation System (INS). The INS utilises an Inertial Measurement Unit (IMU) to estimate the AUV's states including the position, orientation and velocity relative to the inertial frame. Since a navigation system only based on an INS can result in a relatively large position drift error, the INS can be aided by the bottom tracking DVL to reduce the error [20]. However, the DVL-aided INS is occasionally unavailable when the vehicle is in regions where a Doppler Velocity Log (DVL) is out of range from the bottom. In other words, the distance between the vehicle and seabed is larger than the transmission range of the DVL: for instance for Teledyne RD Marine DVLs, 300 kHz DVLs have a maximum range of around 200 m, while the maximum range of 1200 kHz DVLs is around 30 m [19]. When the DVL is out of the range of the seabed, the vehicle's velocity can be estimated by utilising a model-based inertial navigation algorithm: i.e. a model-aided INS [21]. The state-of-the art model-aided inertial navigation system (MA-INS) for underwater vehicle is presented in [22] to provide velocity aiding for the INS and validated by real-time sea current estimation and experimental output. Despite the fact that the localisation by the MA-INS is not as precise as the DVL-aided INS, the MA-INS is more accurate than an unaided INS and the DVL-aided INS in the water tracking mode.

As underwater vehicles are applied into more dynamic and limited environment, more accurate dynamic model is required for controlling the vehicle and estimating of the states. The vehicle dynamic model in currents is presented in [41], and it is assumed that the flow dynamics is composed of two components– a steady, nonuniform component and an unsteady and uniform component. Based on this assumption, a dynamic model for the motion of a rigid vehicle in an unsteady nonuniform flow is presented in [42]. Furthermore, information of the ocean current or water column can enhance navigation accuracy and control performance, a nonlinear observer based on a dynamic motion model in a current for an AUV was introduced to estimate the current velocities [14]. The current velocities are the difference between the vehicle's absolute velocities and relative velocities obtained by the nonlinear observer. However, the observer gain matrix is preliminarily optimised by using the pole placement which appoints the Eigen values at certain poles.

There are numerous introduced estimator approaches, but the HGO is one of the most prominent estimation techniques used in nonlinear control [43]. The HGO employs the selection of adequately large gain to reduce the impact of uncertainty and nonlinearity in the error estimation dynamics. However, as the gain becomes increased a peaking phenomenon occurs in the transients, which can destabilize the control loop [32]. A time-varying increasing-gain observer is presented by Alessandri and Rossi [35] for a nonlinear system. Beginning with small initial gain, it gradually escalates up to its maximum and is fixed at certain value. The design parameters are selected by solving a set of linear matrix inequalities (LMIs) and a nonlinear programming problem in a few variables. LMI theory has lately drew attention because different ranges of control problems can be narrowed down to a few standard convex optimization problems such as LMIs. The format of an LMI can be very general, which allows that diverse constraints from control theory such as Lyapunov and Riccati inequalities can all be written as LMI. Hence, LMIs can be used to solve various optimisation and control problems and the LMI was utilised in this chapter to determine the gain for the observer design [36].

In this chapter a nonlinear observer based on an AUV dynamic model in currents is presents to obtain the current velocity estimates. This chapter is organised as follows: Section 3.2 describes the methodology including the AUV kinetic, dynamic models and observer design. Section 3.3 and Section 3.4 are devoted to present results and conclusion.

3.2 Methodology

The current velocity can be taken from the difference between the vehicle's absolute and relative velocity as illustrated in Equation 3.1 which gives this calculation in vector form as follows:

$$\vec{V}_{current} = \vec{V}_{Abs} - \vec{V}_{Rel} \tag{3.1}$$

where $\vec{V}_{current}$ is the vector of the current velocity ; $\vec{V}_{Abs}$ is the vector of the vehicle's absolute velocity; and $\vec{V}_{Rel}$ is the vector of vehicle's relative velocity estimated by the AUV dynamic model-based HGO. In this study, the current velocities near the vehicle were estimated in 3-principal axes by using the AUV dynamic model-based HGO.

3.2.1 Kinematics

In order to study the motion of the AUV in currents, two coordinate frames, an inertial reference frame and a body-fixed frame, are defined as shown in Figure 3.1 – this is based on the notation from [14]. The inertial frame $[x_i, y_i, z_i]$ is fixed in inertial space such that z_i is aligned with the force due to gravity. The vector x_b in the body-fixed reference frame is aligned with the longitudinal axis of the vehicle while vector y_b is directed to port and z_b is directed to the bottom.

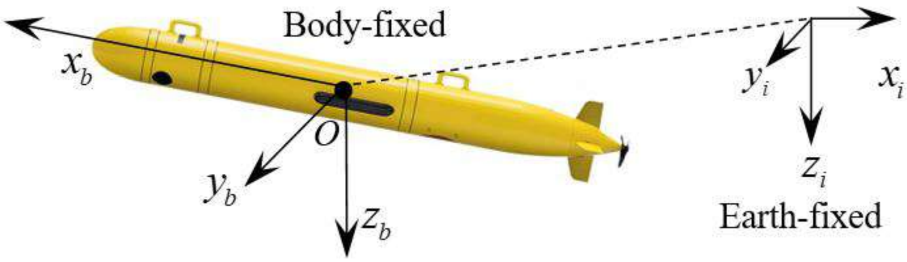

Figure 3.1: AUV's body-fixed and Earth-fixed reference frames.

$\mathbf{X} = [x, y, z]^T$ is the position vector between the origin of the inertial fixed frame and the origin of body-fixed reference frame. The vector $\mathbf{X}$ is in North-East-Down coordinates and is described in the inertial frame. The vehicle's translational and rotational velocities are denoted as $\nu = [u, v, w]^T$ and $\omega = [p, q, r]^T$ with respect to the inertial frame, but they are represented in the body frame of reference. The kinematic equations are

$$\begin{aligned} \dot{x} &= R\nu \\ \dot{R} &= R\hat{\omega} \end{aligned} \tag{3.2}$$

where $\hat{\cdot}$ denotes the 3×3 skew-symmetric matrix satisfying $\hat{a}b = a \times b$ for vectors a and b. Based on the theory in [41], a current flow $V_f(X, t)$ consists of an unsteady, uniform flow component $V_u(t)$ and a steady, circulating flow component $V_s(X)$. In the body-fixed reference frame, two flow components are more favorably represented as Equation 3.3. Then the flow field can be represented by summing these two components as Equation 3.4.

$$\begin{aligned} \nu_u(R, t) &= R^T \nu_{u(t)} \\ \nu_s(R, X) &= R^T \nu_s(X) \end{aligned} \tag{3.3}$$

$$\nu_f(R,X,t) = \nu_u(R,t) + \nu_s(R,X) \tag{3.4}$$

3.2.2 Dynamics

The dynamic model of the AUV in currents can be derived in terms of the vehicle's relative velocity as follows:

$$\begin{aligned}
(M_f + M)\dot{\nu}_r = &- \begin{bmatrix} \hat{\omega} & 0 \\ \hat{\nu_r} & \hat{\omega} \end{bmatrix} (M_f + M)\nu_r + \begin{bmatrix} f \\ m \end{bmatrix} \\
&- \begin{bmatrix} \hat{\omega} & 0 \\ \hat{\nu_r} + \hat{\nu_u} + \hat{\nu_s} & \hat{\omega} \end{bmatrix} (M - \bar{M}) \begin{bmatrix} \nu_u + \nu_s \\ 0 \end{bmatrix} \\
&- \begin{bmatrix} 0 & 0 \\ \hat{\nu_u} + \hat{\nu_s} & 0 \end{bmatrix} (M - \bar{M})\nu_r - \begin{bmatrix} \Phi & 0 \\ 0 & 0 \end{bmatrix} (M_f + \bar{M})\nu_r \\
&- (M - \bar{M}) \begin{bmatrix} (\nu_u + \nu_s)\omega + \frac{\partial}{\partial t}\nu_u + \Phi^T(\nu_u + \nu_s + \nu_r) \\ 0 \end{bmatrix}
\end{aligned} \tag{3.5}$$

where M is generalized inertia matrix and M_f is generalized added inertia matrix for rigid vehicle. $\bar{M}$ denotes a mass matrix that accounts for the kinetic energy of the fluid that is replaced by the vehicle. Note that except the first line in Equation 3.5, rest terms illustrate the impact of current on dynamics of AUV. The explanation of the external forces,f, and moments,m, exerting on the vehicle is not elaborated here for reasons of brevity [44].

3.2.3 Observer Design based on AUV Dynamic in Currents

This section is devoted to establishing the HGO based on a dynamic model in a current for the AUV in order to estimate the current velocity. By using the kinematic Equation 3.2 and dynamic equation 3.5, the system dynamics can be expressed as

$$\begin{aligned}
\dot{x} &= Ax + f(x,u) \\
y &= Cx
\end{aligned} \tag{3.6}$$

where $x \in \mathbb{R}^n$ is the state vector; $y(t) \in \mathbb{R}^n$ is the measurement output vector; $u = [n, \delta_r, \delta_e]^T$ is the vector of control input; $A \in \mathbb{R}^{n\times n}$ $C \in \mathbb{R}^{m\times n}$, and the function f is defined as follows:

$$\begin{aligned}
x(t) &= [\phi \quad \theta \quad \psi \quad u_r \quad v_r \quad w_r] \\
C &= \begin{bmatrix} 0 & 0 & 0 & 1 & 0 & 0 \\ 0 & 0 & 0 & 0 & 1 & 0 \\ 0 & 0 & 0 & 0 & 0 & 1 \end{bmatrix} \\
f(x,t) :&= \begin{bmatrix} f_1(x_1,t) \\ f_2(x_1,x_2,t) \\ \vdots \\ f_{n-1}(x_1,x_2,\cdot,x_{n-1},t) \\ f_n(x_1,x_2,\cdot,x_n,t) \end{bmatrix}
\end{aligned}$$

It is usual to measure Euler angles by an electronic compass or an INS. Also, an AUV absolute velocity is directly sensed by using DVL or indirectly achieved by position differentiation. The DVL can measure the vehicle's relative velocity to the flow, but the result is less accurate since the DVL can only lock the water column some distance away from the vehicle body, caused by the DVL blanking distance. So, here it is assumed that the relative velocity of the AUV to the fluid is not measurable. The observer was designed using the measurement of output y as follows:

$$\dot{\hat{x}} = \hat{f}(\hat{x}, u) + G(\gamma, K)(y - C\hat{x}) \tag{3.7}$$

where $\hat{x}(t) \in \mathbb{R}^n$ is the estimate of $x(T)$; observer gain, $G(\gamma, K) := [\gamma k_1 \gamma^2 k^2 ... \gamma^n k_n]^T$ with $K := [k_1 k_2 ... k_n]^T, k_i \in R$ and $i = 1, 2, ..., n$ [45]. Since f is a known function of f(x, u) it is taken that $\hat{f} = f$. From Equations 2.6 and 2.7, the estimation error dynamics was expressed as follows:

$$\dot{\hat{e}}(t) = (A - GC)\hat{e}(t) + f(x(t), t) - \hat{f}(x(t) - \hat{e}(t), t) \tag{3.8}$$

The stability of the error dynamics was investigated via a Lyapunov function. Furthermore, since (A, C) is observable, there exist $\lambda > 0, K \in \mathbb{R}^n$ and a symmetric positive matrix $P \in \mathbb{R}^{n \times n}$ such as in Equation 3.9 which could be treated by solving the equivalent LMI as expressed in Equation 3.10.

$$(A - KC)^T P + P(A_K C) + \lambda I < 0 \tag{3.9}$$

$$A^T P + PA - C^T Y^T - YC + \lambda I < 0 \tag{3.10}$$

where the unknowns are $\lambda > 0$, $Y = PK \in \mathbb{R}^n$ and $p > 0$.
In order to solve the given system of LMIs, a series of MATLAB functions were adapted. A function `setlmis` was used for initializing the LMI internal representation. New matrix variables P, Y and λ in the LMI system were defined by the function `limvar`. The LMI term indicates the fundamental add-on terms regarding to the block-matrix expression of the LMI. More details for the `lmiterm` function description, see [15]. Once the given LMI system was described by using lmivar and lmiterm, the command `getlmis` determined the LMI's inherent representation `lmisys`. The system of LMIs described by lmisys had a solution `xfeas` which was computed by the function `feasp`. In other words, the vector `xfeas` is a value of the decision variables and all LMIs are satisfied for vector `xfeas`. Given the value `decvars` of the vector of decision variables, the relating value `valx` of the matrix variable with identifier X was computed by the function `dec2mat`. Subsequently, matrix variables - P, Y and λ in the LMI system were attained, then the gain parameter K was calculated by using P and Y [40]. By solving the LMI problem, the high-gain observer was designed, and

the gain and γ were determined as follows:

$$\lambda = 2.7408, K = \begin{bmatrix} 2.2616 & 0 & 2.8609 \\ 0 & 1.6410 & 0 \\ -0.7642 & 0 & 2.1939 \\ 0 & 0.1007 & 0 \\ -0.2669 & 0 & -0.9479 \\ 0 & 0.5343 & 0 \\ -9.9621 & 0 & 4.3196 \\ 0 & 1.7590 & 0 \\ 2.5424 & 0 & 4.1070 \end{bmatrix}$$

3.3 Results and Discussion

This section describes the validation of the proposed HGO by numerical simulations and experimental field tests.

3.3.1 Numerical Simulation

The AUV model applied in this simulation is outlined in reference [38]. The AUV of this model has a prolate spheroid hull shape, is 1.33-meter-long with a fitness ratio of 7:1. The propeller is fixed so that the nominal speed is greater than zero. The attitude of the AUV is controlled by the rudder and elevators through proportional- derivative (PD) feedback [14]. It is assumed that the AUV operated in a nonuniform flow expressed as:

$$V_f(X) = [-0.4, -0.3\sqrt{1 + x/500}, 0]^T \tag{3.11}$$

The AUV was simulated to accomplish a zigzag path from the starting point northwards in the horizontal plane. The heading reference is shift from ψ = 15 to ψ = -15 every 100 seconds. The vehicle departs at $X = [-500, 0, 0]^T$ with original orientation of $\phi = \theta = \psi$ = 0 . The horizontal trajectories resulted from two scenarios: with and without current disturbance. They are illustrated in Figure 3.2.

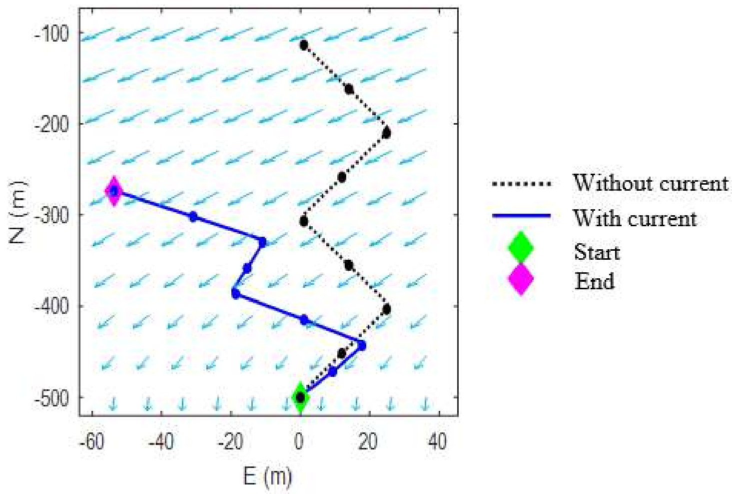

Figure 3.2: AUV paths in inertial frame in horizontal plane

There is a significant discrepancy between the two trajectories which resulted from the disrupted vehicle's absolute velocity as a result of the current. In Figure 3.3, it can be seen that the vehicle's absolute velocities were affected by the current. While the longitudinal absolute and relative velocities, u and u_r are nearly even at 0.6 m/s and 1 m/s respectively, the lateral absolute speed, v fluctuates as the vehicle changed its heading, thus putting it into a cross current situation.

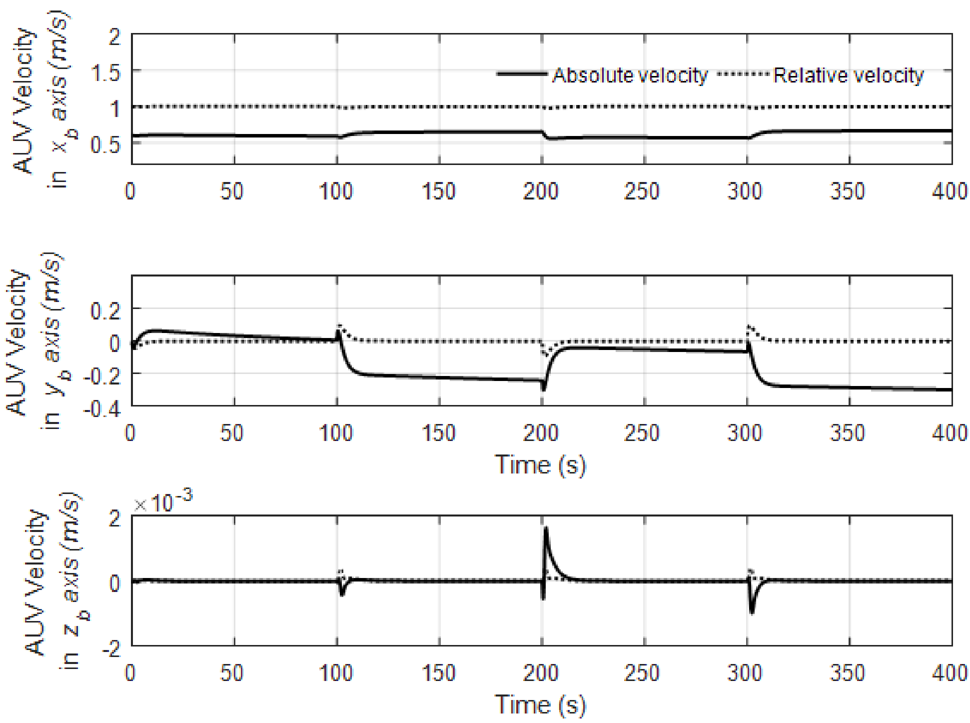

Figure 3.3: Vehicle's absolute and relative velocities in x_b, y_b and z_b axes in the body frame reference

The AUV's velocities relative to the flow were estimated by the HGO which utilized the measurement of Euler angles as shown in Figure 3.4. The relative velocity estimates generally show agreement with the actual relative velocities, although a peaking phenomenon exists in the transient behavior.

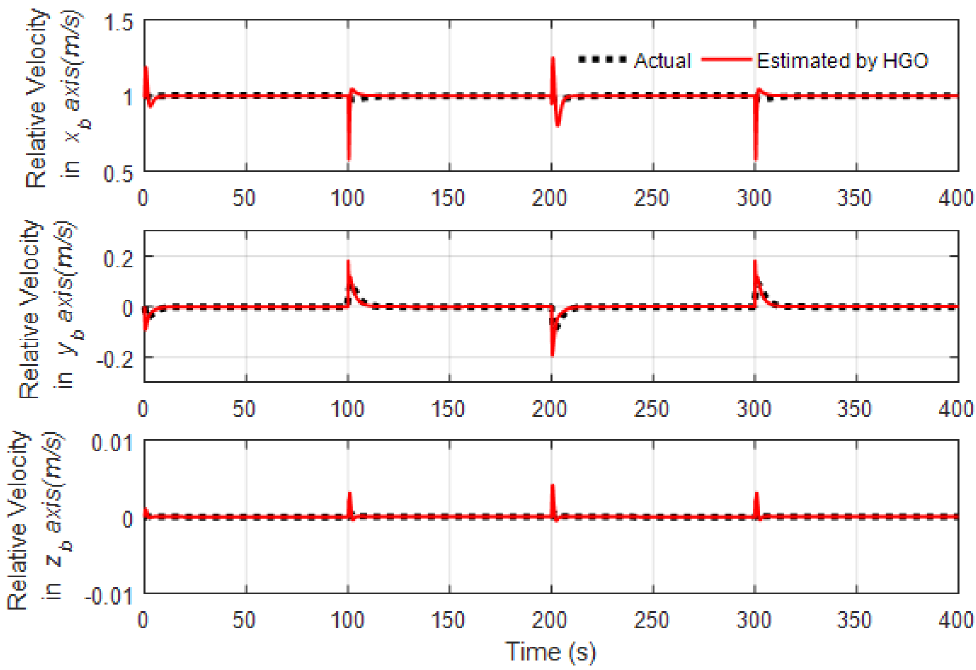

Figure 3.4: Comparison between actual and estimated relative velocities in the x_b, y_b and z_b axes in the body frame reference

Once the vehicle's relative velocities are estimated by using the HGO, then the current velocities can be obtained by subtracting the vehicle's relative velocities from the absolute velocities. It was assumed that the absolute velocities of the vehicle are available with the DVL in operation. As shown in Figure 3.5, current velocities in the x_b, y_b and z_b axes in the inertial reference frame were estimated and these generally matched the actual current.

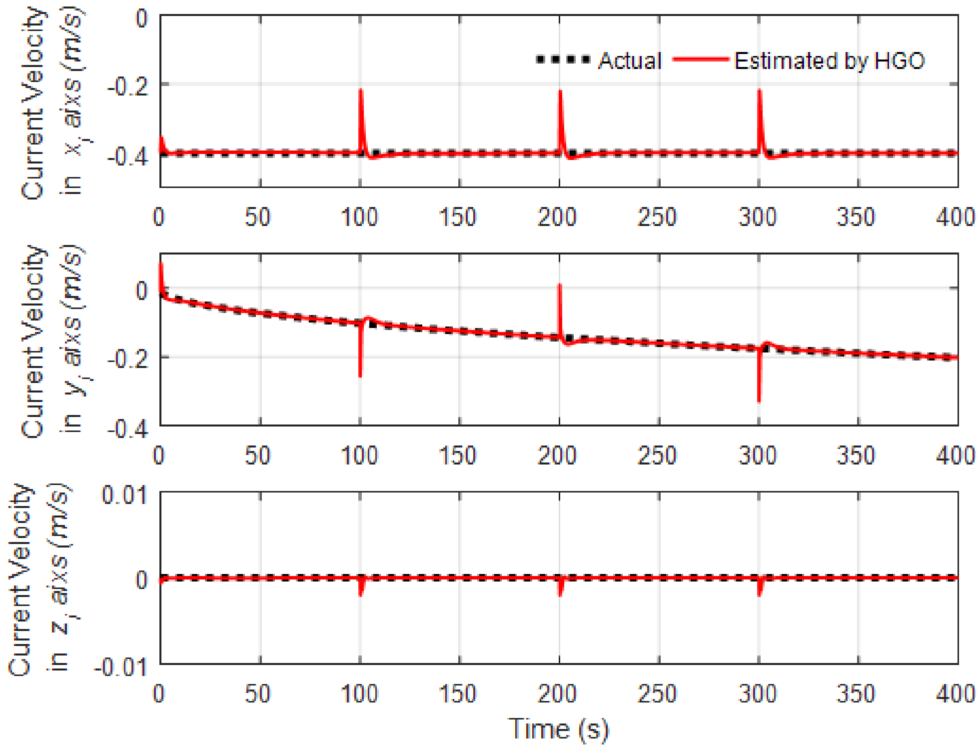

Figure 3.5: Comparison between actual and estimated current velocities in the x_b, y_b and z_b axes in the body frame reference

In order to study effectiveness of the HGO using the LMI, current velocity estimates from both the HGO using the LMI and the HGO using the pole placement to generate observer gain [14] were compared as shown in Figure 3.6. Estimated current velocity in the x_i axis clearly shows that the HGO using the LMI can estimate current velocity with a lower peaking phenomenon than the pole placement method. The differences between the actual current velocity and the estimated current velocity from the LMI approach are represented by standard deviations of 0.0128 m/s, 0.0038 m/s and 0.0001 m/s while their counter parts using the pole placement method are 0.0285 m/s, 0.0070 m/s and 0.0002 m/s in the x_i, y_i and z_i axes in the body frame reference system respectively.

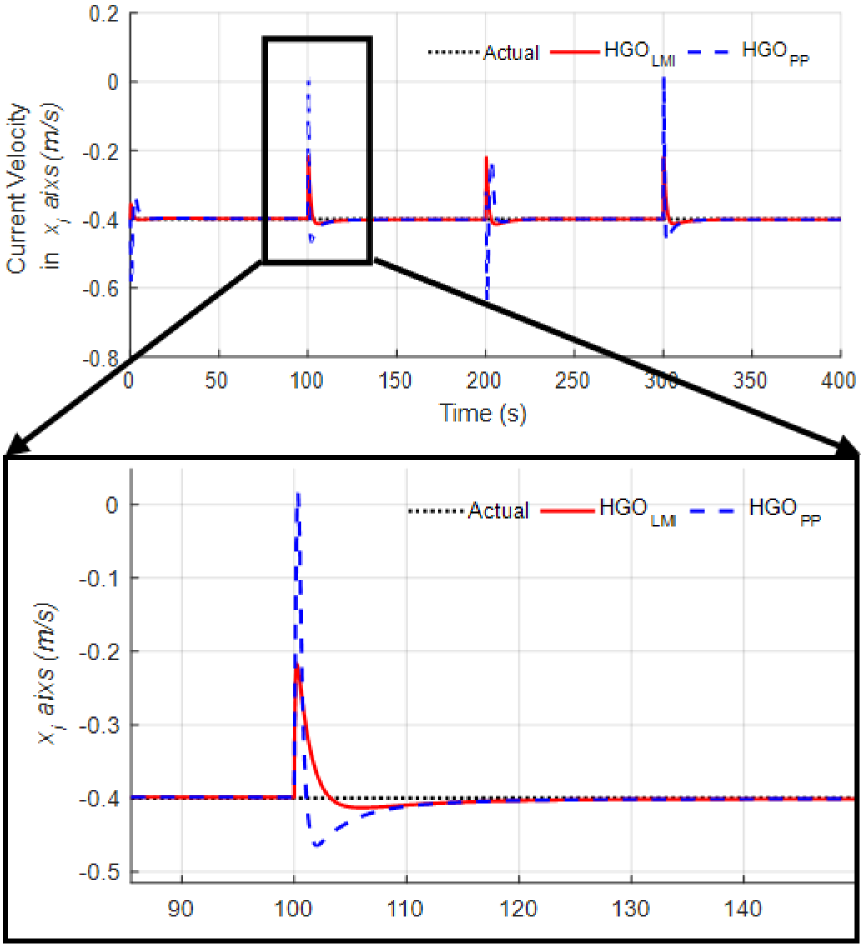

Figure 3.6: Comparison between current velocity estimates in the x_i axis in the inertial frame from both HGO and observer using pole placement

Furthermore, an estimation error ratio was calculated according to Equation (13) to see the improvement of the proposed HGO using the LMI to estimate the current velocity compared with HGO using the pole placement method.

$$Estimation\ error(\%) = (V_{Act} - V_{Est})/V_{Act} \times 100 \tag{3.12}$$

where V_{Act} is the actual current velocity and V_{Est} is the estimated current by observer. The current estimation errors of HGO using the LMI are considerably less than counter parts of the pole placement method in x_i and y_i axes shown in Figure 3.7.

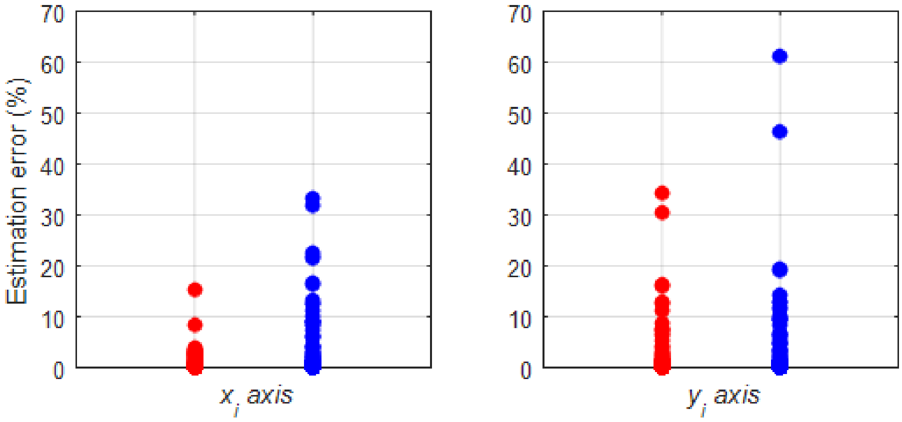

Figure 3.7: Estimation error distributions of two observers for current velocity estimates in x_i axis (LEFT) and y_i axis (RIGHT) in the inertial reference frame.

In Table A.1, estimation error means from the current estimation results for the HGO using the LMI and the pole placement method are tabulated. The estimation error means of the HGO using the LMI are smaller than the pole placement method in both x_i and y_i axes, which contribute an estimation improvement of 45 % and 1% respectively.

Table 3.1: Example table for summarized data.

Estimates error mean of	x_i axis	y_i axis
HGO using the LMI	0.6217 %	1.5666 %
HGO using the pole placement	1.2187 %	1.5833 %
Estimation improvement of HGO using the LMI	44.92 %	1.05 %

As mentioned in the previous section, the absolute velocity of the vehicle was assumed to be measured and used to estimate the current velocity. In the measurement process for the absolute velocity of the vehicle, an additive white process noise had been taken into account. It was assumed that the AUV operated in a nonuniform flow expressed as follows:

3.3.2 Experimental Test

The proposed HGO design was validated through field tests by comparing between the estimated current velocities and recorded current velocities from an on-board ADCP. A Gavia-class modular AUV was used for the field tests. Its dimensions were overall length 2.7 m, diameter 0.2 m, and dry weight in air around 70 kg [27]. The AUV was composed of a nose cone, battery module, sonar module, ADCP/DVL model, INS module, control module and a propulsion module. Two ADCP/DVLs were set up upward-looking (ADCP mode) and downward-looking (DVL mode) configurations. For the field tests, the AUV had a straight-line, consistent altitude mission at 10 m depth as illustrated in Figure 3.8.

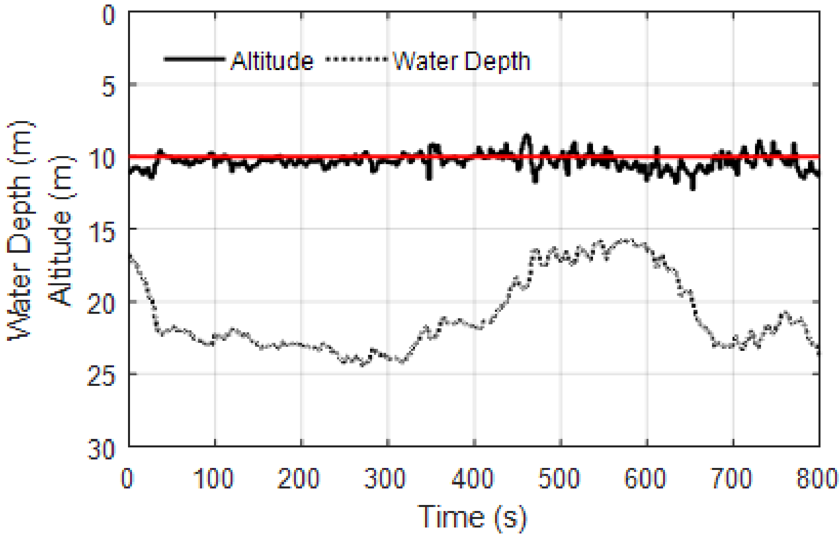

Figure 3.8: Depth of water and altitude of the AUV during the field test.

The hydrodynamics parameters for the AUV model were identified by adapting a recursive least squares (RLS) method identification. The identified parameters determined according to the inputs of the simulation varied, and the vehicle's velocities through the water were estimated by the model-based observer. The vehicle's relative velocities through the water were firstly estimated by the high-gain observer based on the AUV dynamic model. Subsequently the current velocities could be calculated by calculating the difference between the estimated relative velocities and the vehicle's absolute velocities over the ground measured by the DVL. The vehicle's absolute velocity recorded by the DVL-aided INS navigation system during the field test is shown in the dotted line in Figure 3.9 while the relative velocity estimated by the HGO is shown in the solid line. Only x_i direction are presented in this chapter due to space limitation, and x_i direction is chosen since the longitudinal direction showed the most dominant current velocity. The desired reference line which the AUV followed for the filed test was near the shore and against the direction of tidal flow.

The estimated current velocity by the HGO is shown in the red solid line while the measured current velocity from the ADCP in the x_i axis in the inertial frame is shown in the dotted curve in Figure 3.10. The current velocities were measured few distance away from the AUV due to the ADCP's blanking distance. However, the estimated current velocity from the HGO closely matched up with the measured current velocities. A peaking phenomenon was noted in the estimated current velocity right after the start of the test, but the transient period was quite short compared to the time scale and the estimated velocity reached the measured current velocity very quickly.

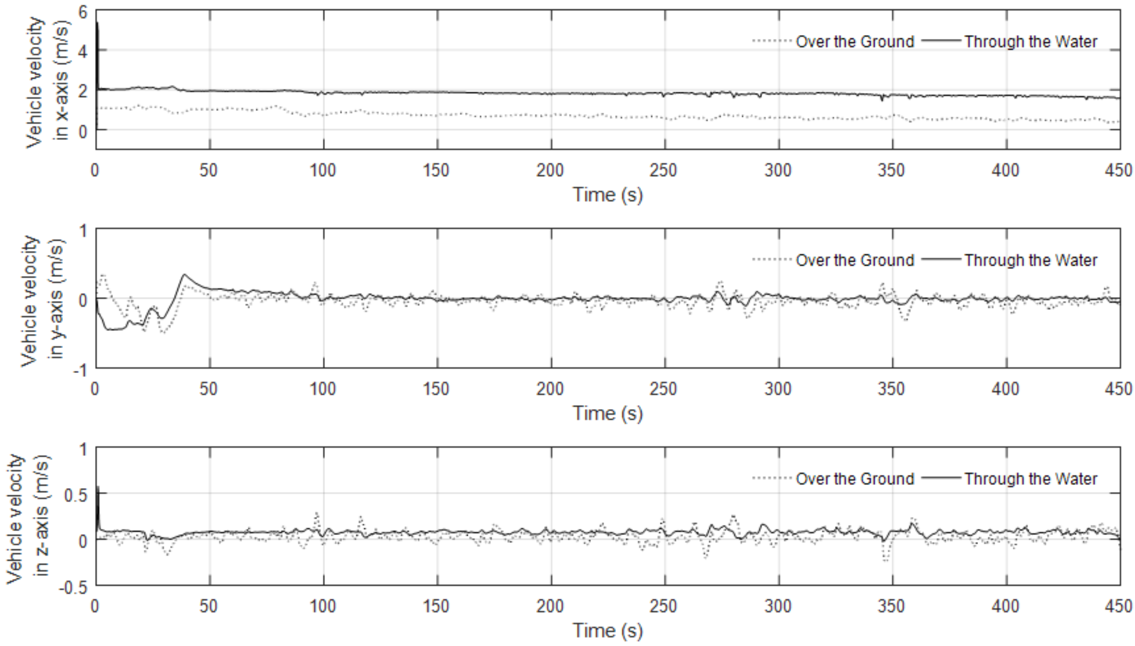

Figure 3.9: The vehicle's absolute velocity measured by DVL-aided INS and relative velocities estimated by AUV model-based HGO along the x_i axis.

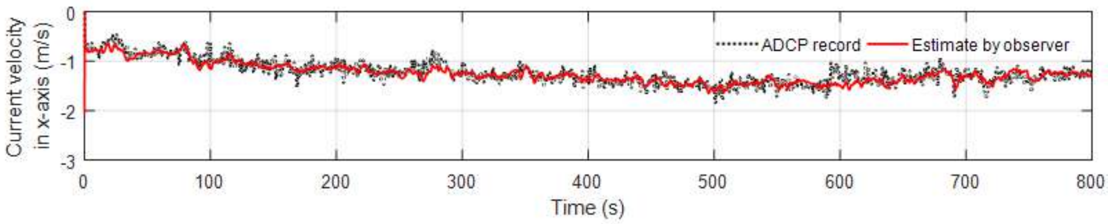

Figure 3.10: The current velocities measured by ADCP and its counterpart which was estimated by the HGO in the x_i axis.

In order to study the accuracy of the current estimates, the standard deviations between the current velocity estimate from the HGO and the current velocity measured by the ADCP were quantified as 0.0942 m/s in the x_i, axis of the inertial reference frame.

3.4 Conclusions

In this chapter, the current velocity in the x_i, y_i and z_i axes of the inertial reference frame were estimated to validate the performance of an AUV dynamic model-based high gain observer for estimating current velocities around the AUV. The current velocities were estimated by calculating the difference between the vehicle's absolute velocities over ground and the relative velocities through the water estimated from the AUV model-based HGO.

The nonlinear observer for current estimation based on the AUV dynamic model has been enhanced by applying a high-gain. The observer gain was obtained by solving the LMIs representing the error dynamics equation. In the numerical simulation, the vehicle's relative velocities were firstly estimated through the HGO and then the current velocity was further calculated by subtracting the vehicle's relative velocities from the absolute velocities. The estimated current velocities were well matched with the actual current velocities. The estimated current velocities and actual current velocities were compared by quantifying standard deviations as 0.0128 m/s, 0.0038 m/s and 0.0001 m/s for the x_i, y_i and z_i axes in inertial reference frame. The estimation error means of the HGO using the LMI have smaller values than using the pole placement method in both xi and yi axes which results in an estimation improvement of 45 % and 1 % respectively.

To validate the HGO, a series of the AUV missions were conducted with a straight-line and constant altitude condition. The current velocities were measured by the on-board ADCP while the vehicle velocities were measured by DVL. The vehicle's relative velocity in x_i axis was calculated by using the control commands executed during the field test. Subsequently the current velocity in x_i axis was estimated by obtaining the difference between the vehicle's relative velocity calculated by the HGO and the vehicle's absolute velocity recorded by the DVL-aided INS. The estimated current velocity in xi axis in the inertial reference frame was well agreed with the measured current from the AUV-onboard ADCP. The differences between the estimated and measured current velocities was quantified using standard deviations as 0.0942 m/s.

For more accurate navigation and control of the AUV, it is crucial to have the current velocities close to the AUV where the ADCP is impotent to measure because of its blanking distance. Thus, the high-gain observer based on the AUV model is beneficial for estimating the current velocities either close to or at the vehicle by taking advantage of the dynamic model in currents with precise hydrodynamics properties.

For precise navigation and control of an AUV, it is critical to obtain the current velocities around the boundary layer of the AUV where the ADCP is unable to measure due to its blanking distance. Hence the AUV model-based observer is advantageous to estimate the current velocities either close to or at the vehicle by utilising an AUV dynamics model. Precise hydrodynamics properties can be identified from the real-time measurement.

Chapter 4

Path Following for an AUV by Using a High-Gain Observer Based on an AUV Dynamic Model

This chapter is based on the journal article 'Path Following for an Autonomous Underwater Vehicle (AUV) by Using a High-Gain Observer based on an AUV Dynamic Model' and 'Current Estimation and Path Following for an Autonomous Underwater Vehicle (AUV) by Using a High-Gain Observer Based on an AUV Dynamic Model', which are published in the journal '*IFAC-PapersOnLine*' and '*International Journal of Control, Automation and Systems*' respectively. The citations for the articles are:

E. Kim, S. Fan, N. Bose and H. Nguyen, Path Following for an Autonomous Underwater Vehicle (AUV) by Using a High-Gain Observer based on an AUV Dynamic Model", *IFAC-PapersOnLine*, 2019, [3].

E. Kim, S. Fan, N. Bose and H. Nguyen. Current Estimation and Path Following for an Autonomous Underwater Vehicle (AUV) by Using a High-Gain Observer Based on an AUV Dynamic Model. *International Journal of Control, Automation and Systems*, 2020, [4].

In chapters 2 and 3, the high-gain observer based on the AUV dynamic model was introduced to the Gavia AUV and the Dolphin II AUV models respectively. Based on the developed high-gain observer, a path following problem for AUVs under a nonuniform current is presented in this chapter using the Dolphin II AUV model. A dynamic model of an AUV in a nonuniform flow was adopted to present a high-gain observer (HGO) for estimation of the three-dimensional current velocities along AUV trajectories. The HGO was chosen as a nonlinear estimation algorithm, and the observer gain was computed by solving a Linear Matrix Inequality (LMI) which represented the estimation error dynamics. The current velocities were determined by calculating the differences between the measured absolute velocities of the vehicle and the estimated relative velocities of the vehicle estimated by the observer. The estimation error means of the HGO using the LMI have smaller values than the state observer with a gain matrix determined by the pole-placement approach. For the path following study, the desired curved path was represented by using a Serret-Frenet frame which propagated along the curve. The path-following system includes a guidance law, an update law and a proportional and integral controller. Two cases of numerical simulations were conducted to verify the performance of the path following system combined with HGO for current compensation, and the results of both cases have shown that the AUV reached and converged to the desired path.

4.1 Introduction

Autonomous underwater vehicles (AUVs) have been extensively used over the past several decades in numerous applications across various fields. One reason for this is AUVs can perform unpredictable and dangerous marine operations. These AUVs application fields are search, rescue, surveillance, reconnaissance and exploration, pipeline construction, marine survey and mapping, geological sampling, resource development, etc [46]. To complete AUV missions successfully, it is critical to design an efficient and robust motion control system. It is a challenging task to achieve this due to the model's nonlinearity, uncertain hydrodynamic coefficient and unpredictable external disturbances caused by ocean currents, wind and waves [47].

The control, or more specifically motion control is the action of determining the necessary control forces and moments to be provided for the AUV to satisfy a certain control objective. Thus, when designing a motion control system, the control objective must be well defined to satisfy the required specifications for safe operation [11]. The elements of a motion control objective are point stabilization, path following and trajectory tracking. This chapter addresses a vital ability for an AUV to follow a predefined curved path in the presence of a nonuniform ocean current.

The performance of path following is mainly dependent on the guidance system, and a line-of-sight (LOS) guidance law is one of the popular and effective ways for kinematic guidance control, which mimics an experienced sailor on a vessel [48]. However, when the vehicle is under the presence of unknown external disturbances, the traditional LOS guidance law exhibits limitations. To enhance the adaptability and path following performance, many of improved LOS guidance laws have been developed. In [49], a modified LOS guidance law with integral action is proposed to counteract environmental disturbances. Paired with a set of adaptive feedback controllers, global asymptotic path following of straight-line paths in the constant and irrotational ocean currents is guaranteed. In [50], 3D LOS guidance law with integral action is studied, which counteracts the current by allowing the vehicle to side-slip and pitch while keeping the desired course. However the path following problem is discussed at the kinematic level only in this study. A 3D LOS guidance law with two integrators and three feedback controllers is proposed by [51] to successfully counteract the drifting caused by unknown current. As the vehicle dynamics are defined in terms of relative velocities, no adaptation laws are required, and the closed loop system is analysed through Lyapunov techniques. Furthermore, the integral LOS(ILOS) guidance law and the vector field (VF) guidance law are compared based on experimental results on light or long range AUV (LAUV) and the cross track error measurements as well as the servo command signals in the extended work by [52]. Both result in good path following performance, but VF controller performs slightly better despite rudder chattering. In [53], a nonlinear adaptive path following algorithm for estimation and compensation of the sideslip angle is presented. The adaptive guidance law is based on the LOS and integral action obtained by parameter adaptation. In [54], the integral LOS guidance method for path following of underactuated marine vehicles are extensively analysed. The 3D ILOS guidance law which embeds integral action in both vertical and horizontal direction is proposed, and closed loop analysis provides explicit conditions on the design parameters. The proposed ILOS guidance law has been validated via simulation and experiments using the Cooperative autonomous robotics towing system (CART) surface vehicle and the LAUV. A direct and indirect nonlinear adaptive path-following controller based on a LOS guidance principle are studied for marine craft in [55]. Two paths for AUVs, rectilinear and curvilinear, are tested to show effective compensation for time-varying drift force caused by waves, wind, and ocean currents. In [56], a fuzzy iterative sliding mode control (FISMC) scheme is introduced for 3D path following of AUVs with large scale, large inertia and high speed. The control algorithm introduces a fuzzy control to optimise the control parameters online to enhance the adaptability of the system with consideration of system uncertainties and environmental disturbances. The robustness and self-adaptability of the proposed FISMC are validated through numerical simulation of the AUV. In [57], a path variable is introduced to represent the curvilinear abscissa on the path, and the guidance law is designed such that the vessel can reject constant unknown ocean currents by the observer.

The Serret-Frenet frame is frequently employed to obtain the error dynamics equation which represents the path following error. In [58], the path following control method for an unmanned surface vehicle (USV) under the influence of unknown ocean currents is presented by extending the work by [59]. A virtual Serret-Frenet reference frame is introduced, which anchored in and propagates along the desired path. The guidance and update laws are used to drive the Serret-Frenet frame along the path, and combining with observer and controller, convergence of the desired path is achieved. In [60], the path following problem for an underactuated USV is addressed in the Serret-Frenet frame. By introducing the Serret-Frenet frame and global coordinate transformation, the control problem of the underactuated system is transformed into the actuated control problem. Comparative simulations show that a backstepping adaptive sliding mode controller (BADSMC) is insensitive to uncertainties, and had better dynamic performance, adaptability and robustness. In [61], the problem of 3D path following for the AUV in the presence of current disturbance is presented. To make the AUV follow the desired path, a path following error model of the AUV is established in the Serret-Frenet coordinate frame, and virtual guiding speed is designed based on backstepping and Lyapunov stability theory. The performance of the proposed damping backstepping controller is analysed and compared with the counterpart of a traditional backstepping controller, and simulation results show clearly that the damping backstepping control method has better ability and robustness under current disturbance and a bounded dynamic uncertainty.

As mentioned previously, more precise dynamic modelling has become important for control systems and state estimation algorithms as applications of AUVs have expanded into more dynamic and constrained environments including coastal areas and shallow water. Instead of making the assumption that the current is absent or constant, a flow field was assumed to comprise of an unsteady component and a nonuniform component in [62]. Under this assumption, the full dynamic model of an AUV in currents derived which leads towards identification of more accurate flow characteristics by the use of an observer design. In [63], both kinematic and dynamic models of an AUV are established in ocean currents. The kinematic model was developed in terms of the relative velocity with respect to the ocean current disturbances while the dynamic model was developed to include the influences of ocean current-induced uncertainties. But the motions in heave, roll, and pitch directions are neglected, so that only a 3 degrees of freedom (DOF) dynamic model of an AUV in the horizontal plane was used. Using this kind of AUV modelling method, the trajectory tracking problem was discussed with both kinematic control and dynamic control.

The nonlinear observer distinguishes itself from other methods by its simple structure since it only consists of a copy of the system dynamics with a corrective term involving the product of the output observation error by the observer gain. As a result nonlinear observers have been used extensively in the feedback control design for nonlinear systems; see [32] for example. In order to estimate the current velocity, the nonlinear observer based on an AUV dynamic model in current is used in [14]. However, as the most critical parameter, the observer gain is preliminarily obtained by utilising the pole placement method with arbitrarily chosen regulator poles in [14].

The pole-placement is the problem of placing the regulator poles (closed-loop poles) at the desired location. As long as a necessary and sufficient condition for arbitrary pole placement are met, the system can be completely state controllable. It is worthy to note that the gain matrix is not unique for a given system, but depends on the desired closed-loop pole locations which determine the speed and damping of the response. In other words, the selection of the desired closed-loop poles or the desired characteristic equation is a compromise between the rapidity of the response of the error vector and the sensitivity to disturbances and measurement noises [64].

A high-gain observer (HGO) based model predictive control (MPC) is developed for cross tracking the underactuated AUVs under current disturbances in [65]. The HGO is used to estimate the current velocity, external force and torque, the MPC is designed based on the disturbance estimate. However, the observer is derived at the kinematic level in 2-D horizontal plane. The dynamics of surge is neglected, and the surge velocity is assumed to be constant.

On the same line, the high-gain observer (HGO) based on an AUV dynamics model in currents is presented to obtain three-dimensional water current velocities estimates, but the observer gain for the HGO is determined by solving the Linear Matrix Inequality (LMI) describing the estimate error dynamics in [2]. The performance of high-gain observer design is validated by comparing the simulation and field trial results [1]. This chapter aims to estimate the current velocity using the HGO and achieve the path following performance for an AUV with current compensation in consideration. The major contributions of the chapter are as follows:

- Firstly, the high-gain observer (HGO) is developed for a class of systems with Lipchitz nonlinearities to estimate the current velocity. The convergence of the estimation error of the proposed observer has been studied by means of both Lyapunov functions and functionals in [66]. The LMI is utilised to express the stability conditions. The path-following by the HGO is shown to outperform than the counterpart by the state observer using the pole placement through two sets of simulations.

- Secondly, the control method is improved by extending [67] to obtain curved path following performance for AUVs under the influence of unknown ocean currents. This is achieved by implementing the guidance law together with the current observer. The closed-loop system consists of a feedback linearized controller, and the desired path is represented by a Serret-Frenet reference frame in 6-DOF.

This chapter is organised as follows: Section 4.2 is devoted to clarifying the AUV dynamics model. The control objectives and the control system including the observer, update and guidance laws and controllers are presented in Section 4.3 and 4.4 respectively. Simulation results are presented in Section 4.5 followed by the conclusion in Section 4.6.

4.2 Vehicle Model

This section describes the 6 DOF manoeuvring model for an underactuated AUV moving in 3D space and formulates the problem of 3D path following of space curves.

4.2.1 Kinematics

Let $\mathbf{X} = [x \quad y \quad z]^T$ represent the position vector from the origin of the Earth-fixed reference frame $\{i_1,\ i_2,\ i_3\}$ to the origin of a body-fixed frame $\{b_1,\ b_2,\ b_3\}$ illustrated in Figure 4.1. The vector $\mathbf{X}$ is the North-East-Down coordinates in the inertial frame.

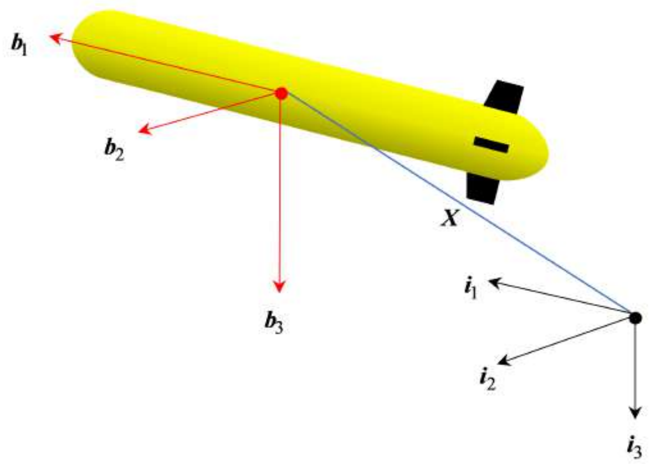

Figure 4.1: AUV's body-fixed and Earth-fixed reference frames.

The vector $\eta = [\phi \quad \theta \quad \psi]$ denote the orientation represented by means of Euler angles relative to the inertial reference frame. The translational and rotational velocities of the vehicle are presented as $\nu = [u \quad v \quad w]$ and $\omega = [p \quad q \quad r]$ expressed in the body frame with respect to the inertial frame. The kinematic equations are [42]:

$$\begin{aligned} \hat{X} &= R(\eta)\nu \\ \hat{\eta} &= J(\eta)\omega \end{aligned} \tag{4.1}$$

$$R(\eta) = \begin{bmatrix} c\theta c\psi & -c\phi s\psi + s\phi s\theta c\psi & s\phi s\psi + c\phi s\theta c\psi \\ c\theta s\psi & -c\phi c\psi + s\phi s\theta s\psi & -s\phi c\psi + c\phi s\theta s\psi \\ -s\theta & c\theta s\phi & c\theta c\phi \end{bmatrix}$$
$$J(\eta) = \begin{bmatrix} 1 & s\phi t\theta & c\phi t\theta \\ 0 & c\phi & -s\phi \\ 0 & s\phi/c\theta & c\phi/c\theta \end{bmatrix}$$

where $s\cdot = \sin(\cdot)$ and $c\cdot = \cos(\cdot)$.

The vehicle model is based on following assumptions:

Assumption 1 The motion of the AUV is described by 6-DOF, which are surge, sway, heave, roll, pitch and yaw.

Assumption 2 The AUV is port-starboard symmetric.

Assumption 3 The vehicle's centre of mass (CM) is located at r_{cm}, and the origin on the body reference frame is located at the centre of buoyancy (CB); see Figure 4.1.

In this chapter, a flow field is considered to comprise two components : a steady, circulating flow component Vs(X) and an unsteady and uniform flow component $V_u(t)$ [41]. These two components can be expressed in body-fixed reference frame as follows:

$$\begin{aligned} \nu_s(R, X) &= R^T V_s(X) \\ \nu_u(R, t) &= R^T V_u(t) \end{aligned} \tag{4.2}$$

The complete flow field is $\nu_f(R, X, t) = \nu_s(R, X) + \nu_u(R, t)$.

4.2.2 Dynamics

Let ν the generalized vehicle's velocity while ν_s and ν_u represent the steady and circulating flow and unsteady and uniform flow respectively as follows:

$$\nu = [\upsilon \quad \omega]^T, \quad \nu_s = [\upsilon_s \quad 0]^T, \quad \nu_u = [\upsilon_u \quad 0]^T$$

The vehicle's velocity relative to the flow can be expressed as follows:

$$\nu_r = \nu - \nu_s - \nu_u = [\upsilon_r \quad \omega]^T$$

where $\upsilon_r = \upsilon - \upsilon_s - \upsilon_u = [u_r \quad v_r \quad w_r]^T$ is the vehicles velocity relative to the flow expressed in body-fixed frame.
By referring [44] and [68], the complete flow-relative dynamics of the vehicle can be obtained

$$\begin{aligned}(M_f + M)\dot{\nu}_r = &- \begin{bmatrix} \hat{\omega} & 0 \\ \hat{\nu_r} & \hat{\omega} \end{bmatrix} (M_f + M)\nu_r + \begin{bmatrix} f \\ m \end{bmatrix} \\ &- \begin{bmatrix} \hat{\omega} & 0 \\ \hat{\nu_r} + \hat{\nu_u} + \hat{\nu_s} & \hat{\omega} \end{bmatrix} (M - \bar{M}) \begin{bmatrix} \nu_u + \nu_s \\ 0 \end{bmatrix} \\ &- \begin{bmatrix} 0 & 0 \\ \hat{\nu_u} + \hat{\nu_s} & 0 \end{bmatrix} (M - \bar{M})\nu_r - \begin{bmatrix} \Phi & 0 \\ 0 & 0 \end{bmatrix} (M_f + \bar{M})\nu_r \\ &- (M - \bar{M}) \begin{bmatrix} (\nu_u + \nu_s)\omega + \frac{\partial}{\partial t}\nu_u + \Phi^T(\nu_u + \nu_s + \nu_r) \\ 0 \end{bmatrix}\end{aligned} \tag{4.3}$$

where $\Phi = R^T \left(\dfrac{\partial V_s}{\partial X} \right)^T R$. M is inertia matrix and M_f is generalized added inertia matrix for rigid vehicle. The generalized added inertia matrix is obtained by summing the added mass inertia matrix for the spheroidal hull and the matrix representing the added mass for the control planes. $\bar{M}$ denotes a mass matrix that accounts for the kinetic energy of the fluid that is replaced by the vehicle. Note that except the first line in Equation 4.3, rest terms illustrate the impact of current on dynamics of AUV. The external forces and moments exerting on the vehicle are explained in [42]. By incorporating the kinematic equation 4.1 with the dynamic equation 4.3, a complete dynamic AUV model in an unsteady, nonuniform flow field can be obtained. The AUV model used for the numerical simulation is described in [42].

4.3 Control Objectives

This section formalises the control problem. The control system should make the vehicle following a given smooth path P and maintain a desired constant relative surge velocity $u_{r,des}$ in the presence of unknown constant ocean current $V_c = [V_x \quad V_y \quad V_z]^T$. The path P is specified as by functions of the arc length s with respect to the inertial frame using a virtual Serret-Frenet frame f given by equation 4.4. While the position of the frame origin is described by $x_f(s)$,$y_f(s)$ and $z_f(s)$, the orientation of the path is defined by $\theta_f(s)$ and $\psi_f(s)$. $\alpha_f(s)$ and $\beta_f(s)$ describe the path curvature and torsion respectively.

$$P = \{x_f(s),\ y_f(s),\ z_f(s),\ \theta_f(s),\ \psi_f(s),\ \alpha_f(s),\ \beta_f(s)\} \tag{4.4}$$

As shown in Figure 4.2 the Serret-Frent frame is anchored in P and it propagates along P with instantaneous speed $\dot{s}$. The position of the vehicle is expressed with x_{bf}, y_{bf} and z_{bf} which is the position of the body frame b relative to the Serret-Frenet frame f , so when x_{bf}, y_{bf} and z_{bf} are zero, the vehicle is on the desired path [58]. Furthermore, the relative surge velocity u_r is required to maintain a desired constant relative surge velocity $u_{r,des}$. Therefore, the control objective can be defined as following equation 4.5.

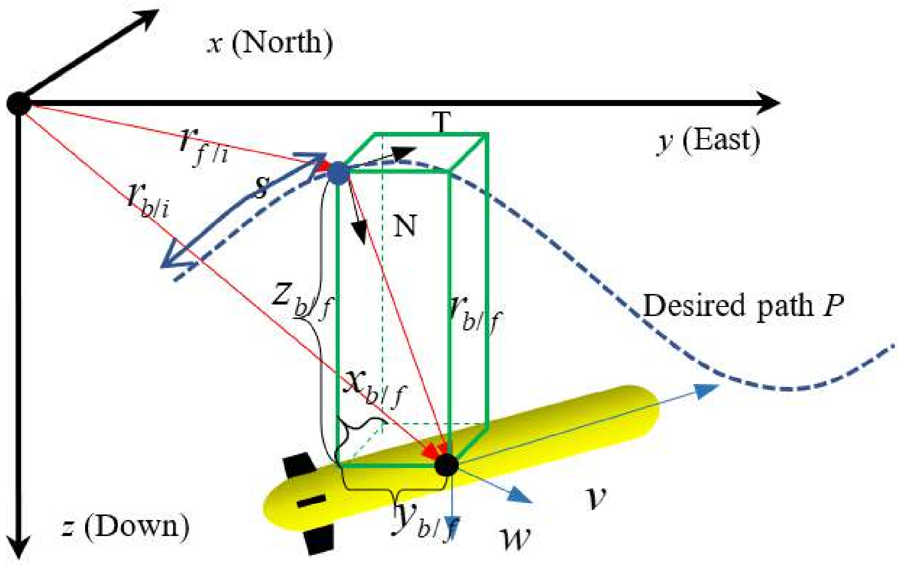

Figure 4.2: Illustration of Serret-Frenet for 3D path following: Serret-Frenet frame has axes denoted T and N and is anchored in the desired path. The position of the body frame relative to the Serret-Frenet frame is denoted $(x_{bf},\ y_{bf},\ z_{bf})$.

$$\begin{aligned} &\lim_{x\to\infty} x_{b/f} = \lim_{x\to\infty} y_{b/f} = \lim_{x\to\infty} z_{b/f} \\ &\lim_{x\to\infty} u_r(t) = u_{r,des} \end{aligned} \tag{4.5}$$

The dynamics of the body frame relative to the Serret-Frenet can be expressed as follows:

$$\begin{bmatrix} \dot{x}_{b/f} \\ \dot{y}_{b/f} \\ \dot{z}_{b/f} \end{bmatrix} = R_b^f(\Theta_{fb}) \begin{bmatrix} u \\ v \\ w \end{bmatrix} - \begin{bmatrix} \dot{s} \\ 0 \\ 0 \end{bmatrix} - \dot{s} \begin{bmatrix} 0 & -\alpha & 0 \\ \alpha & 0 & -\beta \\ 0 & \beta & 0 \end{bmatrix} \begin{bmatrix} x_{b/f} \\ y_{b/f} \\ z_{b/f} \end{bmatrix} \tag{4.6}$$

where α and β and described the path curvature and torsion respectively, and $R_b^f(\Theta_{fb})$ is the transformation matrix relating to the angle between the path P and the orientation of the body.

4.4 Control System

In this section a control system is presented to achieve the control objectives specified in previous section. As shown in Figure 4.3, the control system includes an observer, an update law for the Serret-Frenet reference frame, guidance laws for the attitude control and lastly controllers for surge, pitch and yaw control.

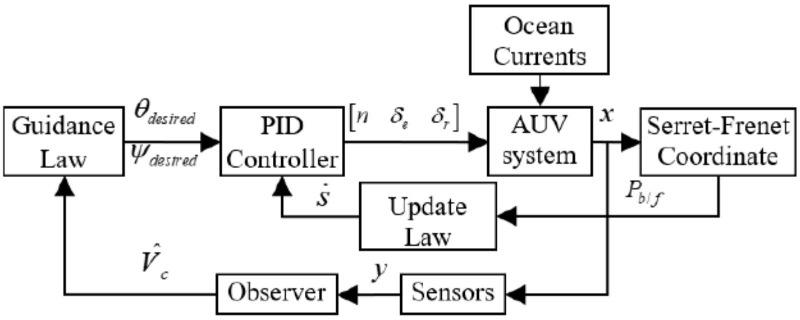

Figure 4.3: The proposed AUV path following control scheme

4.4.1 Observer Design

In this section, a HGO based on the AUV dynamics model is designed. To set up the nonlinear HGO, the AUV's dynamic systems are described by:

$$\begin{aligned} \dot{x} &= Ax + f(x, k, d) \\ y &= Cx \end{aligned} \tag{4.7}$$

where $x = [\phi \quad \theta \quad \psi \quad u_r \quad v_r \quad w_r \quad pqr]$ is the state vector; $k = [T \quad \delta_q \quad \delta_r]^T$ is a vector of controller inputs including the propeller force T and two rudder angles δ_q and δ_r (the deflection of elevator and rudder respectively); d denotes the current disturbances; y is the output vector; C is the measurement matirx as follows:

$$C = \begin{bmatrix} 1 & 0 & 0 & 0 & 0 & 0 & 0 & 0 & 0 \\ 0 & 1 & 0 & 0 & 0 & 0 & 0 & 0 & 0 \\ 0 & 0 & 1 & 0 & 0 & 0 & 0 & 0 & 0 \end{bmatrix}$$

Underwater vehicles are usually equipped with various sensors to measure or estimate the vehicle's states. For the proposed controller system, the vehicle's absolute velocities and Euler angles are required to be measured. The vehicle's absolute velocities can be directly measured by Doppler velocity log (DVL) or indirectly estimated by position differentiating while Euler angles can be measured by electronic compass or inertial navigation system (INS) [14].

To estimate , the observer is considered as follows:

$$\dot{\hat{x}} = A\hat{x} + \hat{f}(\hat{x}, \tau) + G(\gamma, K)(y - C\hat{x}) \tag{4.8}$$

where $\hat{x}$ is the estimate of $x(t)$ at time t ; the observer gain, G; $\hat{f}(\hat{x}, \tau)$ is a model of $f(x, t, d)$. The high gain was computed by solving the LMI which represented the error dynamics. The estimation error dynamics were derived from Equation 4.7 and 4.8 as follows:

$$\dot{\hat{e}}(t) = (A - GC)\hat{e}(t) + f(x(t), t) - \hat{f}(x(t) - \hat{e}(t), t) \tag{4.9}$$

By rearranging the Equation 4.9 with $\hat{e} := T(\gamma)e$, $e \in \mathbb{R}^n$ and $T(\gamma) = diag(\gamma,\ \gamma^2,\ \cdots\ \gamma^n)$ which results in Equation 4.10 as follows:

$$\dot{\hat{e}}(t) = T(\gamma)^{-1}(A - GC)T(\gamma)e(t) + T(\gamma)^{-1}\{f(x(t),t) - f(x(t) - T(\gamma)e(t),t)\} \tag{4.10}$$

Because of the particular observer structure, the previous equation was rewritten as follows:

$$\dot{\hat{e}}(t) = \gamma(A - KC)e(t) + T(\gamma)^{-1}f(x(t),t) - f(x(t) - T(\gamma)e(t),t) \tag{4.11}$$

The stability of the error dynamics was investigated via a Lyapunov function. Furthermore, based on the fact that (A,C) is observable, there exist $\lambda > 0,\ K \in \mathbb{R}^n$ and a symmetric positive matrix $P \in \mathbb{R}^{n\times n}$ such that

$$(A - KC)^T P + P(A - KC) + \lambda I < 0 \tag{4.12}$$

with $K := [k_1\ k_2\ \cdots\ k_n]^T$. The above equation could be treated by solving the equivalent LMI:

$$A^T P + PA - C^T Y^T - YC + \lambda I < 0 \tag{4.13}$$

where the unknowns are $\lambda > 0,\ Y = PK \in \mathbb{R}^n$ and $P > 0$.
In order to compute the solution to a given system of LMIs, a number of MATLAB functions were used. Before starting the description of a new LMI system, a function `setlmis` was used to initialise its internal representation. The function `limvar` defined new matrix variables P, Y and λ in the LMI system currently described. The variable matrix P was defined as a 6×6 symmetric matrix while Y was defined as a 6×3 rectangular matrix. One of the gain parameters, λ was defined as a constant. By using a function `limterm`, one term is added to a given LMI at a time. The LMI term referred to the elementary additive terms involved in the block-matrix expression of the LMI [1]. For more details for the `lmiterm` function description, see [40]. After completing the description of a given LMI system with lmivar and `limterm`, its internal representation `lmisys` was obtained with the command `getlims`. The function `feasp` computed a solution `xfeas` of the system of LMIs described by `lmisys`. The vector `xfeas` was a particular value of the decision variables for which all LMIs were satisfied. Finally, a function `dec2mat` computed the corresponding value `valx` of the matrix variable with identifier X given the value `decvars` of the vector of decision variables. As a result, matrix variables - P, Y and λ in the LMI system were obtained, then P and Y were used to calculate the one of gain parameter K.

4.4.2 Update and Guidance Laws

The Serret-Frenet frame propagates along the desired path, and let the distance the frame travels be s. By motivated by [67], the update law is introduced to update the distance

s. Since$\{f\}$-frame is a virtual reference frame, the update law can be freely chosen. The guidance law providing the pitch and yaw controller with their references are determined as following equations and explanation of the variables can be found in [67]:

$$\begin{aligned}\theta_{fc,des} &= \arctan\left(\frac{z_{z/f}+f}{\Delta^2+y^2_{b/f}}\right)\\ \psi_{fc,des} &= \arctan\left(\frac{y_{z/f}+g}{\Delta^2+x^2_{b/f}+z^2_{b/f}}\right)\end{aligned} \tag{4.14}$$

where f is the solution to the second order equation:

$$\underbrace{\left(\hat{V}_z^{f^2}-U^2_{des}\right)}_{a_f}f^2+2\underbrace{\left(\hat{V}_z^{f^2}z_{b/f}\right)}_{b_f}f+\underbrace{\hat{V}_z^{f^2}\left(\Delta^2+y^2_{b/f}+z^2_{b/f}\right)}_{c_f}=0 \tag{4.15}$$

and g is the solution to the second order equation:

$$\underbrace{\left(\hat{V}_y^{f^2}-\cos^2(\theta_{fc,des})U^2_{des}\right)}_{a_g}g^2+2\underbrace{\left(\hat{V}_y^{f^2}y_{b/f}\right)}_{bf}g+\underbrace{\hat{V}_y^{f^2}\left(\Delta^2+x^2_{b/f}+y^2_{b/f}+z^2_{b/f}\right)}_{cf}=0 \tag{4.16}$$

Above equations are second order equations, so there are two possible solutions for each equation:

$$i_1=\frac{-b_i-\sqrt{b_i^2-a_ic_i}}{a_i}, \quad i_2=\frac{-b_i=\sqrt{b_i^2-a_ic_i}}{a_i}$$

for $i=\{f,g\}$, so f and g are chosen as

$$f=\begin{cases}f_1 & \hat{V}_z^f\geq 0\\ f_2 & \hat{V}_z^f<0\end{cases}, \quad \begin{cases}g_1 & \hat{V}_y^f\geq 0\\ g_2 & \hat{V}_y^f<0\end{cases}.$$

4.4.3 Controllers

This section presents feedback linearization controllers that ensure the vehicle track the references for u_r, θ and ψ. The AUV model has three inputs T, δ_q and δ_r, which are the propeller force and two rudder angles of elevator and rudder. A feedback linearizing P-controller is used to ensure that the relative surge velocity u_r is tracking the desired velocity $u_{r,des}$. Similarly, the pitch and yaw controllers ensure tracking of the desired pitch angle θ_d and yaw angle ψ_d.

$$\begin{aligned}T &= -k_{ur}\tilde{u}_r\\ \delta_q &= -k_\theta\tilde{\theta}-k_q\dot{\tilde{\theta}}\\ \delta_r &= -k_\psi\tilde{\psi}-k_r\dot{\tilde{\psi}}\end{aligned} \tag{4.17}$$

where the errors are defined as $\tilde{u_r}=u_r-u_{r,des}$, $\tilde{\theta}=\theta_r-\theta_d$, $\dot{\tilde{\theta}}=q-\dot{\theta}_d$, $\tilde{\psi}=\psi-\psi_d$ and $\dot{\tilde{\psi}}=r-\dot{\psi}_d$,

4.5 Simulation Results

In this section two simulation cases are presented to verify the effectiveness of the path following guidance system and the high-gain observer for current estimation. In the first case, a straight-line was chosen for the desired path while a helix was used for the second simulation case. In all cases, the simulations were carried out with a modular AUV, Dolphin II developed by Zhejiang University [69] and the parameters for the AUV model are shown in Table A.1. The Dolphin II AUV hull is a prolate spheroid and 2-meter-long with a fineness ratio of 10:1. The four identical tail fins, arranged in a cruciform configuration, have an aspect ratio of 3; the tip-to-top span for each pair of fins is 34 centimetres. The parameters of the controller and the desired path configuration are presented in Table 4.2.

Table 4.1: Parameters of the Dolphin II AUV

m = 79.11 kg	length = 2 m	diameter = 0.2 m
$I_{xx} = 0.496\ kg \cdot m^2$	$I_{yy} = 30.95\ kg \cdot m^2$	$I_{zz} = 30.95\ kg \cdot m^2$
$r_{cm} = [0 \quad 0 \quad 0.2]^T$	$X_{\dot{u}} = 0.930\ kg$	$Y_{\dot{v}} = -52.111\ kg$
$Y_{\dot{r}} = 1.504\ kg \cdot m/rad$	$Z_{\dot{w}} = -51.551\ kg$	$Z_{\dot{q}} = -1.138\ kg \cdot m/rad$
$K_{\dot{p}} = -0.829 kg \cdot m^2/rad$	$M_{\dot{w}} = -1.138\ kg \cdot m$	$M_{\dot{q}} = -16.11\ kg \cdot m^2/rad$
$N_{\dot{v}} = 1.504\ kg \cdot m$	$N_{\dot{r}} = -16.355\ kg \cdot m^2/rad$	

Table 4.2: Parameters of the controller and desired path configuration

$k_{ur} = 1$	
$k_\theta = 1$	$k_q = 0.001$
$k_\psi = 1$	$k_r = 0.01$
$u_{r,des} = 4\ m/s$	Desired surge velocity
$\Delta = 20\ m$	Look-ahead distance
$R_{helix} = 400\ m/s$	Radius of helix
$h_{r,des} = 40\ m/s$	Vertical separation distance of helix

As mentioned in the previous section, the absolute velocity of the vehicle was assumed to be measured and used to estimate the current velocity. In the measurement process for the absolute velocity of the vehicle, an additive white process noise had been taken into account. It was assumed that the AUV operated in a nonuniform flow expressed as follows:

$$V_f(X) = [-0.5 \quad -0.5\sqrt{501 + x/500} \quad 0]^T \quad [m/s] \tag{4.18}$$

In the simulation, it was assumed that the AUV operated in a nonuniform current flow in which the velocity of the flow changed at different positions. However, animation was required to simulate the time-varying current state. Since the process to create the animated line simulator for the time-varying state is computationally expensive, the current used in the simulation was assumed to be nonuniform flow.

4.5.1 Case 1: Straight-Line Path

In the first case simulation, the AUV was required to follow a straight-line path as defined as:

$$P_1 := \begin{cases} x_f(s) = s\cos(\theta_f(s)) \\ y_f(s) = 0 \\ z_f(s) = s\sin(\theta_f(s)) \\ \theta_f(s) = \pi/12 \\ \psi_f(s) = 0 \\ \alpha_f(s) = 0 \\ \beta_f(s) = 0 \end{cases} \tag{4.19}$$

The result of the simulation for 200 seconds is shown in Figure 4.4. The trajectory of the AUV is shown by the blue line while the desired path is shown by the red dashed line. The cone shapes indicate the location and orientation of the AUV at 50 second intervals. It can be seen from Figure 4.5 that the AUV converged to the desired path within 50 seconds from the initial point [0, -30, 30]. The path-following errors in x, y and z directions are shown in Figure 4.5, which demonstrates that the path-following error converges to zero after a transient period.

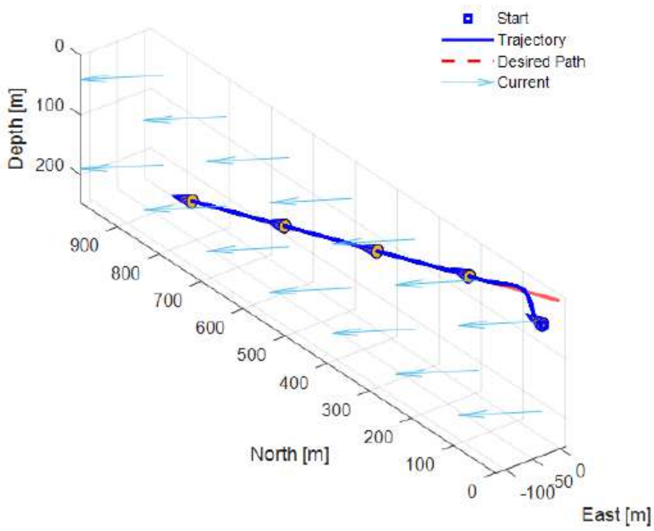

Figure 4.4: Actual trajectory of the AUV (solid blue curve) and the straight-line desired path (red dashed curve) in the NED coordinate system

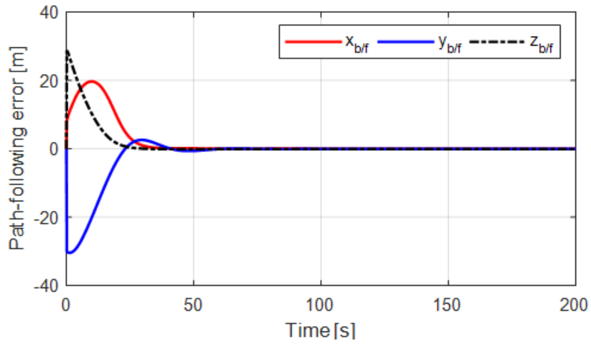

Figure 4.5: Time evolution of the path-following errors

Figure 4.6 shows the performance of the path-following guidance system in different conditions, such as the presence of current and the absence of current compensation (see Table 4.3). When the current is not accounted for in the path-following control algorithm, the vehicle will definitely drift away due to the current, as shown in Condition 2. The path following guidance system used in the simulation allowed the vehicle to converge towards the desired path regardless of the presence of current, as shown in Conditions 1 and 3.

Table 4.3: Four simulation conditions for current presence and compensation

	With current compensation	Without current compensation
With Current	Condition 1	Condition 2
Without Current	Condition 3	Condition 4

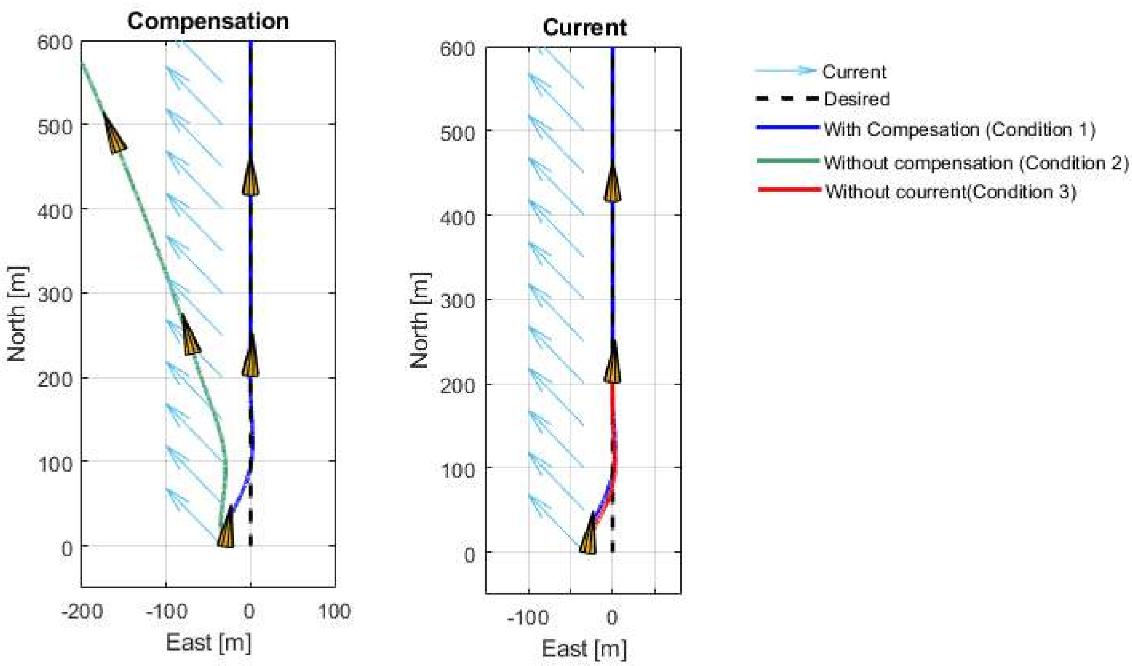

Figure 4.6: Comparison of the AUV trajectories in four different conditions with current presence and compensation

In Figure 4.7 the vehicle's absolute velocities over the ground were measured in m/s, and the vehicle's relative velocities were estimated by the HGO in the x_b, y_b, and z_b axes direction.

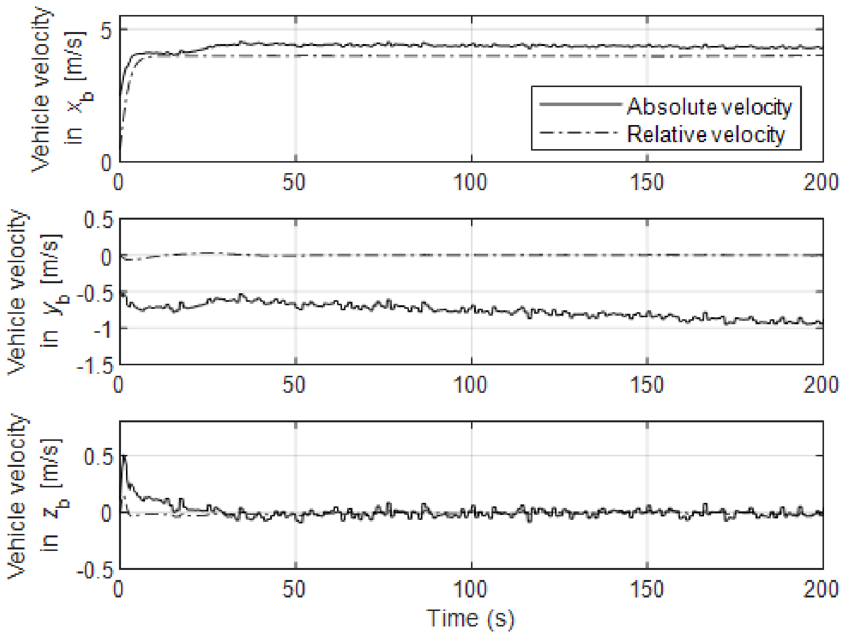

Figure 4.7: Vehicle's absolute and relative velocities in x_b, y_b and z_b axes in the body frame reference

The current velocity was obtained by subtracting the relative velocity estimated by the HGO from the measured absolute velocity as shown in Figure 4.8.

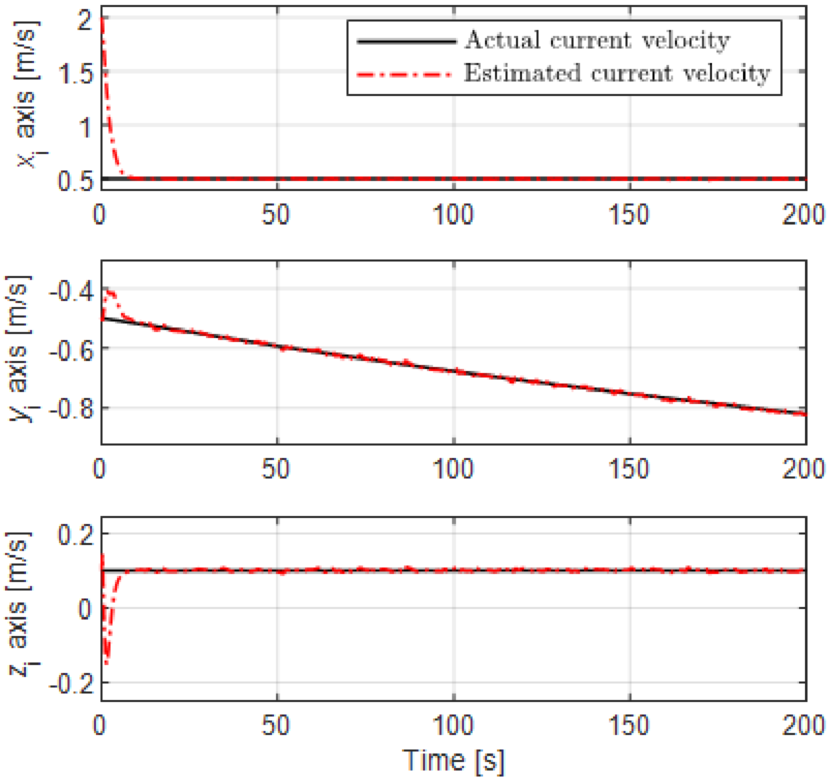

Figure 4.8: Comparison between actual and estimated current velocities in x_i, y_i and z_i axes for strait path

The estimated current velocities closely matched the actual velocities. The difference between the estimated current velocity and the actual velocity was calculated by quantifying the standard deviation between the two. The standard deviations of the current velocities were 0.0016 m/s, 0.0027 m/s and 0.0014 m/s, and the maximum errors of the estimated current velocities were 0.0057 m/s, 0.0069 m/s and 0.0031 m/s in the x_i, y_i and z_i axes in the body frame reference. According to [70], an AUV-fixed acoustic doppler current profiler (ADCP) usually obtains a velocity measurement with an uncertainty margin of ± 0.1 m/s. Here the standard deviations of the current velocity estimates lay within this uncertainty margin of ADCP measurement.

In order to study the effectiveness of the HGO, estimation errors from the HGO using the LMI and the state observer with the gain matrix using the pole placement (PP) method were compared. While the gain for the HGO is optimised by using LMI, the counterpart for the state observer is obtained using the PP. The pole location was selected in such a way to fix only the undesirable aspects of the open-loop response and avoids either large increases in bandwidth [71]. The gain for the HGO and the state observer are shown in Equation 4.20 and 4.21 respectively.

$$G_{HGO} = \begin{bmatrix} 15.5054 & 0 & 3.9756 \\ 0 & 19.4735 & 0 \\ 3.5061 & 0 & 17.1021 \\ 0 & 5.5409 & 0 \\ 13.2489 & 0 & 16.8845 \\ 0 & 26.1511 & 0 \\ 11.9951 & 0 & 19.7814 \\ 0 & 35.9769 & 0 \\ 17.9880 & 0 & 23.4438 \end{bmatrix} \tag{4.20}$$

$$G_{SO} = \begin{bmatrix} 2.5199 & 0.515 & 3.8491 \\ 1.4834 & 1.7287 & 1.3190 \\ 2.3363 & 0.0618 & 4.0765 \\ 0.0500 & 1.1679 & 0.0444 \\ 85369 & 0.2481 & 24.7374 \\ 4.7676 & 12.1646 & 4.2406 \\ 10.7580 & 0.1796 & 24.4995 \\ 4.1958 & 20.9760 & 3.7374 \\ 6.1138 & 0.2169 & 29.4517 \end{bmatrix} \tag{4.21}$$

As shown in Figure 4.9, the HGO can estimate current velocity with a lower initial peak transient phenomenon than the pole placement method. As mentioned previously, the selection of the poles is a compromise between the rapidity of the response of the error vector and the sensitivity to disturbances and measurement noise. For higher-order systems, the location of the poles and the system dynamics (response characteristics) are not easily correlated [64]. This might result in the higher peak in the estimation errors by the state observer using the PP method.

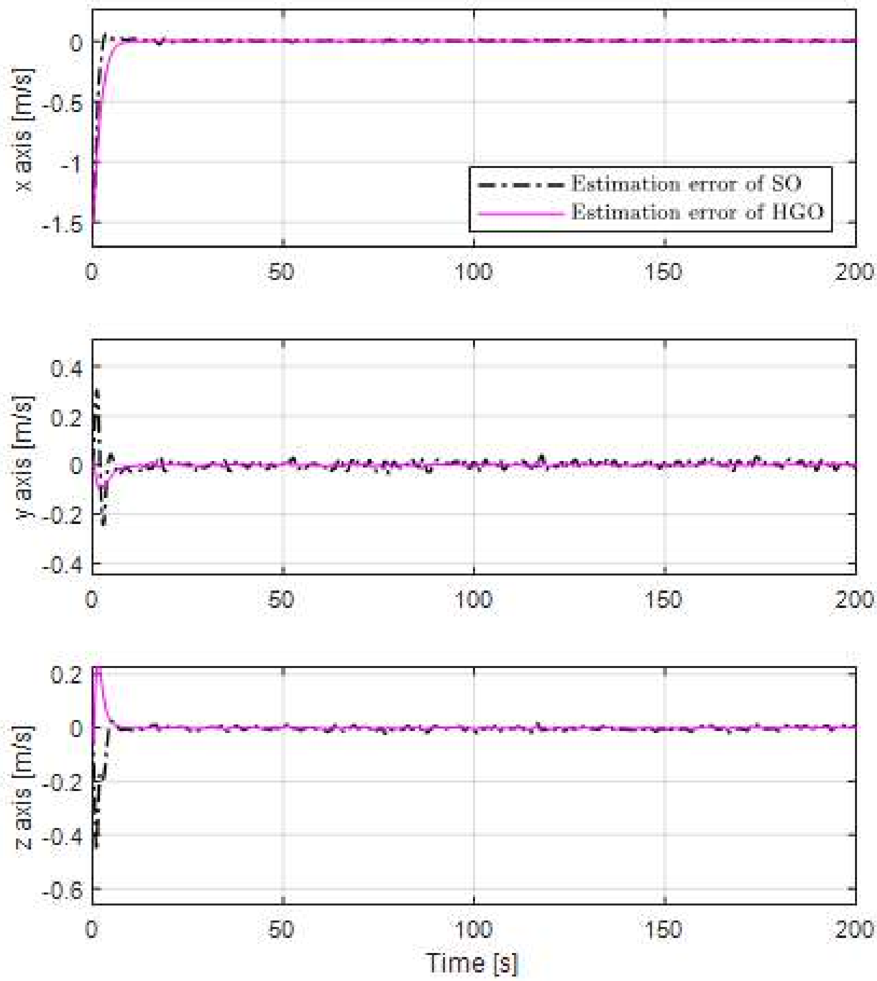

Figure 4.9: Comparison of estimation errors between the state observer and HGO

Furthermore, data analysis of the path following errors were carried out to analyse the path following performance more accurately and quantitatively. Three parameters were calculated to evaluate the path following accuracy and stability, viz, the average value of the absolute path errors, standard deviation of the path errors, and maximum value of the absolute path errors as shown in Figure 4.10. The standard deviation directly reflects the path following stability while the average reflects the tracking accuracy [63]. As shown in Figure 4.10, the HGO exhibits better path following accuracy and stability with smaller average and standard deviation of path error than the state observer using PP.

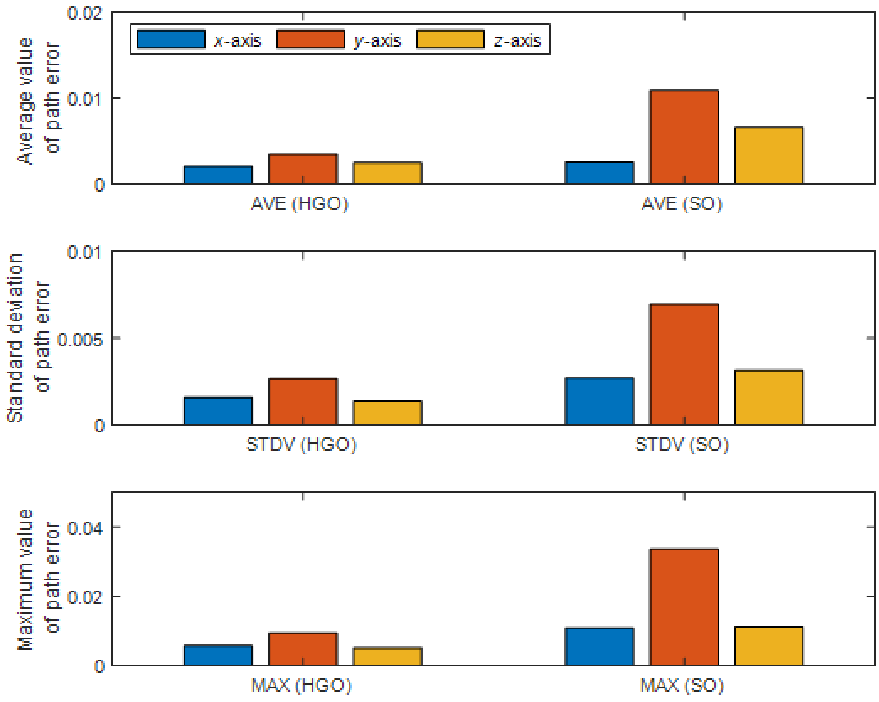

Figure 4.10: Data analysis of path errors for HGOs using LMI and the state observer (SO) using PP.

4.5.2 Case 2: Helix Path

In the second simulation case, a helix path was specified as follows:

$$P_2 := \begin{cases} x_f(s) = R\cos(\frac{s}{\sqrt{R^2+(h/2\pi)}}) \\ y_f(s) = R\sin(\frac{s}{\sqrt{R^2+(h/2\pi)}}) \\ z_f(s) = \frac{h}{2\pi}\frac{s}{\sqrt{R^2+(h/2\pi)}} \\ \theta_f(s) = -\arctan(\frac{h}{2\pi R}) \\ \psi_f(s) = \frac{s\cos(\theta_f(s))}{R} + \frac{\pi}{2} \\ \alpha_f(s) = \frac{R}{R^2+(\frac{h}{2\pi})^2} \\ \beta_f(s) = \frac{\frac{h}{2\pi}}{R^2+(\frac{h}{2\pi})^2} \end{cases} \tag{4.22}$$

where R is the radius of the helix and h is the vertical separation distance of helix, and they were set as $R = 400$ m and $h = 40$ m. The resulting motion of the AUV for a 1200 seconds simulation is shown in Figure 4.11.

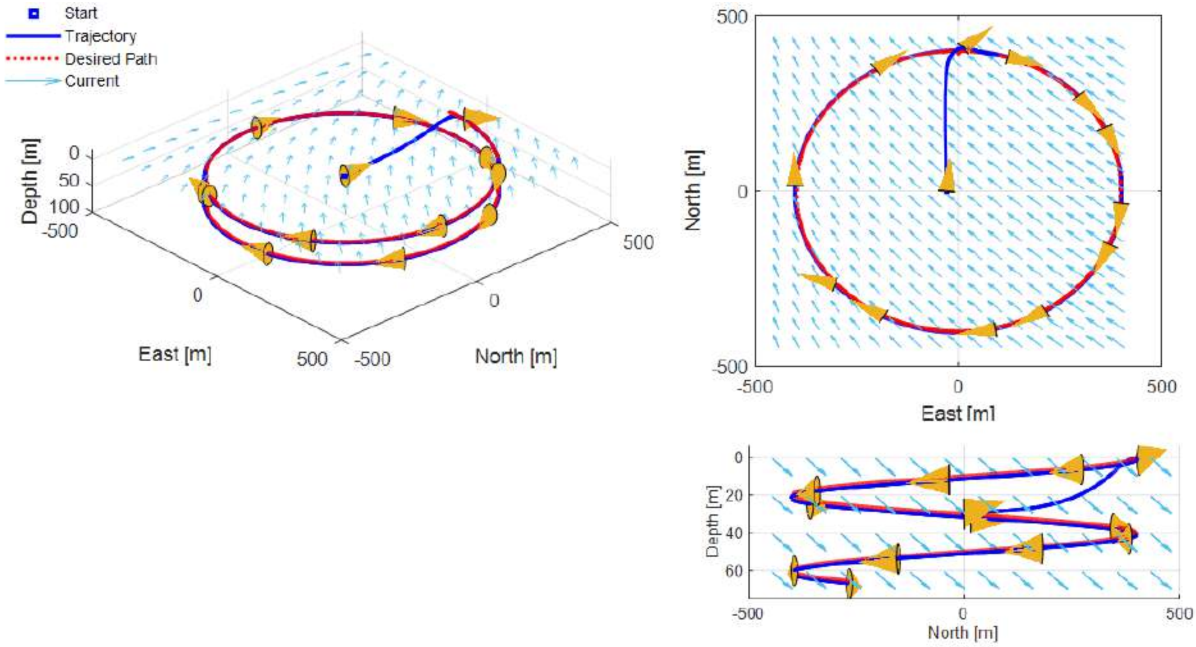

Figure 4.11: Path following of the desired helix path in NED, in xy-plane and in xz-plane

The trajectory of the AUV is the blue line while the red dashed line is the reference. The yellow cone shapes represent the location and orientation of the AUV at each 50 seconds interval. The AUV started from on the initial point at [0, -30, 30], then followed the desired helix path as shown in Figure 4.11. The initial point of the desired path was located at [400, 0, 0], and it took around 100 seconds for the AUV to reach this point to begin to follow the desired path. It can be easily seen from Figure 4.12 that the AUV trajectory converged to the desired path.

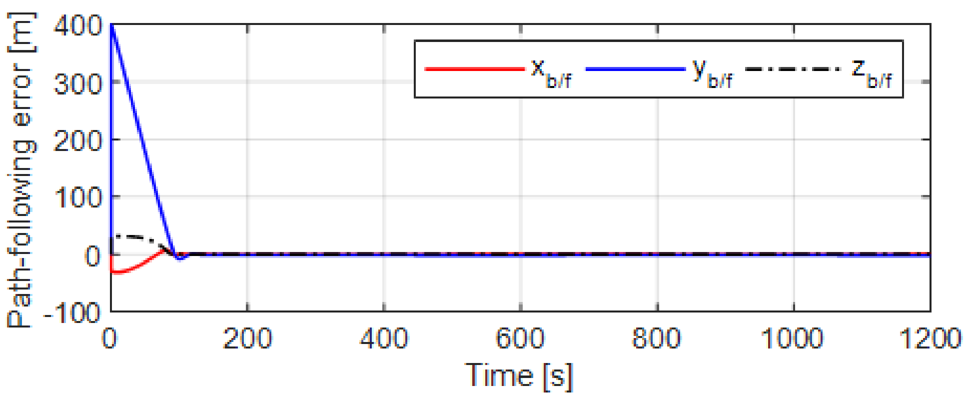

Figure 4.12: Time evolution of the path-following errors

The vehicle's absolute velocities over the ground were measured, and vehicle's relative velocities were estimated by the HGO in the x_b, y_b and z_b axes direction as shown in Figure 4.13. The estimated current velocities and the actual current velocities are illustrated in Figure

4.14. The current velocity in the y-axis especially oscillated as the current was assumed to be nonuniform with different velocities at different points. The standard deviations of the current velocities were 0.0077 m/s, 0.0078 m/s and 0.0134 m/s, and the maximum errors of the estimated current velocities were 0.0411 m/s, 0.0413 m/s and 0.0572 m/s in the x_i, y_i and z_i axes in the body frame reference.

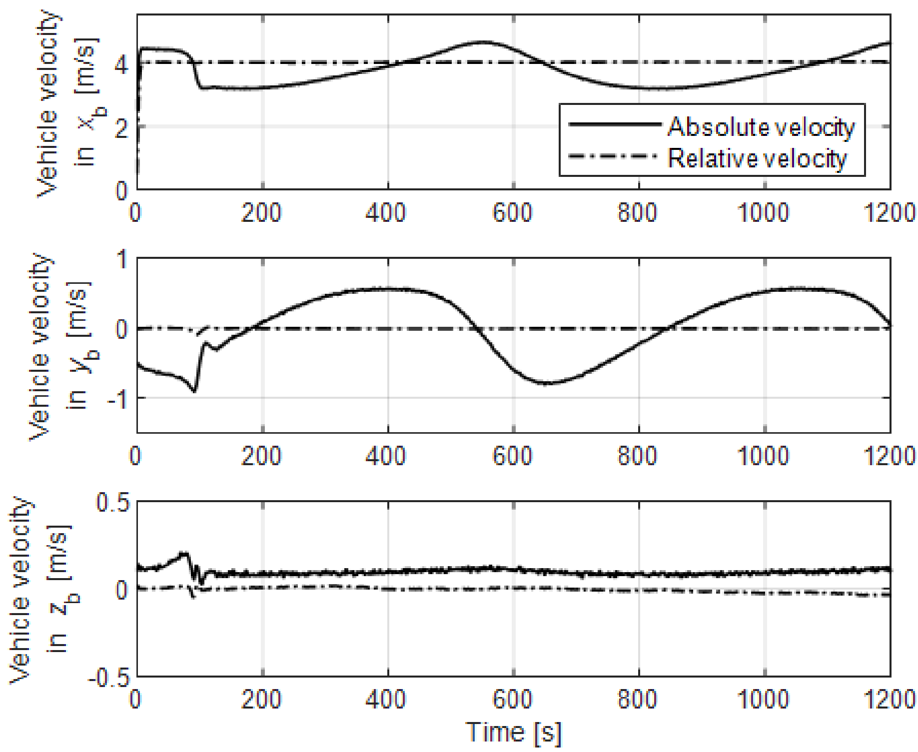

Figure 4.13: Vehicle's absolute and relative velocities in x_b, y_b, and z_b axes in the body frame reference

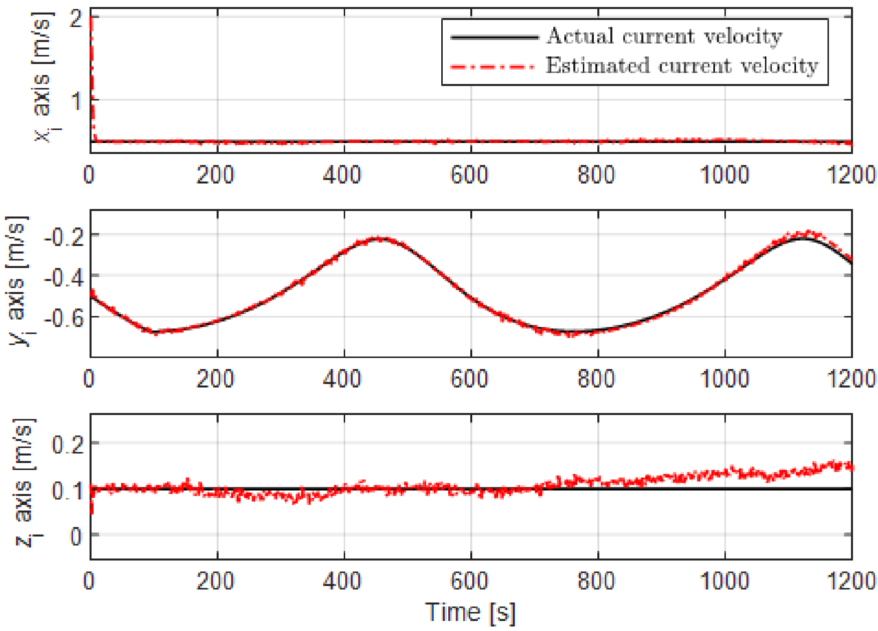

Figure 4.14: Comparison between actual and estimated current velocities in x_i, y_i and z_i axes for the helix path

Current velocity estimates from both the HGO using the LMI and the state observer using the pole placement were compared as shown in Figure 4.15. Estimated current velocity in the y_i and z_i axis clearly shows that the HGO can estimate current velocity with a higher accuracy than for the pole placement method. The current estimation error of the state observer oscillates unlikely the HGO. Thus, it can be concluded that the observer gain plays a major role in eliminating the path following errors caused by ocean currents.

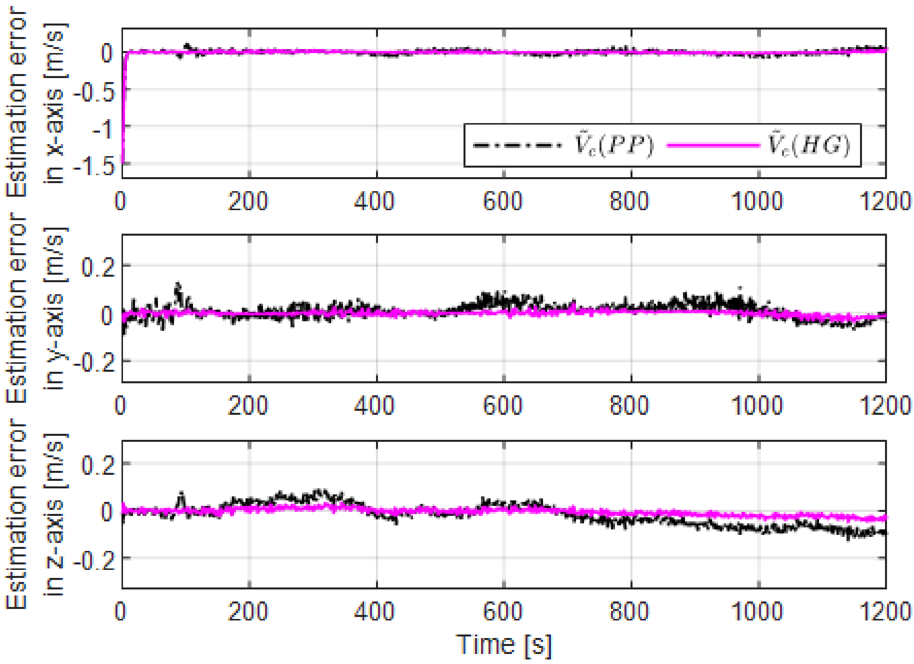

Figure 4.15: Comparison of current estimation errors between the HGO and the state observer (SO)

As shown in Figure 4.16 the HGO exhibits better path following accuracy and stability with smaller average and standard deviation of path error than the state observer.

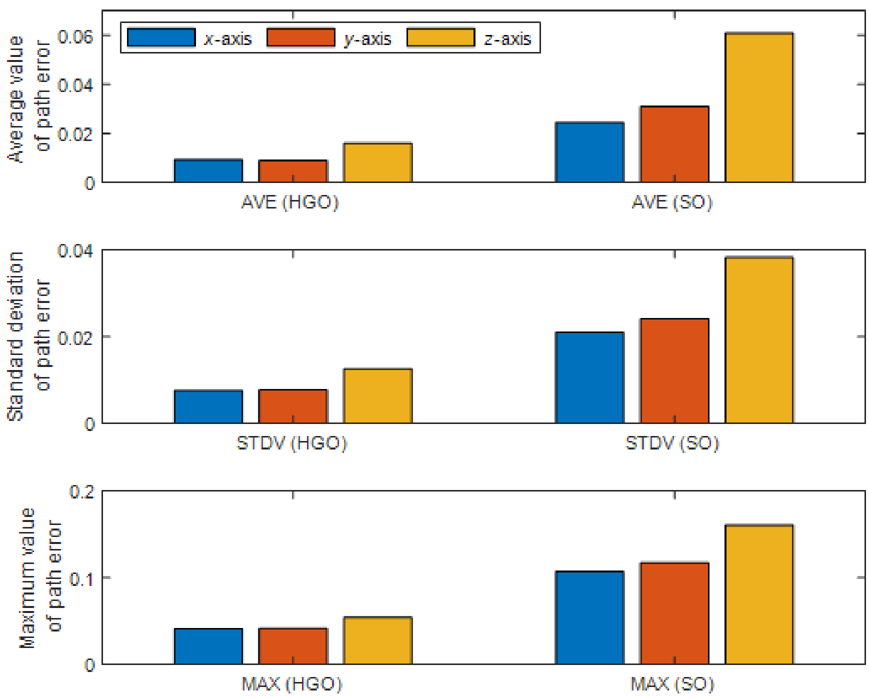

Figure 4.16: Data analysis of path errors for HGO and the state observer (SO)

In Table 3, means of estimation error from the current estimation results for the HGO and the state observer using pole placement are tabulated. The means of estimation error the HGO are smaller than the state observer with the pole placement method for all axes, which contribute an estimation accuracy improvement of 62%, 71% and 72% in x_i, y_i and z_i axes respectively.

Table 4.4: Mean of estimation error for HGO and state observer (SO) using pole placement

Mean of estimates error	x_i axis	y_i axis	$x_i$axis
HGO	0.0094	0.0090	0.0170
SO PP	0.0245	0.0310	0.0608

The actual pitch and yaw angles are compared with the desired pitch and yaw reference angles obtained by the guidance law in Figure 4.17. The desired pitch and yaw reference angles were obtained from the guidance law shown in Equation 4.14, and the actual yaw angle was well matched with the desired yaw angle. However, the pitch angle had minor discrepancy between the desired and the actual angle, which resulted in an increasing current estimation error in the z_i axis as shown in Figure 4.17.

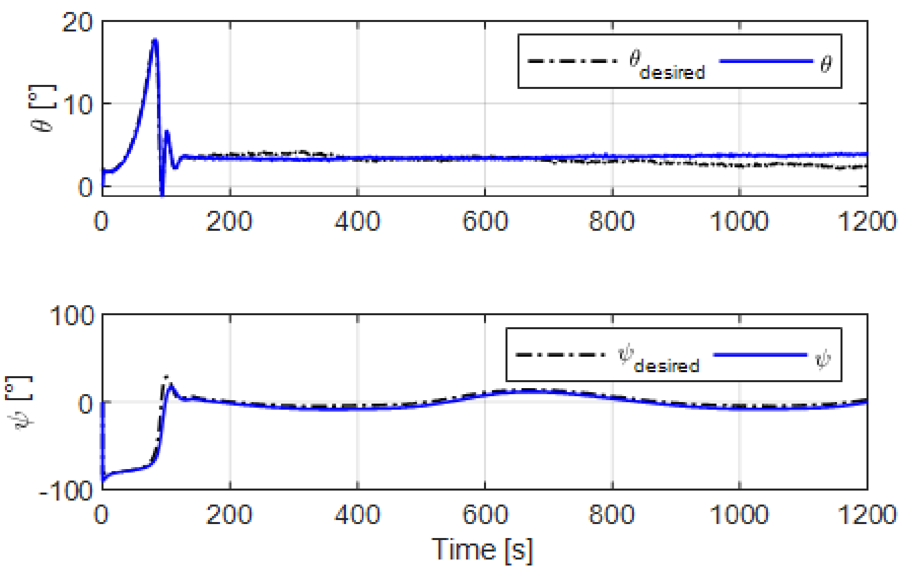

Figure 4.17: Desired and actual rates for pitch and yaw for case 2

The elevator angle is shown by the dotted line while the rudder angles are shown by the solid line in Figure 4.18. The maximum angles of elevator and rudder depend on the model of the control plane and its properties, for example, the maximum angle of the control plane is 20° for the MUN Explorer AUV [72], and 13.6 ° for a REMUS AUV [38]. Assuming the maximum rudder angle is 15° in this study, the simulation result shows that the angles for elevator and rudder were operated within the upper and lower angle constraints.

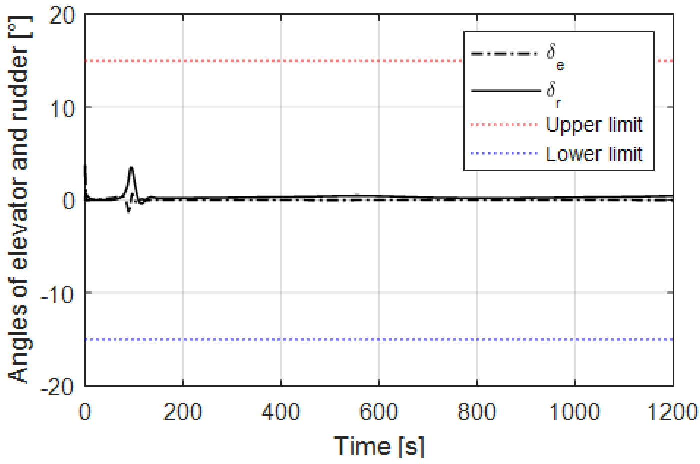

Figure 4.18: Angles of elevator and rudder

In order to calculate the desired pitch and yaw angles, it is necessary to solve Equations 4.8 and 4.9 for f and g, and the two solutions depend on the condition of the current velocities expressed in the f-frame. The solution for Equations 4.8 is chosen as f_1 for the whole running time since the current velocity in the z-axis is positive through the whole simulation as shown in the first plot of Figure 4.19. On the other hand, the solution for Equations 4.9 is chosen based on the current velocity in the y-axis. For instance, the current velocity in the y-axis in the time span between 537 to 897 seconds is negative, so the solution g_2 was chosen. The chosen solutions, f and g are shown in the second plot of Figure 4.19.

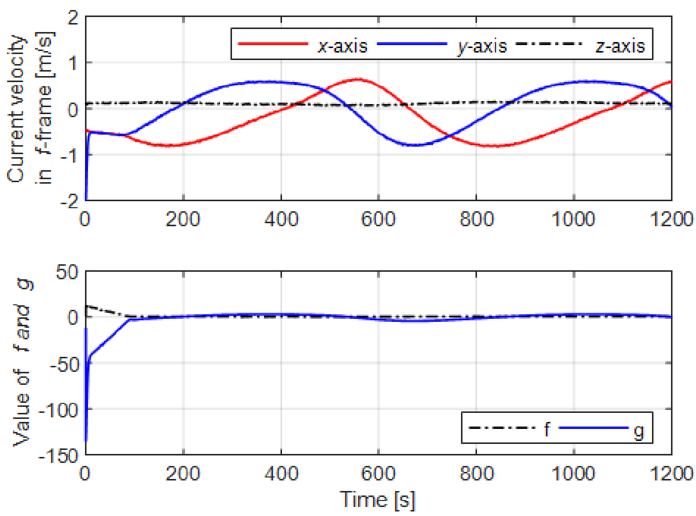

Figure 4.19: Ocean current velocities expressed in the f-frame (top) and solution values of f and g (bottom)

The Serret-Frenet frame propagates along the desired path at the instantaneous speed, which is shown in the left plot in Figure 4.20. The distance travelled along the path, s is shown in right plot in Figure 4.20. Once s is obtained, it is used to define the desired path recursively as illustrated in Equations 4.12 and 4.13.

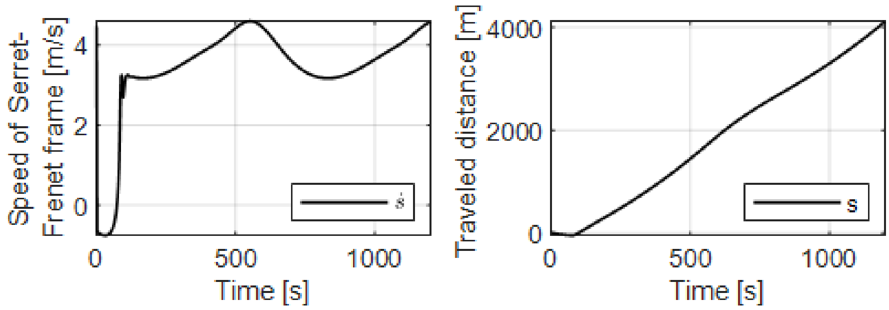

Figure 4.20: Speed of Serret-Frenet frame along path (left) and traveled distance (right)

4.6 Conclusion

In this chapter, a path following control method for an AUV using a high-gain observer based on a dynamic model has been investigated. The control objective of the path following was to make the vehicle follow a given desired path and maintain a desired constant relative surge velocity.

The high-gain observer was used to estimate the states of the vehicle which are not directly measured, and the observer gain was optimised by solving the LMI which represents the estimation error dynamics. The current velocities in three dimensions were obtained from the difference between the vehicle's absolute velocity measured by the DVL and the vehicle's relative velocity estimated by the HGO.

The update law and guidance law were utilised to provide pitch and yaw references to the controllers, so that the AUV could follow the desired path described by the Serret-Frenet frame.

Two path-following cases consisting of a straight-line and a helix path were simulated to validate the performance of the proposed control system. Both cases have shown that the AUV reached and converged to the desired path within 50 and 100 seconds of the transient period respectively. Furthermore, the current velocity estimates in the x, y and z axes were obtained by the HGO, and the standard deviations of the current velocity estimates lay within the uncertainty margin of the ADCP which is ± 0.1 m/s for both simulation cases.

In order to study the effectiveness of the HGO using the LMI approach, estimation errors from both the HGO and the state observer using the pole placement (PP) were quantitatively analysed. The HGO exhibits more accurate and robust path following performance and stability with smaller average and standard deviation of path error than the state observer using the PP method.

The AUV's dynamic model is able to represent the forces and moments that are not captured by the kinematic motion model. Thus, the HGO based on the dynamic model has the potential to improve the performance of the path following problem and current estimation. However, in order to promote the practical application of the proposed path-following guidance and control system in a real ocean environment, the following future work is to be implemented: (1) a system identification approach will be implemented for the unknown hydrodynamic model of the AUV; (2) by employing a time-varying equation for the lookahead distance, a more flexible path following performance can be achieved; and (3) the real ocean environment is more harsh and complex than considered in the simulations here, and this may result in more serious parameter perturbations, model uncertainties, and external disturbances. Therefore, the adaptability of the proposed path following system needs further verification in the real ocean environment.

Chapter 5

Ocean Current Estimation and Design of Path Following Guidance Logic: Simulation and Field Testing

In previous chapter, the path following control method using the high-gain observer (HGO) based on a dynamic model has been investigated by using the simulation for the Dolphin II AUV. In order to study the effectiveness of the HGO using the linear matrix inequality (LMI) approach, the HGO and the state observer using the pole placement were quantitatively analysed, which showed the HGO exhibited more accurate and robust path following performance and stability. However, the path following guidance law presented in chapter 4 was neither quantitatively analysed by comparing different method nor tested in the open water.

Thus in an effort to enhance the performance of the AUV's path-following guidance system, a 'Pure Proportional Navigation and Pursuit Guidance (PPNAPG)' approach is developed in this chapter. In order to validate the proposed guidance system, it would be ideal to integrate the proposed guidance system within the control architecture of the vehicle and carry out the experimental field testing. However, the given time as a visiting fellow in *Memorial University of Newfoundland* in Canada was not sufficient to develop the back-seat driver for integrating the guidance system before the weather window closed due to the climate of Newfoundland characterised by freezing and snow winter. For that reason, the performance of the proposed guidance system is replicated by a simulator of the *MUN Explorer* while the performance of a conventional line-of-sight (LOS) which is the existing guidance system for the *MUN Explorer* was obtained from the field testing. In this chapter, the performance of the proposed PPNAPG guidance system was quantitatively validated by analysing the times taken to reach each waypoint and the cross-track error.

Firstly, a simulator for the *MUN Explorer* was built by using the *component build-up* method.

Secondly, the combined the pure proportional navigation guidance (PPNG) law and the pursuit guidance (PG) law (referred to as the 'PPNAPG (Pure Proportional Navigation and Pursuit Guidance)') was proposed as the path following guidance law. Lastly, the extended Kalman filter (EKF) was chosen as a non-linear estimator to estimate the current velocity by utilising the measurement from GPS, rpm and heading angles. As the Acoustic Doppler current profiler (ADCP) was deployed to collect the magnitude and direction of the current, the performance of the EFK to estimate current velocity could be validated by quantitatively analysing the estimation error.

A series of experiments at sea was conducted to measure the vehicle's response at Holyrood Marine Base, St. John's, Canada in November, 2019. These experiments were conducted with assistance of the Autonomous Ocean Systems Centre (AOSCENT) staff at *Memorial University of Newfoundland* and funding for travel to Canada from the *Ocean Frontier Institute*.

Figure 5.1: The *MUN Explorer* AUV at Holyrood, Newfoundland, Canada.

5.1 Introduction

The *MUN Explorer* is a survey-class AUV acquired by Memorial University, St John's, Newfoundland and Labrador, Canada in 2006. The *MUN Explorer* was built by International Submarine Engineering Ltd., (ISE) in Port Coquitlam, British Columbia. The *MUN Explorer* is a multi-user AUV primarily for research purposes in Newfoundland and other parts of Canada. The *MUN Explorer* has been serving as a research platform for underwater sensor technologies such as underwater imaging, water quality sampling, offshore environmental monitoring, seabed imaging and iceberg reconnaissance [73]. The accessibility of the *MUN Explorer* at Memorial University facilitated the performing of a series of path-following missions required for this thesis work, during September, 2019. The entire test was carried out at Holyrood bay area situated 45 km south west of St. John's, Newfoundland. A satellite map of the location of Holyrood and its marine chart are shown Figure 5.2.

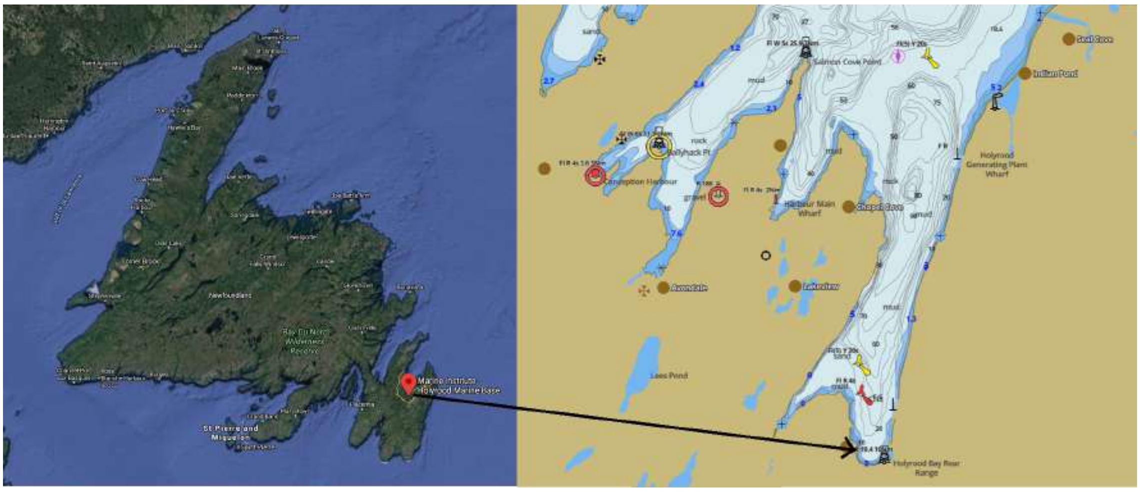

Figure 5.2: The location of the Holyrood Marine Base, Marine Institute [Left] and the marine chart of Holyrood Bay [74].

In this chapter, a numerical model for the *MUN Explorer AUV* in six degrees of freedom is described. The external forces and moments resulting from hydrostatics, hydrodynamic lift and drag, added mass, and the control inputs of the vehicle propeller and planes were taken into consideration to define the external forces and moments.

Simulation of underwater vehicles in the time domain has been utilised as a tool to predict motions of the vehicles before prototype tests. Important factors to be studied were operating limits, the establishment of valid control strategies, and the feasibility to perform prescribed manoeuvres as effectively as possible. The design of controllers, training of AUV operators and even mission planning all rely on realistic simulation of the AUVs.

In order to characterise the behaviour of a vehicle, a dynamic model based on theory and

empirical data is often built, which can be used as an efficient platform for development of the vehicle control system [75]. A reliable model can predict the actual vehicle response. A dynamic model of an axisymmetric streamlined AUV based on the"body-build-up" method was developed by Perrault [76] and Evans [77] using MATLAB and Simulink for use for the MUN Explorer AUV. In order to validate this model, it was necessary to have experimental data from real vehicles.
Issac's Ph.D thesis [75] is aimed at evaluating the performance of a hydrodynamic motion simulation model developed based on the component build-up method for torpedo-shaped underwater vehicles. The model is derived in a form that only requires the specification of the vehicle's geometry, and the lift, drag and moment characteristics of its constituent elements: the hull, control surfaces, propulsion system etc. The total hydrodynamic load acting on the vehicle is obtained by summing up the loads from each of these components.

5.2 Materials and Procedures

5.2.1 The *MUN Explorer* AUV structure

The *MUN Explorer* is a streamlined survey-class AUV for underwater survey and offshore environmental monitoring purposes. The AUV is 4.5 m in length with maximum mid-body diameter of 0.69 m. It is propelled by a twin-blade propeller and can reach cruising speeds between 0.5 to 2.5 m/s. Manoeuvring of the vehicle in 3-D space is facilitated by six control-planes: two dive planes on the forward payload section and four aft planes arranged in an 'X' configuration as shown in Figure 5.3.

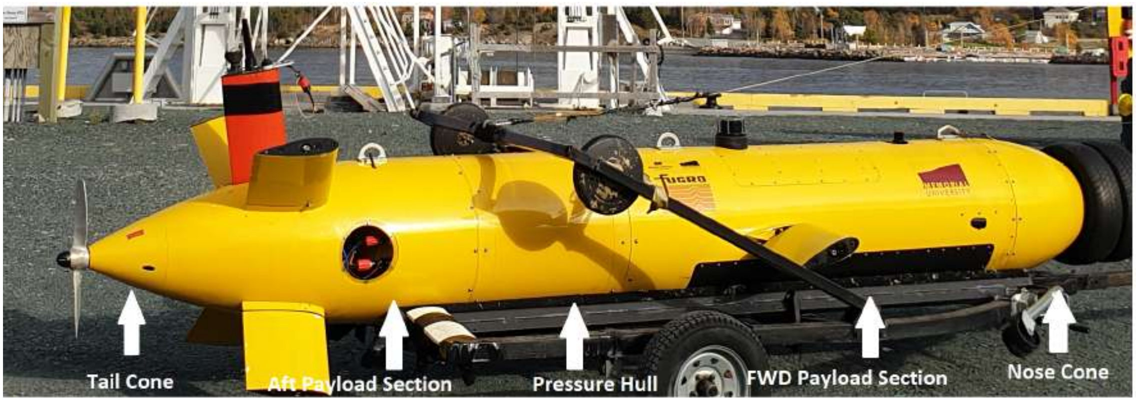

Figure 5.3: The *MUN Explorer* AUV at Holyrood, Newfoundland, Canada.

The *MUN Explorer* AUV is modular in structure with cylindrical main body, a front nose cone and a tapered tail section at rear. Most of the hull sections, except for the pressure hull, are made from Glass Reinforced Plastic (GRP) which reduces the overall weight of the vehicle. The pressure hull is a cylindrical ring stiffened module made of 7075-T6 Aluminium, consisting of a cylindrical section and 2 hemispherical end caps [75]; it is rated to 3000m depth.

The forward payload section has the dive planes, depth sensor and LinkQuest^{TM} acoustic transponder mounted. There is space available inside of this section for additional wet payload items.

The aft payload section is free-flooding and at the rear of the pressure hull. It has a tapered end to connect to the tail cone section. Navigation sensors such as the Doppler Velocity Log (DVL) and the fixed communication mast are located in this section. The aft control planes are attached to the exterior of this section in an 'X' configuration.

The tail cone has a torpedo shape which aims to minimise the drag derived by the pressure drop at the end of the vehicle body. In the tail cone section, the propeller and the drive motor are located.

5.2.2 Control and Guidance

The Vehicle Control Computer (VCC) is the "brain" of the AUV that provides guidance and control using sensors and actuators. For the *MUN Explorer*, it is a rack mounted Inova Compact PCI computer, which acquires data from all onboard instruments and transfers this data to the Surface Control Console (SCC). The SCC receives telemetry from the vehicle and transmits commands to the vehicle. The SCC is a Lenovo P72 Laptop running the Debian 9 operating system, and the SCC for the *MUN Explorer* is shown in Figure 5.4. The SCC GUI displays the current state of most vehicle feedback information and accepts commands for actuators and instruments. It is used for piloting the vehicle when it is at the surface and in radio contact.

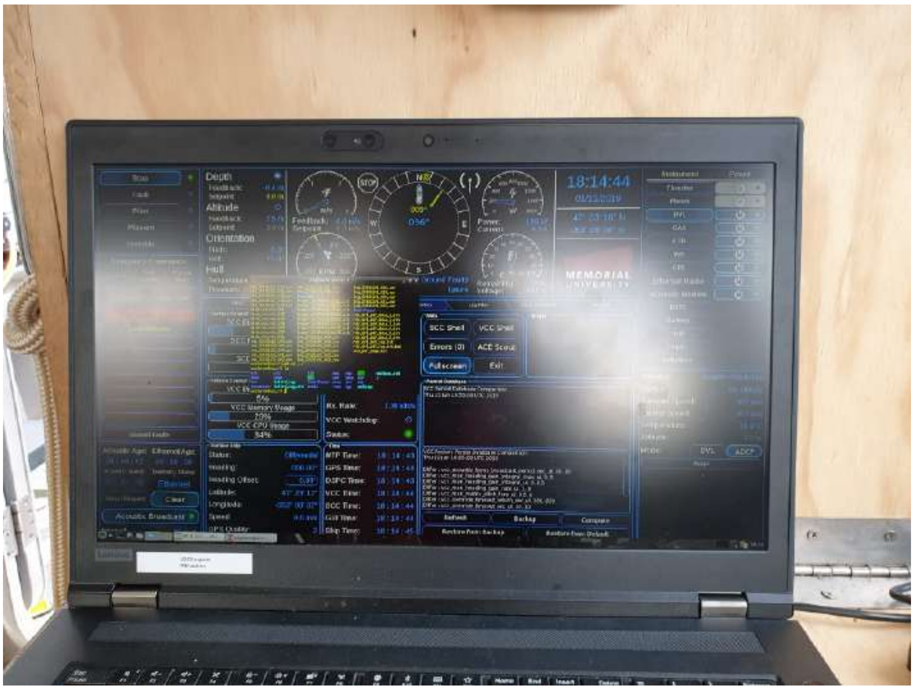

Figure 5.4: The Surface Control Console (SCC) of the *MUN Explorer* AUV

5.2.3 Navigation and Positioning

In order to locate and orient the vehicle in 3-D space, several different sensors are used. A pressure sensor located in the forward payload section measures the depth of the vehicle below the water surface, while bottom avoidance and altitude are obtained by using a forward/downward looking altimeter located in the nose cone.
The Doppler Velocity Log (DVL) is an Acoustic Doppler Current Profiler (ADCP), which measures velocity using four acoustic beams. This DVL provides the VCC with data such as bottom velocity, water velocity, altitude, pitch and roll to estimate the position of the vehicle. For the *MUN Explorer* AUV, a RDI Velocity Sensor (RDI 300 KHz DVL) is used to determine 3-dimensional vehicle velocity relative to both water and or ground. The VCC can estimate the position of the vehicle by utilising the velocity from the ADCP and the heading data. When the vehicle is at the surface, the position fixes from a GPS can be used to initialise or reset the position [78].

Furthermore, the vehicle uses an Attitude Heading and Reference System to sense the vehicle attitudes (roll, pitch and yaw) and angular rates (roll rate, pitch rate and yaw rate).

5.3 Motion Simulator for the *MUN Explorer* AUV

One of the important factors of the AUV's dynamic model is to predict the trajectory of the vehicle underwater: the position and orientation of the vehicle with respect to time. To conveniently describe the AUV model, two suitable reference frames body-fixed and Earth-fixed reference frames, are used which described in Appendix A.1. The position and orientation of the vehicle should be described relative to the inertial reference frame while the linear and angular velocities of the vehicle should be expressed in the body-fixed coordinate system [79]. Appendix A contains the the figure of the AUV's body-fixed and Earth-fixed reference frame and notation table.

5.3.1 Kinematics

Based on the notation in Table A.1, the general motion of the vehicle in 6 DOF can be described by the following vectors:

$$\begin{aligned}
\boldsymbol{\eta} &= [\boldsymbol{\eta}_1^T, \boldsymbol{\eta}_2^T]^T; \qquad \boldsymbol{\eta}_1 = [x, y, z]^T; \quad \boldsymbol{\eta}_2 = [\phi, \theta, \psi]^T \\
\boldsymbol{\nu} &= [\boldsymbol{\nu}_1^T, \boldsymbol{\nu}_2^T]^T; \qquad \boldsymbol{\nu}_1 = [u, v, w]^T; \quad \boldsymbol{\nu}_2 = [p, q, r]^T \\
\boldsymbol{\tau} &= [\boldsymbol{\tau}_1^T, \boldsymbol{\tau}_2^T]^T; \qquad \boldsymbol{\tau}_1 = [X, Y, Z]^T; \quad \boldsymbol{\tau}_2 = [K, M, N]^T
\end{aligned}$$

The transformation matrices which related through the functions of the Euler angles are described in Appendix A.1. Based on the transformation matrix $\boldsymbol{J}_1(\boldsymbol{\eta}_2)$ and $\boldsymbol{J}_2(\boldsymbol{\eta}_2)$ in Equation A.2 and A.3, the kinematic equations can be expressed in vector form as :

$$\begin{bmatrix} \dot{\boldsymbol{\eta}}_1 \\ \dot{\boldsymbol{\eta}}_2 \end{bmatrix} = \begin{bmatrix} \boldsymbol{J}_1(\boldsymbol{\eta}_2) & \mathbf{0}_{3\times3} \\ \mathbf{0}_{3\times3} & \boldsymbol{J}_2(\boldsymbol{\eta}_2) \end{bmatrix} \begin{bmatrix} \boldsymbol{\nu}_1 \\ \boldsymbol{\nu}_2 \end{bmatrix} \quad \Longleftrightarrow \quad \dot{\boldsymbol{\eta}} = \boldsymbol{J}(\boldsymbol{\eta})\boldsymbol{\nu} \tag{5.1}$$

5.3.2 Rigid Body Dynamics

The equations of motion for a rigid body in six degrees of freedom are represented as follows:

$$\begin{aligned}
m[\dot{u} - vr + wq - x_G(q^2 + r^2) + y_G(pq - \dot{r}) + z_G(pr + \dot{q})] &= \Sigma X_{ext} \\
m[\dot{v} - wp + ur - y_G(r^2 + p^2) + z_G(qr - \dot{p}) + x_G(qp + \dot{r})] &= \Sigma Y_{ext} \\
m[\dot{w} - uq + vq - z_G(p^2 + q^2) + x_G(rp - \dot{q}) + y_G(rq + \dot{p})] &= \Sigma Z_{ext} \\
I_x\dot{p} + (I_z - I_y)qr - (\dot{r} + pq)I_{xz} + (r^2 - q^2)I_{yz} + (pr - \dot{q})I_{xy} & \\
+m[y_G(\dot{w} - uq + vp) - z_G(\dot{v} - wp + ur)] &= \Sigma K_{ext} \\
I_y\dot{q} + (I_x - I_z)rp - (\dot{p} + qr)I_{xy} + (p^2 - r^2)I_{zx} + (qp - \dot{r})I_{yz} & \\
+m[z_G(\dot{u} - vr + wq) - x_G(\dot{w} - uq + vp)] &= \Sigma M_{ext} \\
I_z\dot{r} + (I_y - I_x)pq - (\dot{q} + rp)I_{yz} + (q^2 - p^2)I_{xy} + (rq - \dot{p})I_{zx} & \\
+m[x_G(\dot{v} - wp + ur) - y_G(\dot{u} - vr + wq)] &= \Sigma N_{ext}
\end{aligned} \tag{5.2}$$

where m is the vehicle mass. The first three equations in Equation 5.2 represent the translational motion while the last three equations represent the rotational motion. In Table A.2 in Appendix A.2, the coordinate of the vehicle's centres of gravity and buoyancy, vehicle mass and moment of inertia are also defined. The value of m and the *MUN Explorer* AUV's moments of inertia are tabulated in Table A.3.

5.3.3 Restoring Forces and Moments

In the hydrodynamical terminology, the gravitational and buoyancy forces are called restoring forces [79]. The gravitational force $\boldsymbol{f}_G$ acts through the centre of gravity $\boldsymbol{r}_G = [x_G, y_G, z_G]$ of the vehicle while the buoyancy force $\boldsymbol{f}_B$ acts through the centre of buoyancy $\boldsymbol{r}_B = [x_B, y_B, z_B]$. When the mass of the vehicle is m, the vehicle's weight and buoyancy are expressed as $W = mg$ and $B = \rho \nabla g$, where ρ is the density of the surrounding fluid and ∇ is the total displaced volume by the vehicle.

The weight of the *MUN Explorer* AUV can be different between missions depending on the payload sensors and the amount of ballast. The weight and buoyancy used in this study were referenced from [75] and are shown in Table A.4. Also equations for the restoring force and moment are described in Appendix A.3.

5.3.4 Hydrodynamic Damping

The hydrodynamic damping of an underwater vehicle in six degrees of freedom is complicated because it is coupled and highly non-linear. In order to simplify the model of the vehicle, the following assumptions were made:

- **Assumption 1** The linear and angular coupled terms were neglected. It was assumed that terms such as $\boldsymbol{Y}_{rv}$ or $\boldsymbol{M}_{rv}$ are relatively small.
- **Assumption 2** It was assumed that the vehicle is symmetrical in both the *xy-plane* and *xz-plane.*
- **Assumption 3** It was assumed that any damping terms greater than second-order were small which allowed the elimination of the higher-order terms.

1. Axial Drag

The main factors of hydrodynamic damping are skin friction caused by the boundary layers and damping due to vortex shedding. The vehicle's axial drag can be expressed by using the following empirical equation:

$$X = -\left(\frac{1}{2}\rho c_d A_f\right) u|u| \tag{5.3}$$

The Equation 5.4 yields the non-linear coefficient for the axial drag force:

$$X_{u|u|} = -\frac{1}{2}\rho c_d A_f \tag{5.4}$$

where ρ is the density of the fluid, A_f is the AUV's frontal area, and c_d is the axial drag coefficient of the vehicle. The parameters of the *MUN Explorer* AUV including the diameter and frontal area, A_f are tabulated in Table A.5 in Appendix A.4.

2. Cross-flow Drag

The cross-flow drag could be obtained by summing the hull cross-flow drag and the control surface cross-flow drag. The hull drag was calculated by strip theory which means that the total hull drag was estimated as the sum of the drags on the two-dimensional cylindrical vehicle cross-sections. In this study the cross-flow drag force was calculated by using the three directions of translational motions, x, y and z, the drag coefficients and the area of interest. The nonlinear cross-flow drag coefficients were calculated by the equations shown in Appendix A.4. The *MUN* Explorer's geometric parameters can be found in Table A.7 in Appendix A.4 as well.

5.3.5 Added Mass

Added mass is the inertia added to a system since an accelerating or decelerating body must move certain volume of surrounding fluid as it moves through it [80]. A detailed study on the sensitivity of added mass to changes in vehicle geometry can be found in [76]. The added mass terms for the *MUN Explorer* AUV were numerically approximated by using a program called ESAM (Estimation of Submarine Added Mass), developed by the Defence Research Establishment Atlantic (DREA) [81]. The ESAM program can calculate all the added mass terms of a submerged multi-component rigid body analytically. For the *MUN Explorer*, added mass was calculated by approximating the body as a finned prolated spheroid whose components were replaced by equivalent ellipsoids of the same fineness ratio and displaced volumes [75]. Added mass matrix for the *MUN Explorer* AUV with its 'X' tail configuration was expressed in Appendix A.5.

5.3.6 Control Planes and Propulsion

The *MUN Explorer* has six planes for manoeuvring as illustrated in Figure A.3. According to the numbering in the manufacturer's manual, the two bow planes are numbered 1 and 2 while the stern planes are 3 and 4 on the port side and 5 and 6 on the starboard side. The two forward planes control the depth. The x-configuration rudders, which are staggered at

45 degrees from the '+' configuration, will couple roll, pitch and yaw control into all four planes. The aft 'x' plane's configuration has been found to be best for the *MUN Explorer* AUV as it provides optimal stability, redundancy and limited protrusion [82]. The planes have a symmetrical cross-section of NACA 0024 [83] which is illustrated in detail in Appendix A.6. The empirical formula for the lift from the control planes are described and the related coordinates of the plane post are described in Appendix A.7.

The *MUN Explorer* AUV is propelled by a high-efficiency two-blade propeller with diameter 0.65m which enables the vehicle to reach a maximum speed of 2.5 m/s. A first-order approximation of the developed thrust T and torque Q for a propeller can be derived from lift force calculations and the related equations and coefficient can be found in Appendix A.8.

5.3.7 Total Vehicle Forces and Moments

The sum of external force and moment as shown in the right-hand side of Equation 5.2 can be obtained by combining the following force and moment equations for the vehicle:

- *Hydrostatics* : Equation A.9
- *Hydrodynamic Damping* : Equation 5.3 and A.10
- *Added Mass* : EquationA.11 and A.12
- *Control Planes* : Equation A.17 and A.25
- *Propeller Thrust and Torque* : Equation A.26

5.4 Field Experiment

In order to verify the performance of the vehicle numerical model, a series of experiments at sea were conducted to measure the vehicle's response. These experiments were conducted with assistance of the Autonomous Ocean Systems Centre (AOSCENT) staff at Memorial University of Newfoundland. Funding for the trials was received from Memorial University and from Fisheries and Oceans Canada through the Multi-partner Oil Spill Research Initiative (MPRI) 1.03: Oil Spill Reconnaissance and Delineation through Robotic Autonomous Underwater Vehicle Technology in Open and Iced Waters. Funding for travel to Canada came from the Ocean Frontier Institute. Also the Holyrood Marine Base of the Marine Institute of Memorial University of Newfoundland, referred to as the Marine Institute (MI) and located in the Holyrood Bay assisted with launching, operating and deploying the *MUN Explorer* during the experiment.

5.4.1 Experimental Setup

The manoeuvring trials using the *MUN Explorer* AUV were conducted on 31st October and 1st November 2019 in Holyrood Bay situated approximated 45 km south-west of St. John's Newfoundland, Canada.

1. Mission Planning and Control Computers

Mission specifics vary depending on the mission scenario and requirements. Mission planning was done using a software called *Mimosa*, which is a software used to create, edit, and generate mission plans as well as display mission plans and AUV location tracking as shown in Figure 5.5. *Mimosa* was originally developed by IFREMER in La Seyne-sur-mer, Provence, France, for ISE.

Figure 5.5: Mission Planning software *Mimosa*

D. Cartwright as shown in Figure 5.6 was used as the surface boat from which the Surface Control Computer (SCC) was operated to communicate with the Vehicle Control Computer (VCC). The SCC displays the data from the VCC using a GUI application; it also provides an interface to pilot the AUV at the surface and download mission files to operate the vehicle autonomously under water.

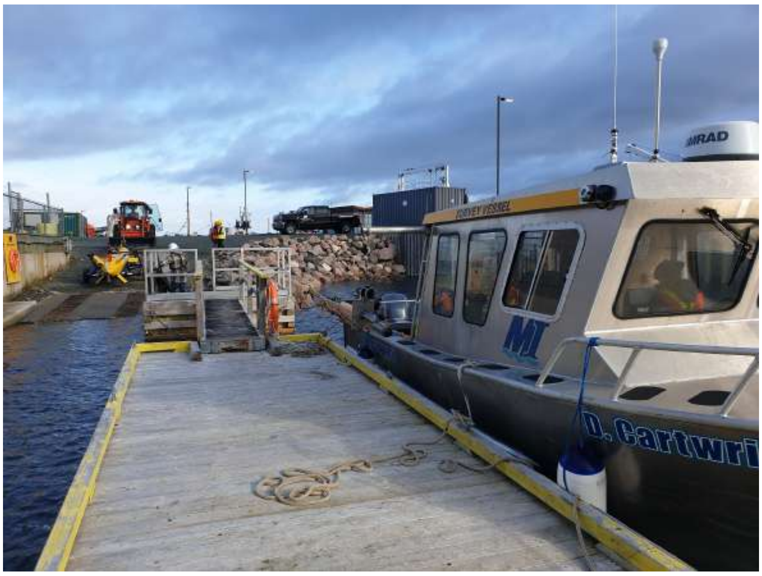

Figure 5.6: *D. Cartwright* of the *Marine Institute* as a control centre

The SCC and VCC can communicate via Ethernet radio, a CAT-5 Ethernet cable on deck connector or acoustic modems as shown in Figure 5.7. The Ethernet radios were used when piloting the vehicle for launch and recovery, or testing. The Ethernet radios can function when the AUV is piloted at the surface whereas below the surface the AUV is controlled by a mission file that is developed by Mimosa and downloaded to the VCC.

Figure 5.7: *E*thernet cable to communicate with the VCC via Ethernet radio

2. Pre-Dive Check

The purpose of the pre-dive check is to review and verify the functionality of the vehicle and its devices before and during the launching stage of the AUV operation. The AUV should not be launched until the pre-dive is complete and approved by the dive operation manager.

The mechanical pre-dive and the pilot pre-dive are two separate procedures. The mechanical pre-dive is done to verify the mechanical readiness of the AUV and to ensure that there are no mechanical deficiencies that may affect the performance of the AUV. When performing the mechanical pre-dive, damage of vehicle is inspected and fasteners are secured as shown in Figure 5.8. The pilot pre-dive is to check the functionality of the AUV and its devices, as well as the control capability of the thruster, planes, and communication system.

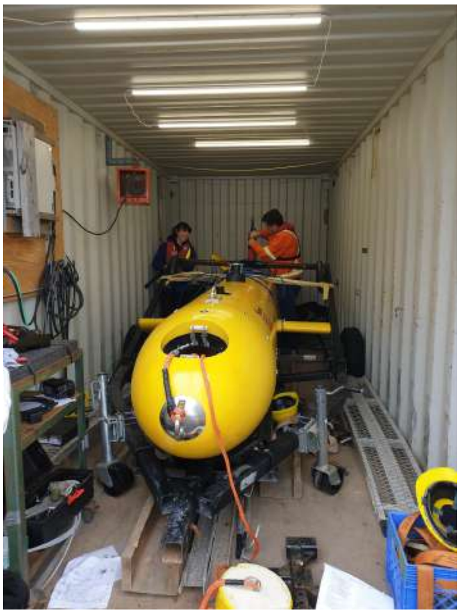

Area	Pre-Dive		Post-Dive	
	Damage (Y/N)	Fasteners (Y/N)	Damage (Y/N)	Fasteners (Y/N)
Pop-up buoy				
Tow rope				
OAS				
Planes x 6				
Fiberglass				
Buoyancy foam				
Acoustic window				
Pressure Hull				
USBL				
Acoustic modem				
Communication mast				
Antennas				
RF Beacon				
Propeller				
Lift lugs x 2				
Tow lugs x 2				
Drop weight				

Figure 5.8: Mechanical pre-dive testing [Left] and Mechanical pre-dive check list [Right]

3. Launch and Recovery

The launch and recovery of the *Explorer* may vary depending on the mission scenario and environment. Launch and recovery is generally done via lifting the AUV from the lifting lugs or using a support ship. In this case the vehicle was deployed using the boat trailer towed by the mini excavator as shown in Figure 5.9.

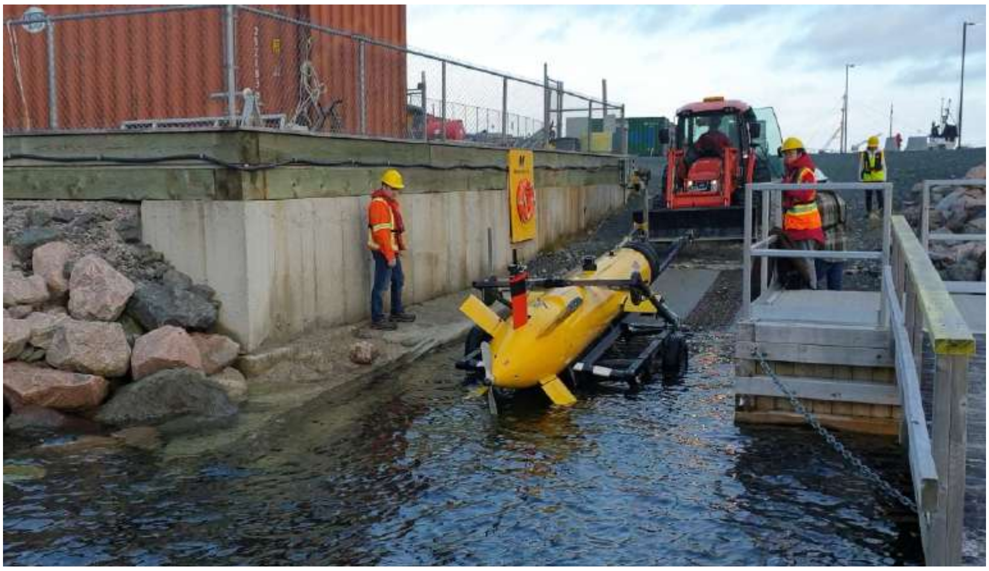

Figure 5.9: *MUN Explorer* AUV deployed by the mini excavator

4. AUV Area Coverage Mission

AUV coverage is currently one of the most popular features of AUV research due to the limitation of onbaord energy storage and hence the endurance of the AUV. The success rate of any AUV mission can be determined by the ability of the AUV to accomplish a targeted coverage of the intended search parameters in the shortest time highest possible at high accuracy and using the safest optimum path. Despite the advanced technology in the AUV, area coverage in underwater exploration is still less sufficient than airborne or land-based robotic vehicle. The reason can be the rapid attenuation of high-frequency signal, unstructured nature of underwater terrains and the lack of GPS coverage [84].

In order to investigate the performance of the proposed guidance law on the area coverage mission, four different mission cases were prepared as illustrated in Figure 5.10. Two type of coverage area were set up: a wide rectangle (Length 300 m $\times$ Width 200 m) and a tall rectangle (Length 200 m $\times$ Width 300 m), and each rectangle was covered by S-N direction and W-E direction. Two directions, S-N and W-E direction, are used to cover a certain area since the number of the turning points are highly dependent on the shape of the area of interest as shown in Table 5.1. In other words, the vehicle makes less turns when it operates in the direction in which the area of interest has a longer length. Figure 5.11 shows the waypoints and actual AUV track for the area coverage for the wide and tall rectangles respectively.

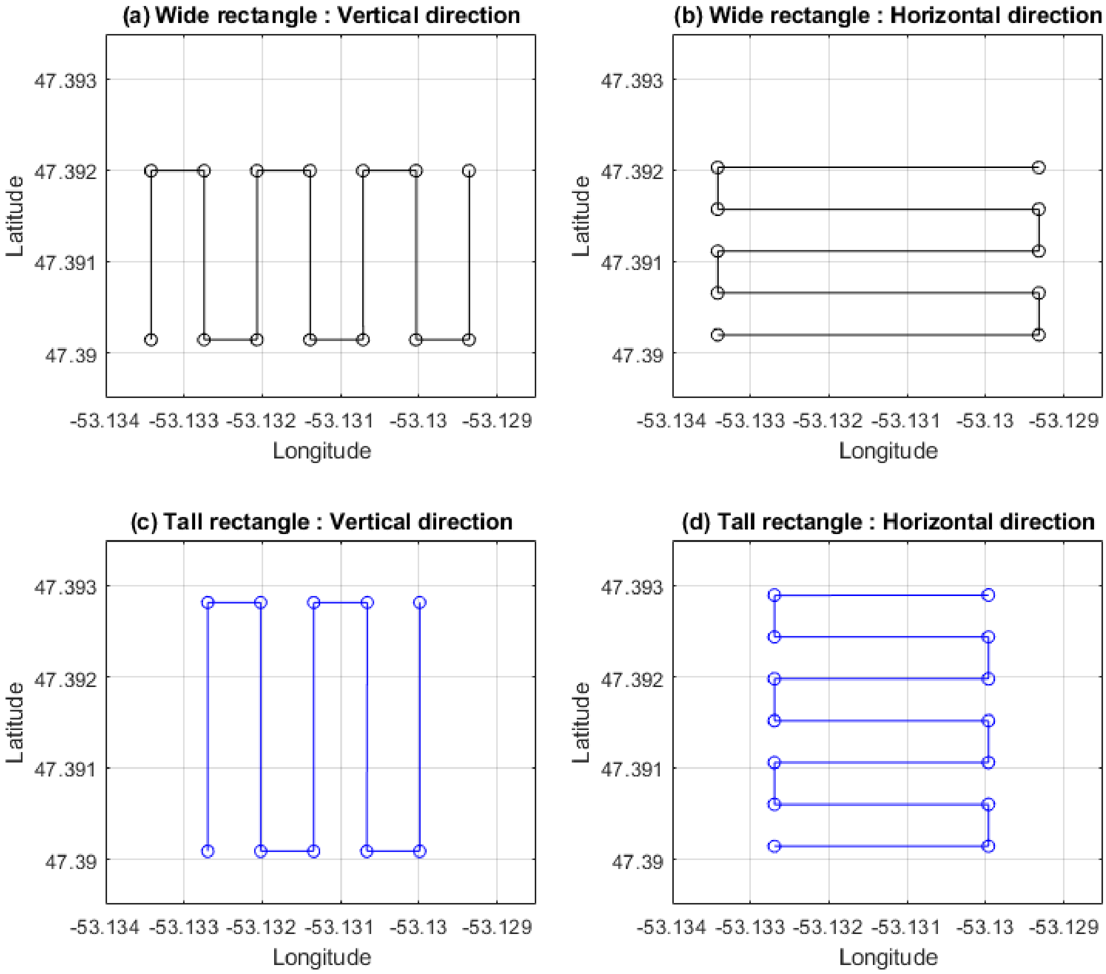

Figure 5.10: Four sets of waypoints for planning the experiment.

Table 5.1: Number of turning points for four simulation cases

Case number	Coverage Area	Following Direction	No. of turns
1	Wide rectangle	Horizontal	12
2	Wide rectangle	Vertical	8
3	Tall rectangle	Horizontal	8
4	Tall rectangle	Vertical	12

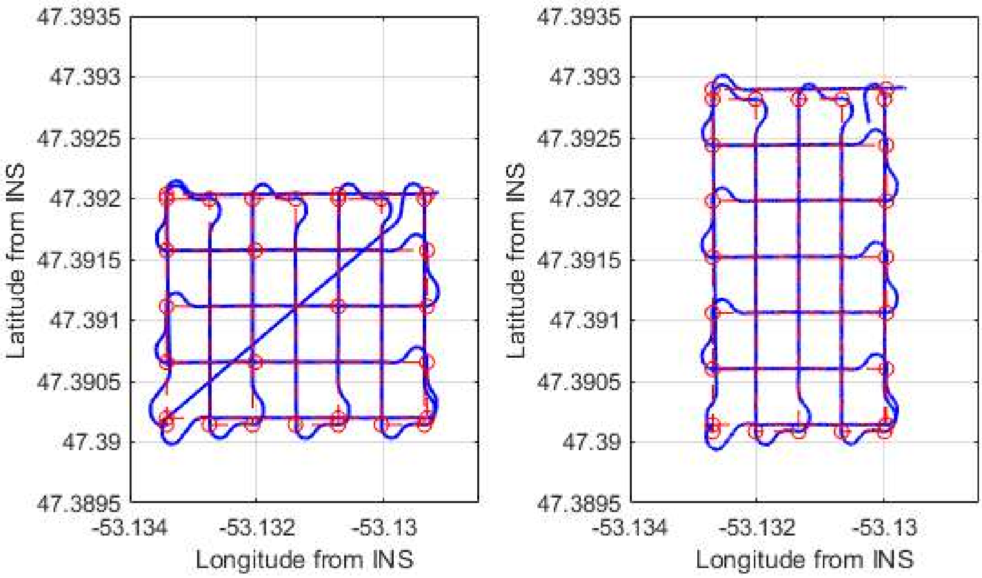

Figure 5.11: Overlapping the waypoint and the actual AUV track for the wide rectangle [Left] and Tall rectangle [Right]

5.5 Model Validation Using *MUN Explorer* Sea Trial

In this section, the main focus is to evaluate the performance of the hydrodynamical model developed for the *MUN Explorer* AUV. The underlying physics of this hydrodynamical model is based on the *component build-up* method. In order to validate the model, the numerical simulations were evaluated against the results from the sea trials. The efficiency and accuracy of the dynamical model are assessed by comparing the virtual and real AUV trajectories.

In the numerical simulations, a set of waypoints for the area coverage plan was used as an input as defined in the previous section. According to the path-following guidance logic, the guidance law was generated and downloaded to the controller. The desired deflection of the control planes was obtained by the PID controller while the propulsion was also calculated by the PD controller.

The position of the vehicle in geodetic latitude and longitude coordinates was transformed to the north-east-down (NED) system by using either the MATLAB function `geodetic2ned` or using the *MUN Explorer* AUV numerical simulation. For example, Figure 5.12 shows that the vehicle position in geodetic coordinates is transformed to the position in NED coordinates for the area coverage mission for the tall rectangle.

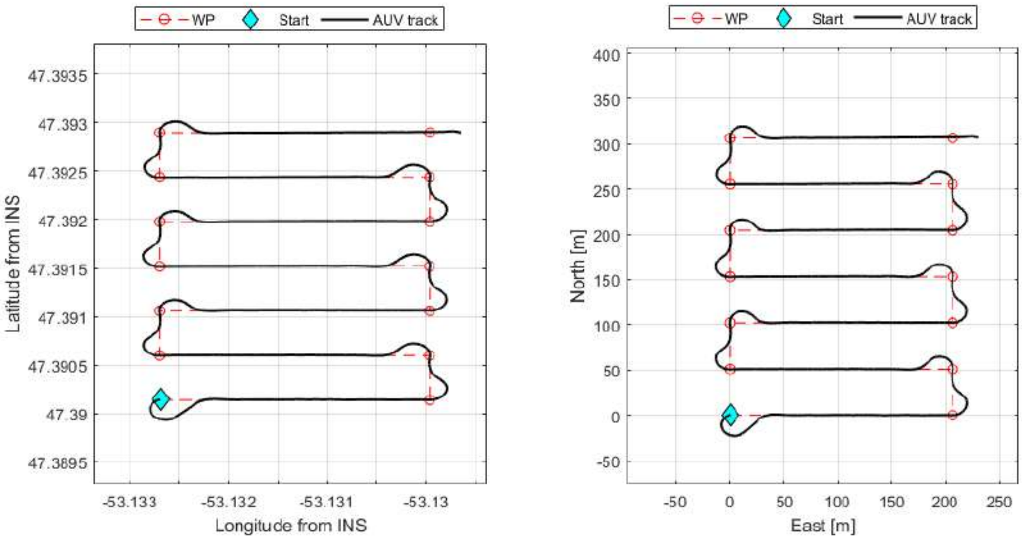

Figure 5.12: Transformation of the vehicle position from geodetic coordinate to the NED coordinate

The numerical model of the *MUN Explorer* AUV which was developed in the previous section 5.3 was used to simulate the motion of the vehicle for the four area coverage plans. In the simulation model, the *Line-of-sight (LOS) guidance* was used as a guidance scheme which involved a stationary reference point in addition to the interceptor and the target. In order to compare the simulation result with the experiment result, the initial conditions such as position and yaw angles were set the same as the experimental conditions tabulated in Table 5.2. An vehicle tracks from the experiment and simulation are shown in Figure 5.13 and 5.14.

An AUV track discrepancy between the experiment and simulation exists at the turning points. This is due to the reason that the reference values used in the simulation model such as the mass of vehicle, inertial parameters, centre of gravity and buoyancy might be different from the values from the experiment.

Despite the discrepancy of the AUV track between the experiment and simulation at the turning points, the simulation track closely resembles the experimental results at other locations.

Table 5.2: Initial conditions for four simulation cases

	Case 1	Case 2	Case 3	Case 4
Initial position in NED [m]	(0,0,0)	(0,0,0)	(0,0,0)	(0,0,0)
Initial heading [°]	250.73	221.47	309.51	234.74
Running time [sec]	1282	1250	1250	1290
Number of waypoints	13	9	9	13

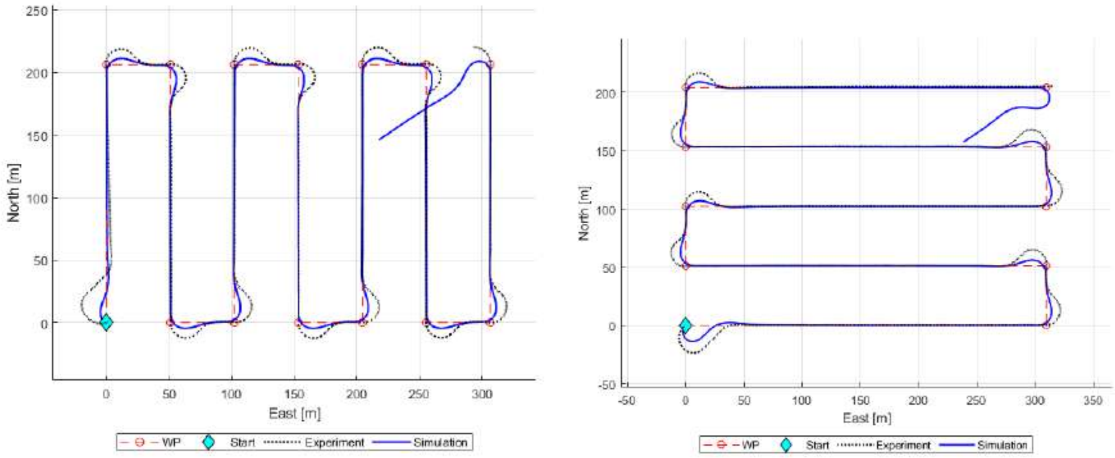

Figure 5.13: AUV tracks from the experiment and the simulation for the lawn mower path-following in the wide rectangle.

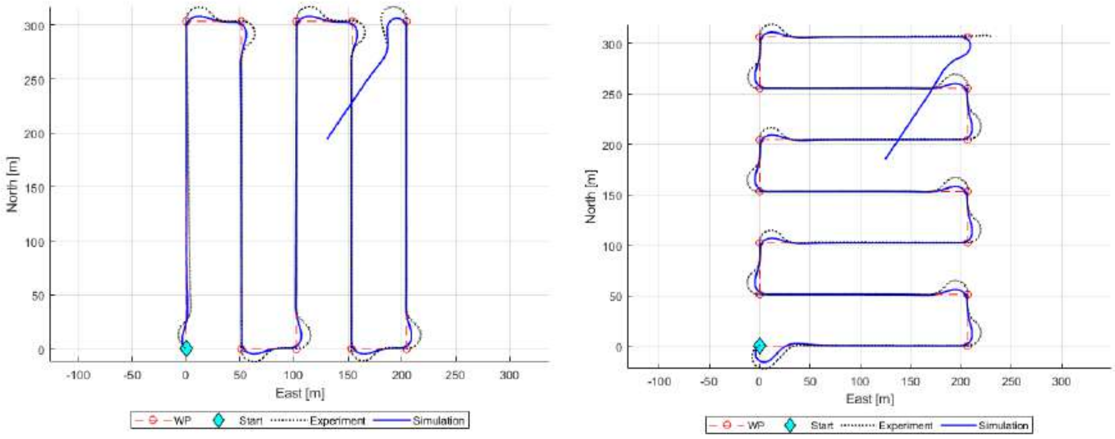

Figure 5.14: AUV tracks from the experiment and the simulation for the lawn mower path-following in the tall rectangle

5.6 Design of Guidance Law

The proposed path following guidance system was composed of the guidance law and the motion strategy of the virtual target. Three-dimensional path following guidance logic for a missile was proposed in [17] which combines the pure proportional navigation guidance (PPNG) law and the pursuit guidance (PG) law. In the missile community, the pure proportional navigation guidance (PPNG) law and pursuit guidance (PG) law have been widely used to focus on an enemy target [85]. The PPNG law keeps a constant LOS angle and ultimately guides a missile to a target. The PG law can direct the vehicle along the LOS regardless of vehicle and target velocities. To the best of the author's knowledge, this path-following guidance logic has not been applied to an underwater vehicle, so the performance and adaptability of this combined guidance law is investigated in the following section.

The overall kinematics of three-dimensional engagement for a vehicle and virtual target is illustrated in Figure 5.15. The inertial coordinate is expressed in {i}. $\vec{R}_m$ and $\vec{V}_m$ are the position and velocity vectors for the vehicle, while $\vec{R}_t$ and $\vec{V}_t$ are the position and velocity vectors for the virtual target. $\vec{R}$ is the position vector of the virtual target relative to the vehicle position or line-of-sight (LOS) vector.

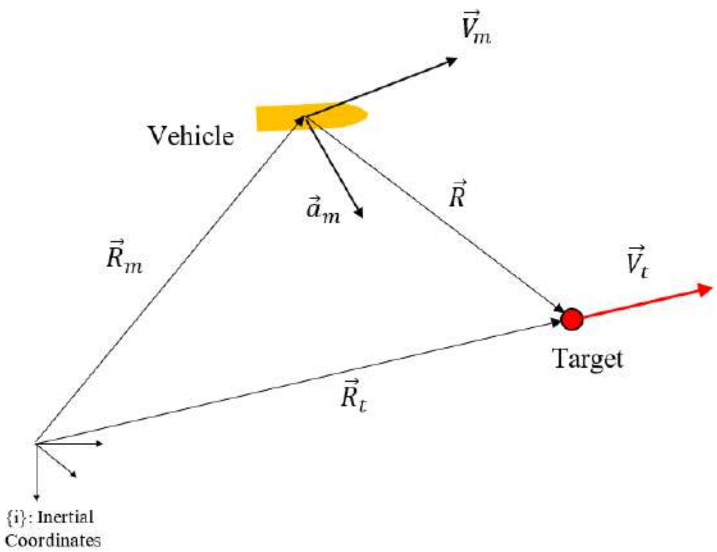

Figure 5.15: Vectors for the position and velocity of the vehicle and target in three-dimensions

In this frame, the path-following guidance law generates acceleration commands perpendicular to the velocity vector, which makes the vehicle pursue the moving virtual target. In other words, the velocity of the vehicle is not constrained by the guidance law because the path-following requires the vehicle to follow a desired path without any temporal restraint. On the other hand, trajectory tracking requires the vehicle to track with a time-parametrized trajectory [86].
In this study, the combined PPNG and PG law (referred to as the 'PPNAPG (Pure Proportional Navigation and Pursuit *Guidance*)') was proposed as the path following guidance law as in Equation 5.5.

$$a_m = N\frac{(\vec{R}\times\vec{V})}{R^2}\vec{V}_m - hN\frac{(\vec{R}\times\vec{V}_m)}{R^2}\vec{V}_m \tag{5.5}$$

where $N > 0$ and $V > 0$ are proportional and pursuit gains respectively, R the distance between the vehicle and target; and $\vec{V} = \vec{V}_t - \vec{V}_m$ is the relative velocity vector. The PPNG law and PG law are the first and second terms of Equation 5.5 respectively.

In order to specify the desired path, two waypoint vectors $\overrightarrow{WP}_i$,$\overrightarrow{WP}_{i+1}$ and a unit vector $\hat{e}_{t_i}$ are presented as shown in Figure 5.16. The waypoint vector is the position vector from the origin of the inertial frame to the position of the waypoint. The unit vector $\hat{e}_{t_i}$ is along the same straight line connecting two waypoints. The point D is the projection of the vehicle on the path. R_0 is the receding distance between the virtual target and the projection point D, and the receding distance is the design choice. The impact of the receding distance can be observed by linear analysis using a similar method to [87]. $\vec{R}_{m_i}$ is the position vector of the vehicle relative to the waypoint $\overrightarrow{WP}_i$.

The velocity of the virtual target is governed by the projection of the vehicle velocity on the straight path line. Thus, the vectors of the position and velocity of the virtual target are expressed as :

$$\begin{aligned}\vec{R}_t &= \overrightarrow{WP}_i + \left(\vec{R}_{m_i} \cdot \hat{e}_{t_i}\right) + R_0 \hat{e}_{t_i} \\ \vec{V}_t &= \dot{\vec{R}}_t = \left(\vec{V}_m \cdot \hat{e}_{t_i}\right) \hat{e}_{t_i}\end{aligned} \tag{5.6}$$

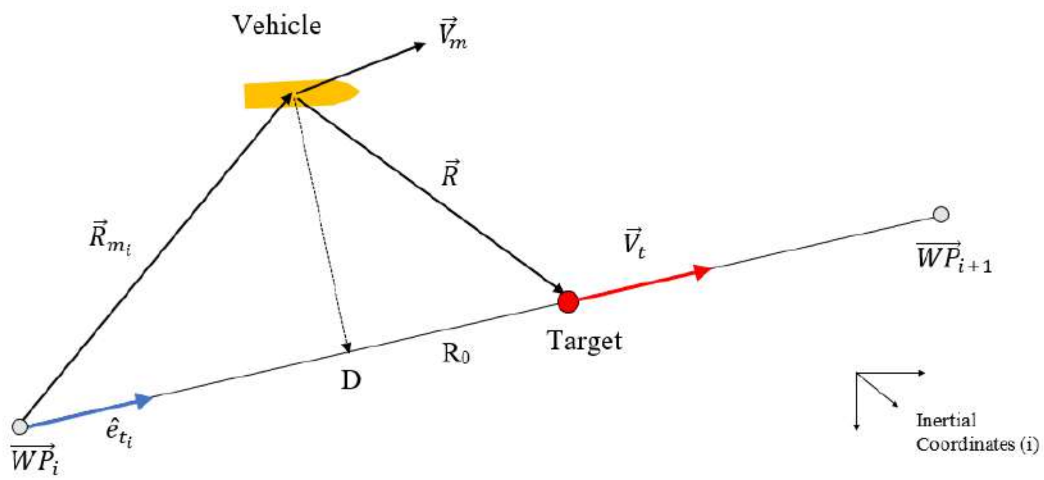

Figure 5.16: Desired straight line path using two waypoint

5.7 Results of the Guidance Law

In this section, the numerical simulations are presented to demonstrate the effectiveness of the proposed path following guidance logic. The path of the vehicle was defined in three dimensions and is assumed to be given to the vehicle. To illustrate straight-line following with the proposed guidance logic, four sets of waypoints, the same as in the sea trial, were considered, and the results are shown in Figures 5.17 and 5.18. In the first two simulations, the vehicle conducts the lawn-mower pattern to cover the wide rectangle in the S-N and W-E direction respectively as shown in Figure 5.17. Similarly the tall rectangle area was covered in two different directions as shown in Figure 5.18. The AUV track resulting from the PPNAPG (pure proportional navigation and pursuit guidance) is shown as the red curve in Figures 5.17 and 5.18 and is compared with the two AUV tracks from the experiment and simulation using the conventional LOS as the dashed-black and solid-blue curves respectively. From these figures, it can be readily seen that the AUV track by using the PPNAPG has no overshoot over the desired path, unlike the other two tracks. As a result, the PPNAPG allows the vehicle to reach the last waypoint in the shortest time.

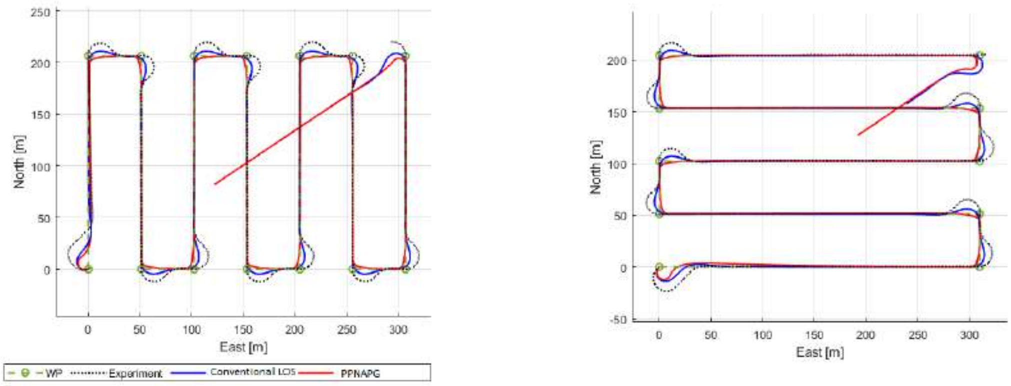

Figure 5.17: AUV tracks from the experiment and the simulation with the conventional LOS and PPNAPG for the Case 1 and 2

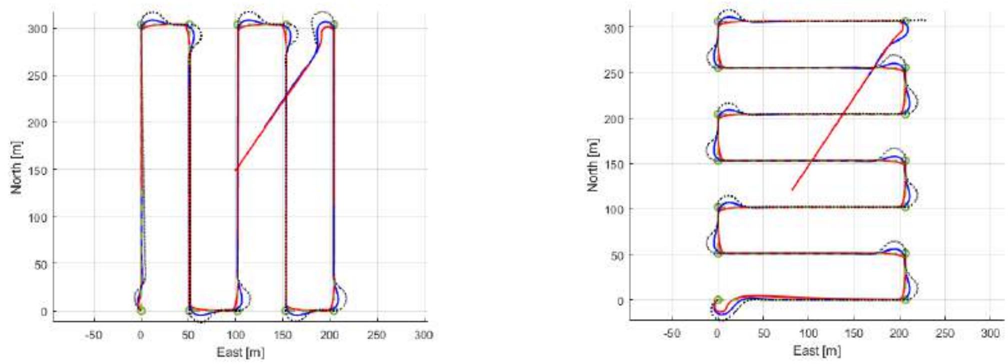

Figure 5.18: AUV tracks from the experiment and the simulation with the conventional LOS and PPNAPG for the Case 3 and 4

For example, the waypoints for the simulation case 1 - wide rectangle coverage area in S-N direction - are numbered from WP 1 to WP 13 as shown in Figure 5.19. Figure 5.21 shows the position of the vehicle in the North and East directions, which show the vehicle controlled by the PPNAPG reached the last waypoint (WP13) in the shortest time of 1130.01 seconds. While the LOS guidance system enabled the vehicle to reach waypoint 13 in 1182.28

seconds in the simulation, the vehicle reached the last waypoint in 1266.71 seconds during the experiment. The desired surge velocities for both the experiment and simulation were set as 1.5 m/s. As shown in Figure 5.20 the velocities were fluctuated at turning points, but the average of the velocities for the experiment and the simulation are 1.5002 m/s and 1.4947 m/s respective.

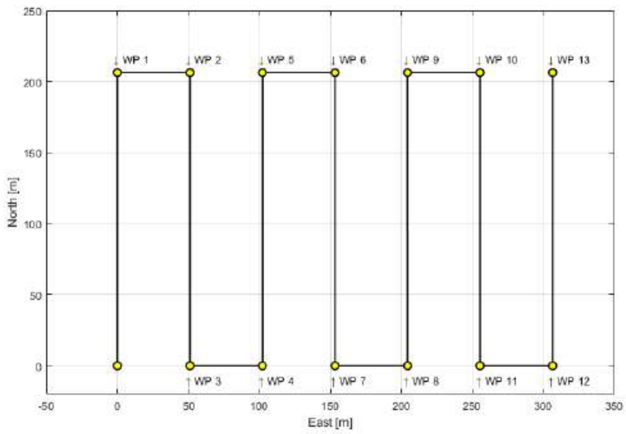

Figure 5.19: 13 waypoints for the simulation case 1

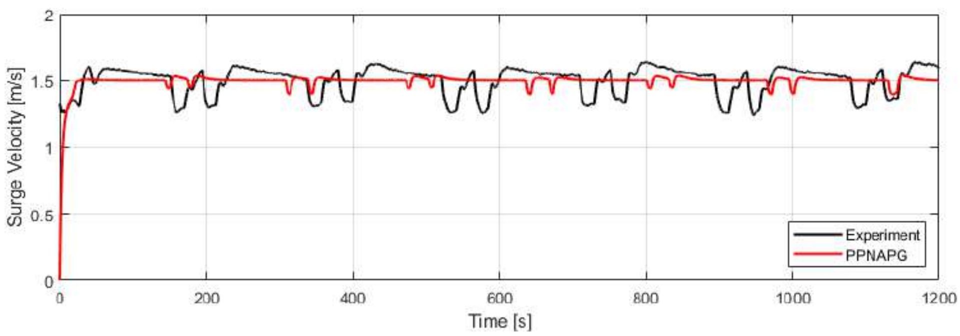

Figure 5.20: Surge speed for the simulation case 1

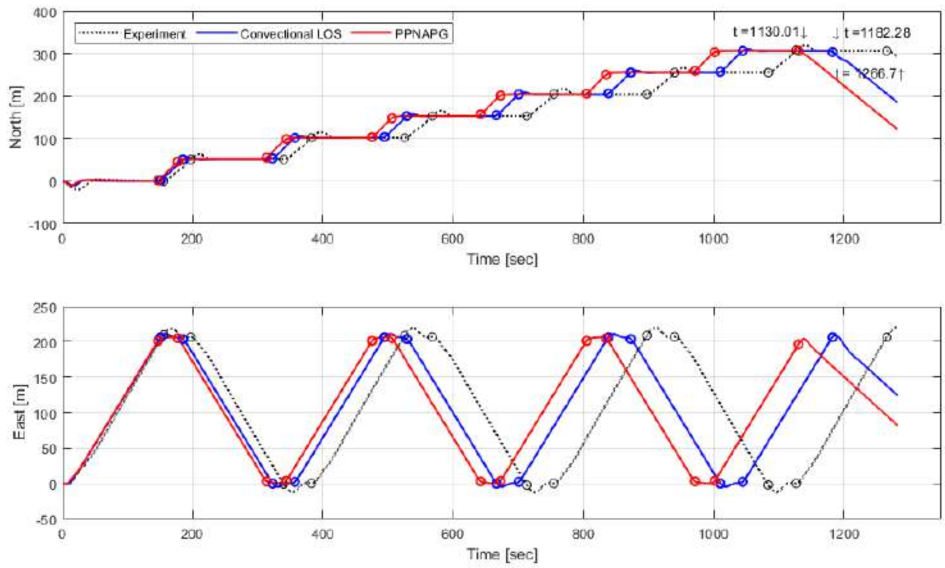

Figure 5.21: AUV positions in North and East in the experiment and simulations using the LOS and PPNAPG for the Case 1

The times taken to reach each waypoints (WP1 - WP 13) are shown in Figure 5.22 as well as the rate of the reduction of the time taken to reach each waypoints. The track resulting from the use of the PPNAPG shows the shortest time to reach every waypoints, and the track of the conventional LOS has slight longer time than the PPNAPG. The reduction rate of the time taken to each waypoints is calculated to assess the improvement of the proposed PPNAPG method by using the equation below:

Time reduction (%) $= \frac{\text{time taken for PPNAPG - time taken in the experiment}}{\text{time taken in the experiment}} \times 100$

The vehicles with the PPNAPG and the LOS in action reduced the time taken to reach the final waypoint by a maximum of -11.17% and -7.30 % compared with the time taken in the experiment.

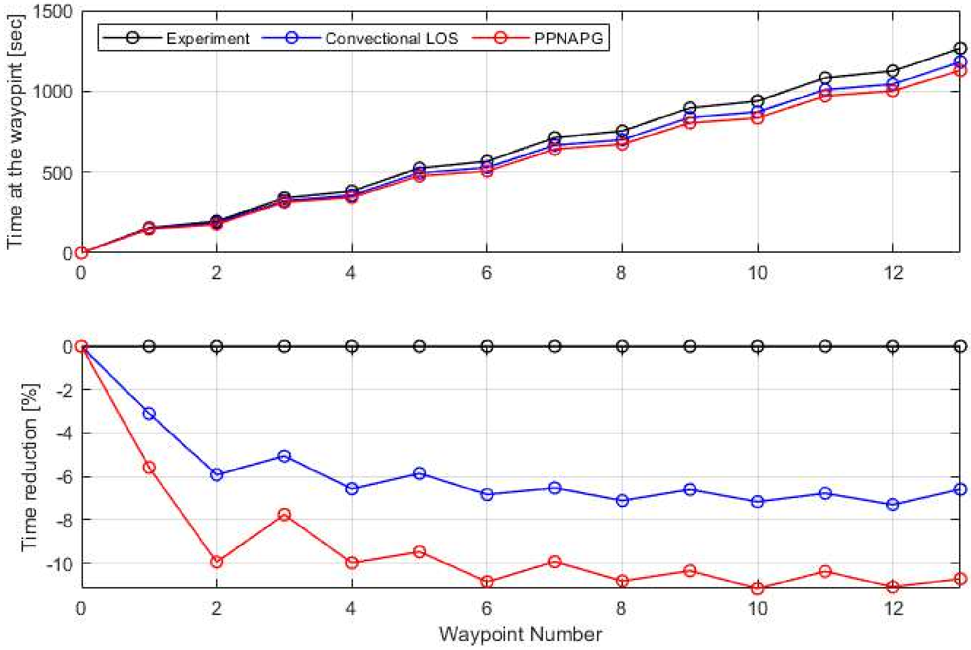

Figure 5.22: Proposed guidance law comparing to the conventional PID in the tall rectangle

Once it is seen that the vehicle using the PPNAPG passed the last waypoint in the shortest time, then the cross-track error can be calculated to validate the accuracy of the PPNAPG compared with the experimental result and simulation with the conventional LOS. To begin with, the cross-track error is defined as the shortest distance between the vehicle's position and the desired path connecting two waypoints as illustrated in Figure 5.23, and the calculated cross-track error is show in Figure 5.24. As shown in Figure 5.25, the vehicle using the PPNAPG exhibits better path following accuracy and stability with a smaller average and standard deviation of cross-track error than the other methods.

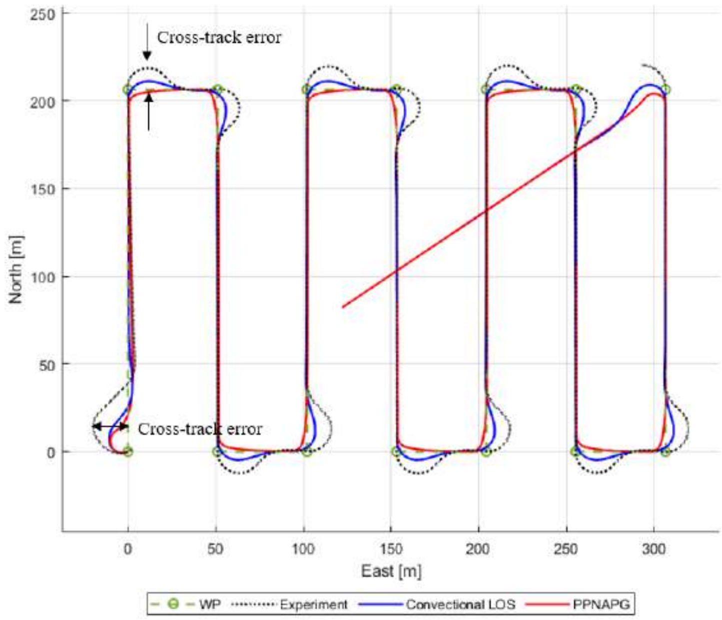

Figure 5.23: Proposed guidance law compared to the conventional LOS in the tall rectangle

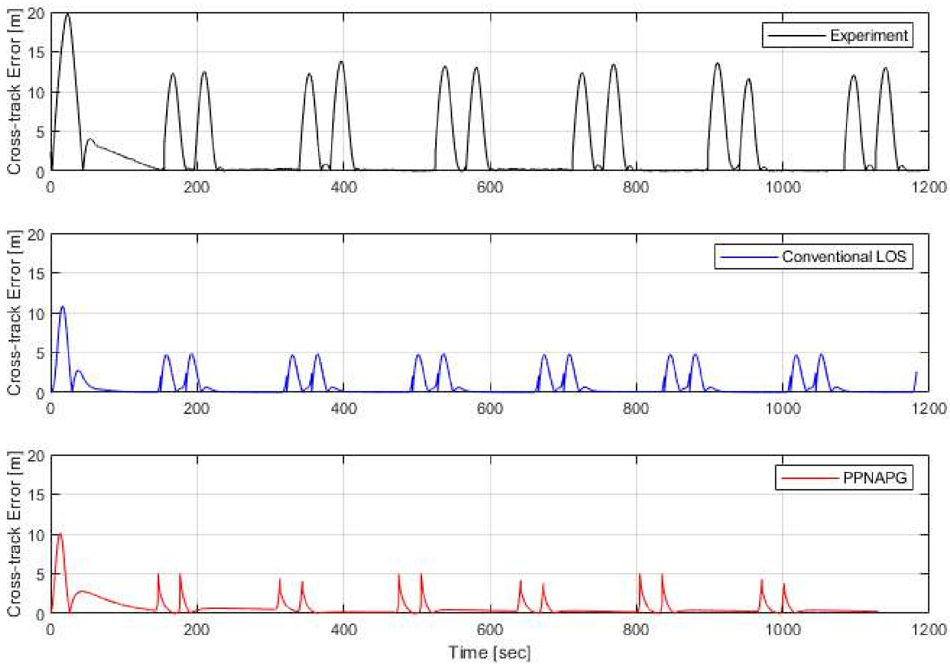

Figure 5.24: Cross-track error from the experiment and two simulation results using the LOS and PPNAPG

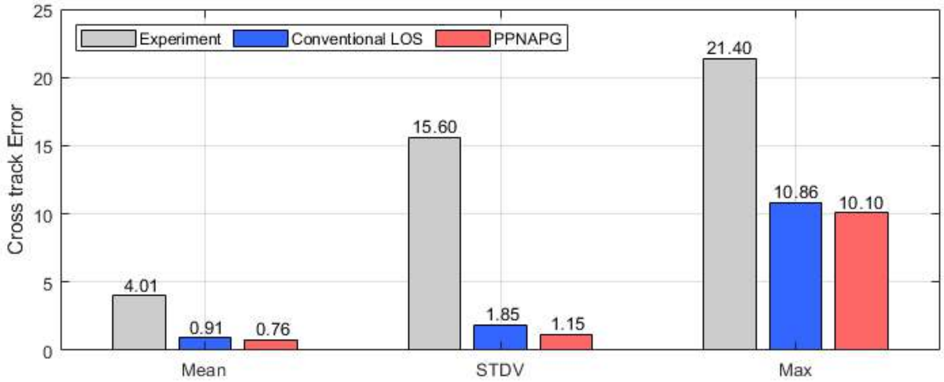

Figure 5.25: Cross-track error mean, standard deviation and maximum for the experiment, the conventional LOS and the PPNAGA

Side-scan sonar systems produce high resolution image representations of acoustic backscatter. They operate by emitting a narrow (in the fore-aft direction) acoustic pulse perpendicular to the along-track direction vector each side of the sonar/AUV. The pulse spreads out over a wide angle in the across-track plane to ensonify the seabed, as shown in Figure 5.26 [88]. Unlike the multibeam echo sounder sonar, a blind nadir zone is present for a side-scan sonar, so overlapping of returning runs in a common lawnmower pattern has been used to overcome this [89]. However, the blind nadir zone from using the side-scan sonar is not considered in this study since it is regarded as out of the research scope. Therefore, it is assumed that the AUV will emit a sonar swath wide of 25 m to cover the area of interest without the blind nadir zone throughout the simulations. The area coved by the side-scan sonar for the experiment, the conventional LOS and the PPNAPG for the simulation case 1, wide rectangle covered in S-N direction, are shown in Figure 5.27. All covered the area of interest sufficiently, but the PPNAPG allowed the vehicle to cover the area of interest with the smallest side-scan sonar coverage area as shown in Figure 5.28.

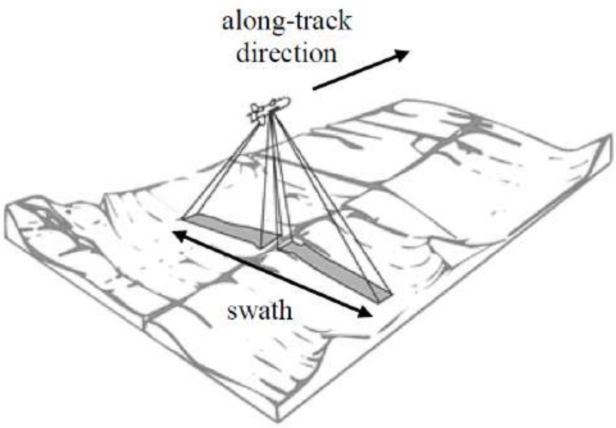

Figure 5.26: A depiction of a side-scan sonar imaging system [88]

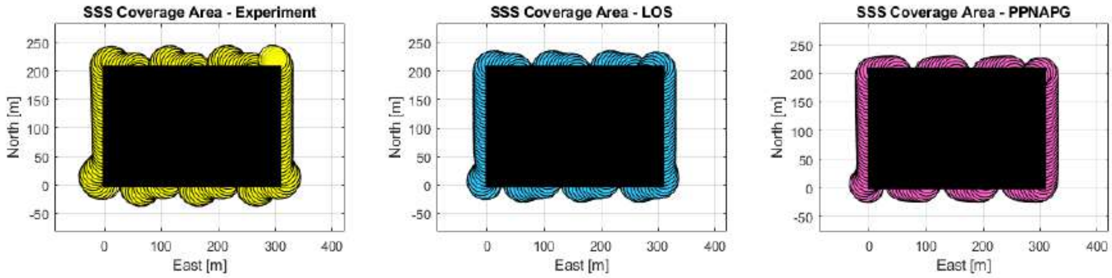

Figure 5.27: Side-scan sonar coverage area from the experiment, conventional LOS and PPNAPG

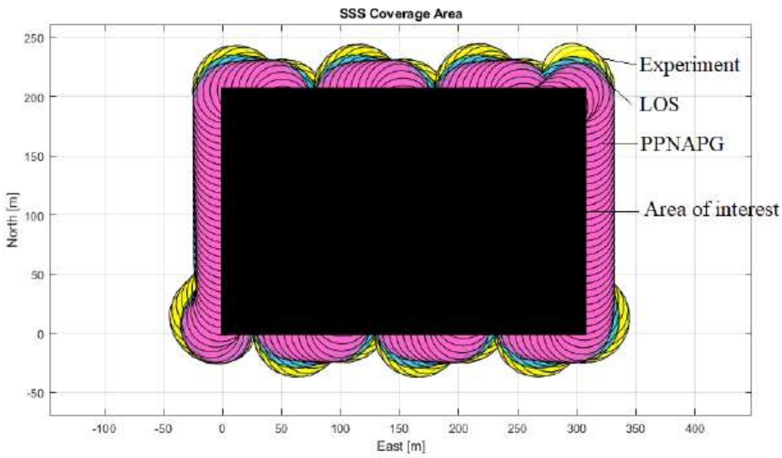

Figure 5.28: Comparison of side-scan sonar coverage areas from the experiment, conventional LOS and PPNAPG

5.8 Current Estimation

This section presents an approach for estimation and navigation in the presence of ocean currents. Several previous research groups have used an extended Kalman filter (EKF) to estimate ocean currents. Such an approach was validated in [90], where currents estimated by the onboard EKF in field testing closely matched actual currents calculated from deployed drifters. The estimation approach presented in [91] also uses an EKF to estimate water currents by including them in the state vector in a manner similar to [92].

5.8.1 Methods

The approach here was to use an EKF to estimate water currents in both north and east directions, which were combined with the speed through water (STW) estimate to give a better estimate of speed over ground (SOG). Motivated by the current estimation approach from [93], both the AUV state and water currents were estimated with the EKF. The EKF has n=6 states: east(E) and north(N) positions, STW(s), AUV heading(ψ), and east(C_E) and north(C_N) current:

$$x = \begin{bmatrix} E \\ N \\ s \\ \psi \\ C_E \\ C_N \end{bmatrix} = \begin{matrix} \text{East position [m]} \\ \text{North position [m]} \\ \text{Speed-through-water (STW) [m/s]} \\ \text{Heading [rad]} \\ \text{East water current [m/s]} \\ \text{North water current [m/s]} \end{matrix} \tag{5.7}$$

In Equation 5.7, speed-through-water (STW), s, is an estimate of the speed of the vehicle relative to the moving reference frame of the water current. Combined with heading, ψ, this gives an estimation of the velocity-through-water (VTW) of the AUV, which is still expressed in the water-current reference frame. In order to obtain the vehicle's velocity in the earth's reference frame, velocity-over-ground (VOG), the current velocities in east and north direction were added to the VTW as illustrated in Figure 5.29.

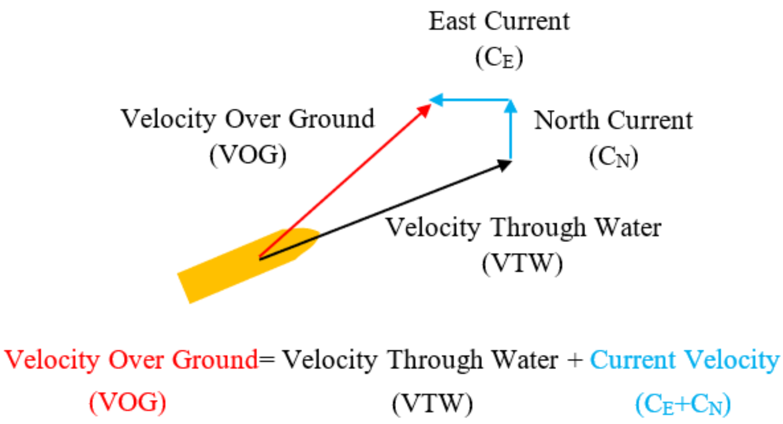

Figure 5.29: The relationship between VTW, VOG and current velocity

As a results, the VOG estimate was used in the kinematic propagation model of the EKF as shown in the equation below:

$$x_{k+1} = f(x_k, u_k, \omega_k) = \begin{bmatrix} E + s\sin(\psi)\Delta t + C_E\Delta t + \omega_E \\ N + s\cos(\psi)\Delta t + C_N\Delta t + \omega_N \\ s + \omega_s \\ \psi + \dot{\psi}\Delta t + \omega_\psi \\ C_E + \omega_{CE} \\ C_N + \omega_{CN} \end{bmatrix} \tag{5.8}$$

where $u = \dot{\psi}$; $\omega = [\omega_E \quad \omega_N \quad \omega_s \quad \omega_\psi \quad \omega_{CE} \quad \omega_{CN}]^T$.

In Equation 5.8, $\dot{\psi}$ is the heading rate collected from an onboard 3-axis gyroscope, Δt is the discrete sample time, and ω is a vector of the process noise related to the state in the EKF propagation model. The estimate from the propagation model should be corrected by utilising the measurement model which is associated with the measurement to the system state as :

$$\begin{aligned} y_k &= h(x_k, i_k, \nu_k) \\ &= \begin{bmatrix} E & +\nu_E \\ N & +\nu_N \\ s & +\nu_s \\ \psi & +\nu_\psi \end{bmatrix} \end{aligned} \tag{5.9}$$

where $\nu = [\nu_E \quad \nu_N \quad \nu_s \quad \nu_\psi]^T$, is a vector of measurement noise related to each measurement shown in below :

$$y = \begin{bmatrix} E_m \\ N_m \\ s_m \\ \psi_m \end{bmatrix} = \begin{array}{l} \text{East position from INS [m]} \\ \text{North position from INS [m]} \\ \text{Speed from propeller RPM correlation [m/s]} \\ \text{Heading from magnetic compass [rad]} \end{array} \tag{5.10}$$

The measurement rate for the RPM speed, INS and DVL can be separately specified using the Surface Control Computer (SCC) before the mission. Although the rates for these measurements were allocated differently, the total payload log was generated at a consistent sampling rate, Ts = 0.1 second during the test. The GPS was not used for the AUV position and hence the difference between the GPS's low measurement rate and faster measurement rate estimated from dead reckoning from rpm and heading was not required. GPS fixes can be obtained for reference and correction of the dead-reckoning based positions during the periods the AUV is at the surface.

5.8.2 EKF Covariance Matrices

It is noticed that an observable system can be created by combining the propagation model 5.8 and measurement model 5.9. The EKF utilises three covariance matrices: the process noise covariance $Q_{n\times n}$, the measurement noise covariance $R_{m\times n}$ and the state covariance $P_{n\times n}$. These square matrices are usually diagonal with values corresponding to the square of the standard deviation of the corresponding process, measurement, or state respectively. The covariance matching technique in [94], is an adaptive algorithm in which the estimates of the process noise covariance (Q) and measurement noise covariance (R) are computed at every sampling instant. Using the past data of the state prediction trajectories, the sample covariance of the state prediction error is computed either cumulatively over the entire data in the past or over a moving window in time [95]. However, applying the covariance matching technique is beyond the scope of the present research and the standard deviations for the noise covariance matrices were estimated based on typical error bounds associated with the process and measurement.

The process noise covariance matrix describes uncertainties associated with the estimations used to simplify the propagation model 5.8. These estimations include discrete time step approximations, numerical integration order, etc.. The covariance values were estimated based on typical error bounds associated with these approximations. The covariance values for the current were small values ($1e$-06 m^2/s^2) and this implies that the current was slowly changing. The process noise covariance matrix is given as:

$$\begin{aligned} Q = \text{diag}(\sigma_{\omega E},\ \sigma_{\omega N},\ \sigma_{\omega s},\ \sigma_{\omega\psi},\ \sigma_{\omega cE},\ \sigma_{\omega cN}) \\ \sigma_{\omega N},\ \sigma_{\omega E} &= 0.01m^2 \\ \sigma_{\omega s} &= 1e-04m^2/s^2 \\ \sigma_{\omega\psi}, &= 1^\circ = 0.0175\,rad \\ \sigma_{\omega cE},\ \sigma_{\omega cN} &= 1e-04m^2/s^2 \end{aligned} \tag{5.11}$$

The measurement noise covariance matrix contains estimates of the noise related with each measurement update, which has the variance determined from statistical analysis of historical data [91]. The measurement noise covariance matrix is:

$$\begin{aligned} R = \text{diag}(\sigma_{\nu E_m},\ \sigma_{\nu N_m},\ \sigma_{\nu s_m},\ \sigma_{\nu\psi_m}) \\ \sigma_{\nu N_m},\ \sigma_{\nu E_m} &= 0.0025m^2 \\ \sigma_{\nu s_m} &= 1.6e-02m^2/s^2 \\ \sigma_{\nu\psi_m}, &= 0.0255\,rad^2 \end{aligned} \tag{5.12}$$

The state covariance matrix is an estimate of the error associated with the current estimate of each state. This covariance matrix was initialised based on the variance of the measurements used to initialise the EKF. Since the *MUN Explorer* AUV has no real-time current information, the covariance on the initial state estimation for both east and north currents were set high enough for the expected current magnitude. The state covariance matrix is given as:

$$P = \text{diag}(1m^2,\ 1m^2,\ 1.5m^2/s^2,\ 0.1218rad^2,\ 0.1m^2,\ 0.1m^2) \tag{5.13}$$

5.8.3 Acoustic Doppler current profilers (ADCPs)

Measuring waves and currents is an important field of study for a variety of applications, including safe and secure waterway navigation, offshore renewable energy, weather forecasting, and scientific research. Acoustic Doppler Current Profilers (ADCPs) can collect data with spatial and temporal sampling resolutions that facilitate capturing detailed features of the flow field in natural rivers [96]. The ADCP model used in this field test was the TRIAXYS$^{\text{TM}}$ Directional Wave Buoy, whose sensor unit is comprised of three accelerometers, three rate gyros, a fluxgate compass, and the proprietary TRIAXYS$^{\text{TM}}$ Processor. As shown in Figure 5.30, the buoy's modular components are easily accessed by removing the polycarbonate dome. The buoy's stainless steel hull has a high strength to weight ratio and corrosion resistance, and provides secure mooring and lifting points. The clear dome allows sunlight to reach the solar panels, while maintaining a low profile and impact resistance. The buoy is solar powered with rechargeable batteries to reduce annual operating costs. The buoy can operate for years before the batteries need replacement [97].

Figure 5.30: *MUN* 's TriAXYS$^{\text{TM}}$ Directional Wave Buoy in Holyrood [left and middle] and its components [right]

The TriAXYS buoy was prepared for deployment as illustrated in the assembly drawing [98], see Figure 5.31, and then it was deployed on 31, October, 2019 in Holyrood Bay as shown in the map of Figure 5.31. The water depth was expected to be most 21m, so the rope to the subsurface float (shown in 6 in the assembly drawing) was adjusted to have the subsurface float at half of the water depth. The position where the TriAXYS buoy was deployed was 1.6 km away from the location of the area coverage test since the buoy and its mooring rope create an obstacle for the AUV if the AUV operates too close to the buoy. However, it has to be assumed that the current near the area where AUV executed the area coverage mission was similar at least in magnitude to the current measurements from the TRiAXYS buoy. In order to provide some comfort that this assumption was reasonable, another set of current measurements are presented which were located 6.64km away from the TriAXYS buoy (Figure 5.32). These had a similar tendency to the current pattern of the TriAXYS buoy (see Figure 5.33). The other set of current data is accessible thanks to the Ocean Networks Canada which monitors the west and east coast of Canada and the Arctic to continuously deliver data in real-time for scientific research [99]. Thus, the current near the operating AUV was assumed to be equal to the current measured from the TriAXYS buoy although the TriAXYS was located 1.6 km away from the area coverage mission point.

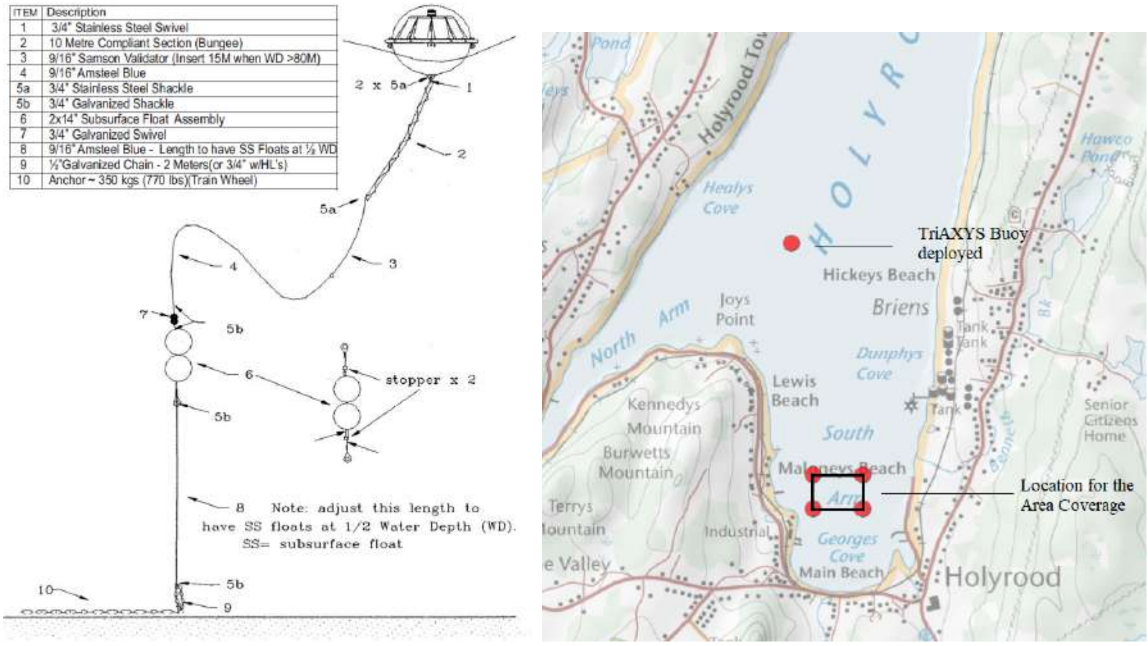

Figure 5.31: Assembly drawing for the TriAXYS Buoy [Left] and the location where the TriAXYS buoy was deployed [100]

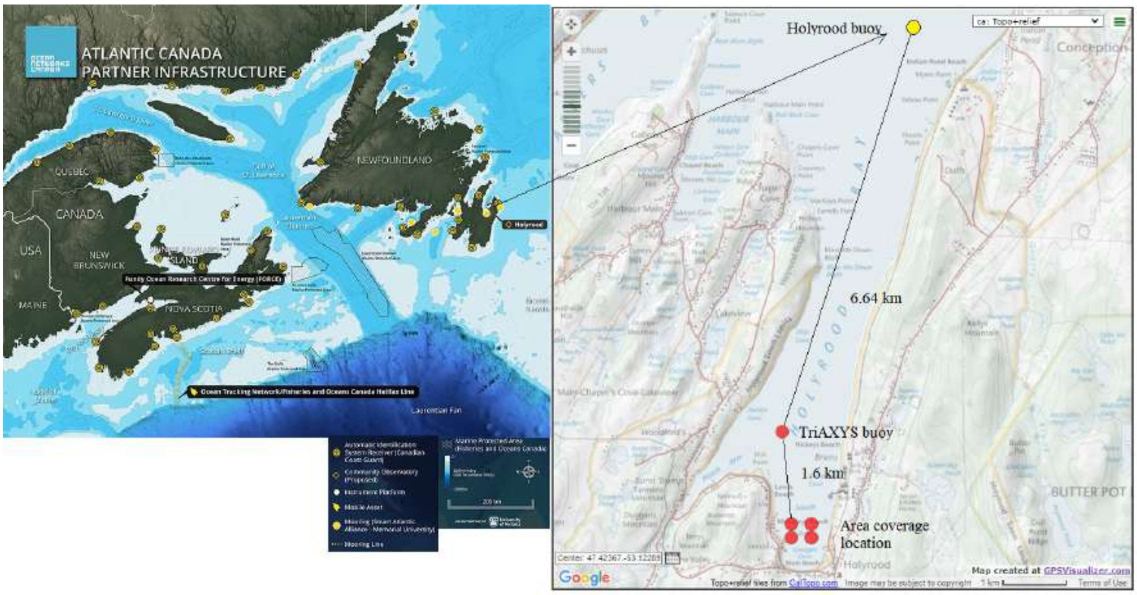

Figure 5.32: Nortek Aquadopp ADCP in the Holyrood bay as part of Ocean Network Canada [Left], which was 6.64km away from the TriAXYS buoy [Right]

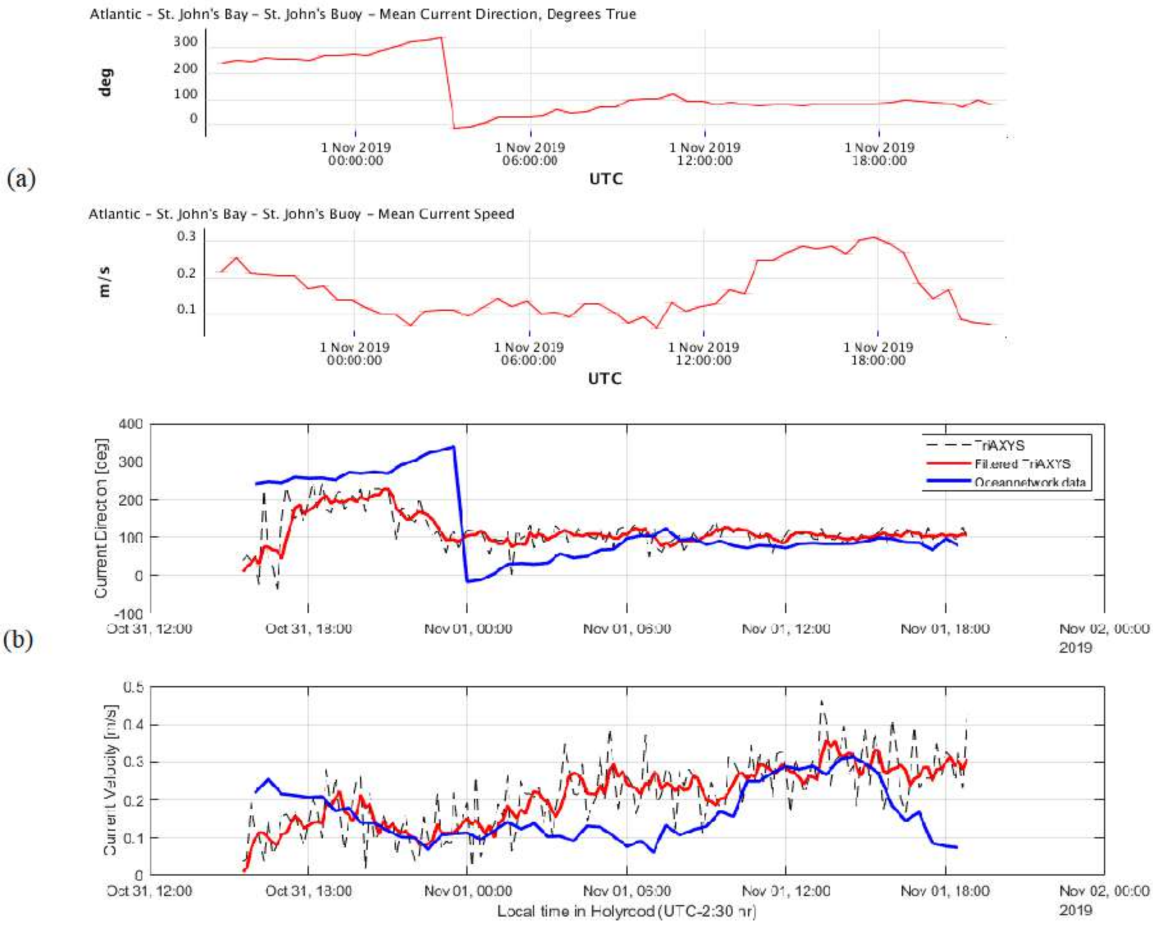

Figure 5.33: (a) Mean Current direction and speed data in Holyrood Bay from the Ocean Network Canada (b) Current data comparison between the TriAXYS buoy and the Ocean Network data

5.8.4 Current Estimation Results

In this section the current velocities were estimated in the x and y directions by utilising the extended Kalman filter (EKF), then the current estimation error was analysed to evaluate the estimation accuracy and stability by comparing the output with the current measurements. The direction and magnitude of current were measured by using a TriAXYS™Directional Wave Buoy fitted with a 600 KHz current profiler on 1, November, 2019 in Holyrood Bay. The ADCP was programmed to profile approximately 50 m of the water column in 1 m range bins as shown in Figure 5.34. The closest bin was 1.48 m away from the buoy which is referred as the blanking distance. There were 50 bins measured by the ADCP, but data from only six bins (bin 1 -6) closest from the ADCP were considered in this study since the AUV was operated at a constant depth of 5 m during the area coverage mission.

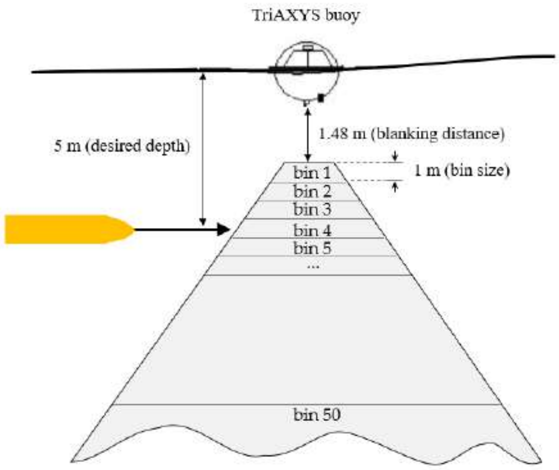

Figure 5.34: Configuration of ADCP beam geometry and the desired depth for the AUV

Four cases of the area coverage mission were carried out in a row without any break from noon, and all cases took around 20 minutes as previously mentioned in Table 5.2. The current direction during the AUV mission was mostly from northwest as indicated in Figure 5.35 which shows direction and magnitude of the current from the six bins.

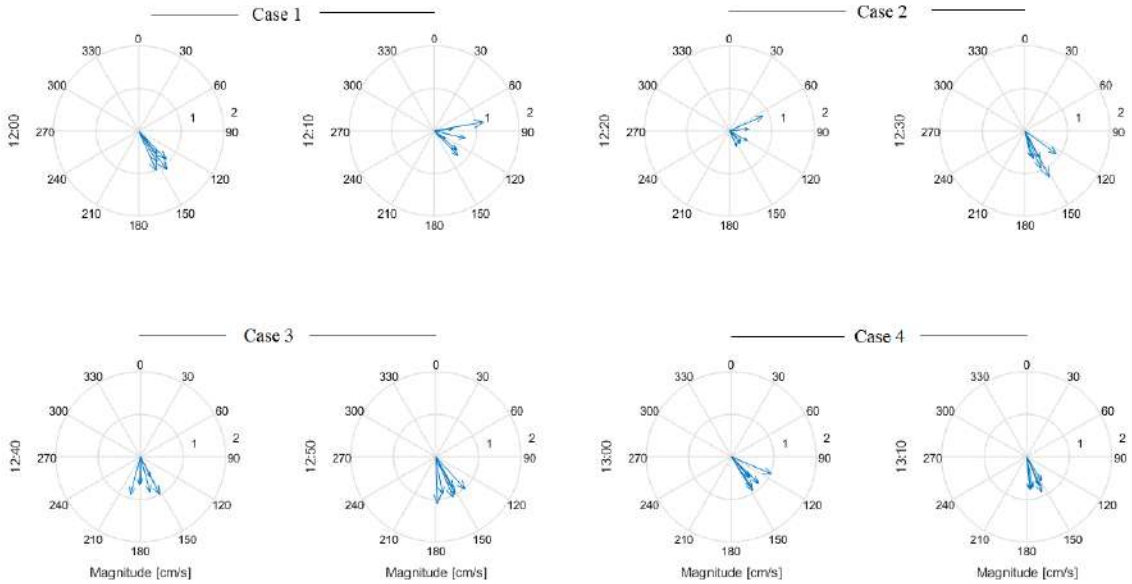

Figure 5.35: Displaying the directions and magnitudes of current during four area cover mission cases from six bins (bin 1-6)

Since each case took around 20 minutes, the current trend changed slightly having two measurements for one AUV mission. In other words, the current information for one mission was decided by averaging two sets of six bin results for 20 minutes and this is tabulated in Table 5.3. In the table, the current direction and magnitude are transformed to the velocity in the East and North direction which will be compared with the estimated current velocity during the AUV missions by the EKF. The current for each case is illustrated with the AUV's actual track for the area coverage missions in Figure 5.36 to demonstrate the current trend about that time.

Table 5.3: Average vales of current magnitude, direction and velocity from six bins (bin 1-6) for four mission cases

	Case 1	Case 2	Case 3	Case 4
Time [UTC-2:30]	1200-1220	1220-1240	1240-1300	1300-1320
Magnitude [m/s]	0.8150	0.6817	0.8750	0.8067
Direction [°]	126.5833	134.4167	164.5833	149.4167
East Current [cm/s]	0.5471	0.4474	0.1155	0.5818
North Current [cm/s]	-0.7438	-0.2198	-0.7579	-0.6059

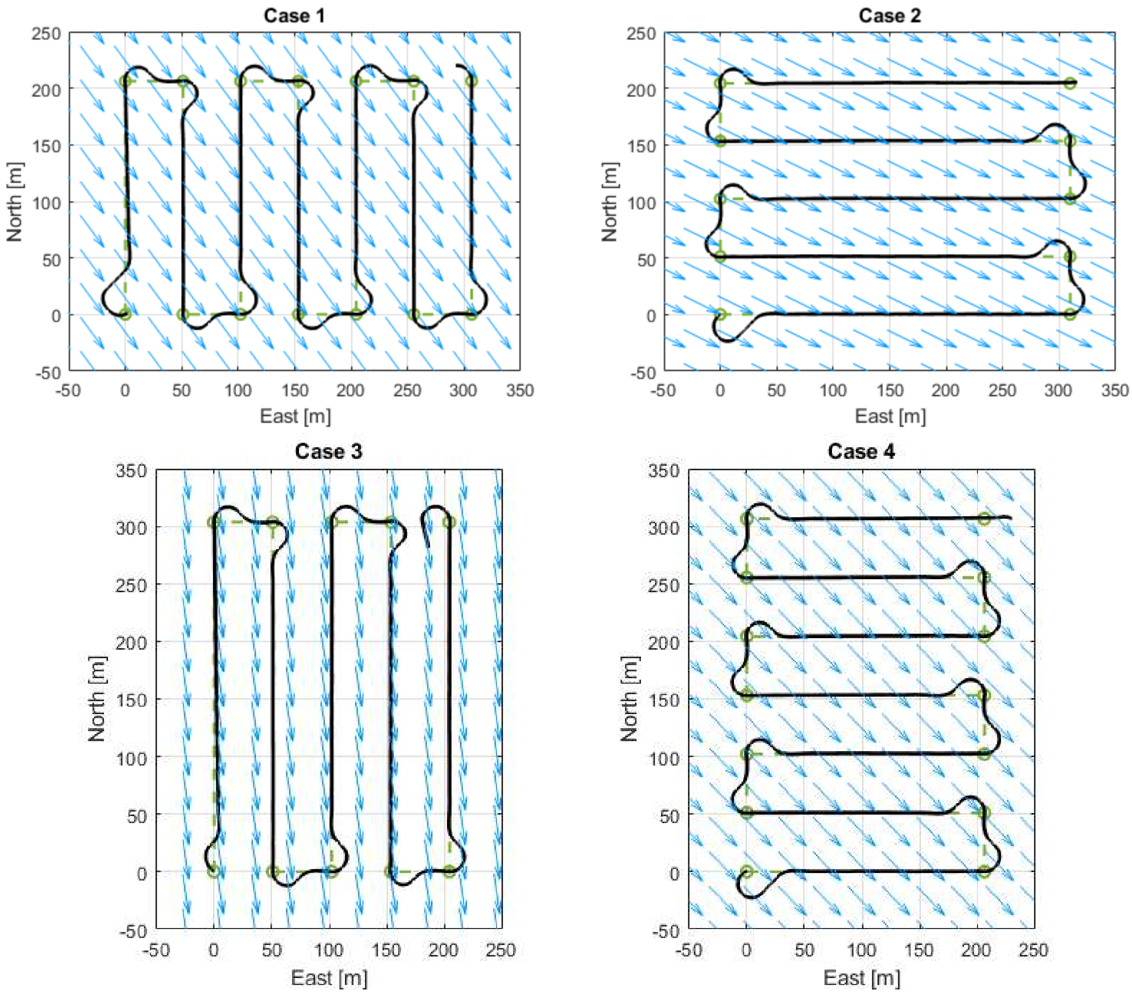

Figure 5.36: Actual AUV tracks during the area coverage missions and the current field from the ADCP measurement

The current velocities were estimated by the EKF as described in Section 5.8, and Figure 5.37 (a)-(d) shows these together with the measured current velocities from the ADCP in East and North direction for four cases. As mentioned previously, the measured current velocity is decided by averaging the two sets of six bin results for 20 minutes. The estimate noise was noticeable in Case 2, resulting from the dispersion of the ADCP measurement from the six bins through the testing. Although noise was found in the estimated current velocities, those from the EKF were matched with the measured current velocities from the ADCP. The Gaussian-weighted moving average filter was used to smooth noisy data over each window of 100, as shown in Figure 5.37 (a)-(d). The original estimate by the EKF and the filtered estimates with window sizes 50 and 100 are compared in Figure 5.37 (e).

In order to evaluate the performance of the EKF more accurately and quantitatively, additional data analysis of the estimation error was carried out. Two parameters - the average value of the absolute estimation error and the standard deviation of the estimation error -

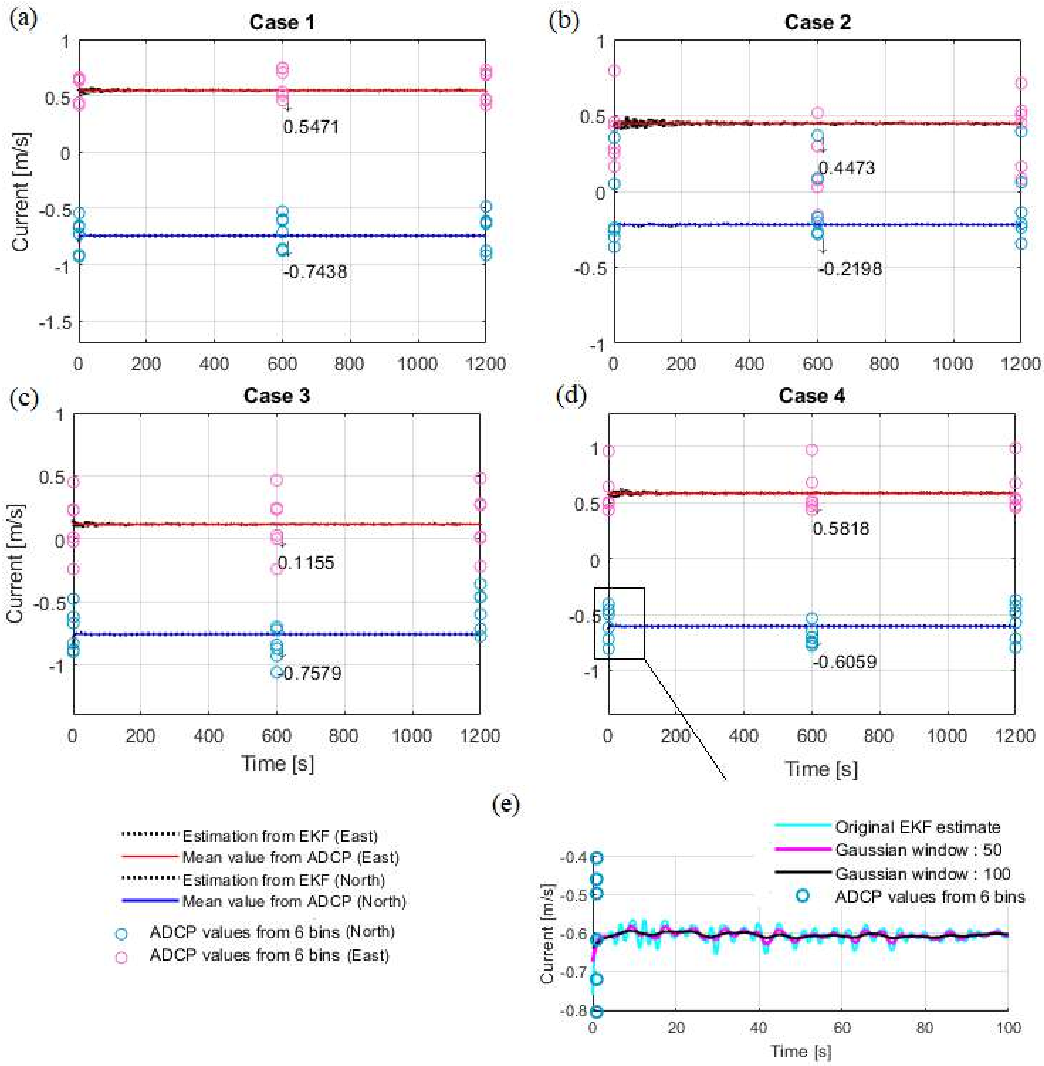

Figure 5.37: Estimated current by EKF and measured velocities for four cases of the area coverage mission (a-d) and the original estimate by EKF and filtered estimate by using the Gaussian weighted filter with the moving window length of 50 and 100 (e)

were calculated to assess the accuracy and stability of estimating the current velocity (Figure 5.38). The standard deviation directly reflects the ability to estimate the current velocity while the average reflects the estimation accuracy. As shown in Figure 5.38 (a), the average value of estimation error in both East and North directions are similar in all four cases with the maximum value of 0.021 for the North directions of Case 2. In terms of the standard deviation, the maximum values in East and North directions are also from Case 2 as shown in Figure 5.38 (b). Furthermore, an estimation error ratio was calculated according to Equation 5.14 to see the performance of the EKF to estimate the current velocity.

$$Error\ ratio(\%) = (V_{ADCP} - V_{Est})/V_{ADCP} \times 100 \tag{5.14}$$

The unusual aspect of the present estimation analysis is that the highest error ratio was from the East current estimation of Case 3 with the value of 0.038% as shown in Figure 5.38 (c). However, the current velocity estimates for East and North were obtained by the EKF, and the standard deviations of the current velocity estimates lay within the uncertainty margin of the ADCP, which was ±0.1 m/s for both simulation cases. The velocity measurements taken from an AUV-fixed ADCP typically have an uncertainty margin of 0.1 m/s [70]. Hence the standard deviation of the current estimate found by the EKF are within the expected uncertainty margin of ADCP measurements and this verified the performance of the EKF for current estimation.

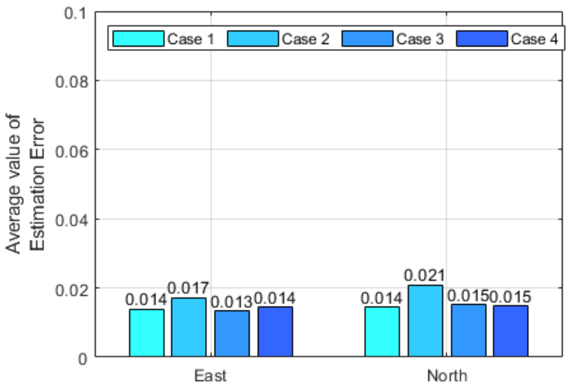

(a)

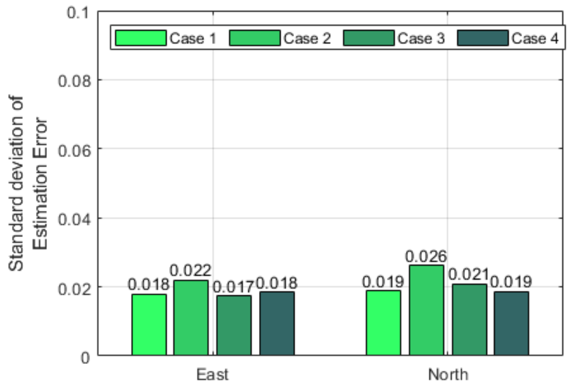

(b)

Case No.	Current Direction	ADCP Measurement (V_{ADCP})	Estimate Average (V_{Est})	Error ratio (%)
Case 1	East	0.5471	0.5470	0.011%
	North	-0.7438	-0.7440	0.024%
Case 2	East	0.4473	0.4474	0.031%
	North	-0.2198	-0.2197	0.026%
Case 3	East	0.1155	0.1155	0.022%
	North	-0.7579	-0.7582	0.038%
Case 4	East	0.5818	0.5817	0.009%
	North	-0.6059	-0.6060	0.010%

(c)

Figure 5.38: Average value (a) and standard deviation (b) of estimation error. Tabulated value for each cases and direction (c).

5.9 Conclusion

In order to verify the capability of the path following guidance system using 'PPNAPG (Pure Proportional Navigation And Pursuit Guidance)', both simulations and experiments were carried out. Firstly, a dynamic model of the *MUN Explorer* AUV was built by using the *component build-up* method, and the model was validated by utilising data from sea trials. The simulation results were closely matched with the AUV's actual track within a thin margin of discrepancy at the turning point near to the waypoints. The proposed guidance system combines the pure proportional navigation guidance (PPNG) law and pursuit guidance (PG) law. The performance of the PPNAPG guidance system was quantitatively validated by analysing the cross-track error compared with the counterparts from the experiment. The PPNAPG allowed the vehicle to pass the waypoints in a shorter time than the conventional LOS guidance law, and this resulted in a 11% reduction in the time compared with the time taken in the experiment.

The extended Kalman filter (EKF) was applied to estimate the current velocity by using measurements from GPS, rpm and heading angle. The estimated current velocities were compared with the current measurement from a TriAXYS ADCP buoy, which validated the ability of the EKF to estimate current velocities in East and North directions with a standard deviation around 0.0187 and 0.0212 respectively.

CHAPTER 6

Summary, Conclusions and Future work

This chapter brings together the findings of the individual chapters. It also concludes the findings and outcomes, and discusses the implications of the findings, the limitations, and the recommendations for further research.

6.1 Research Summary

In this thesis, the application of the nonlinear observers -HGO (High-gain Observer) and the EKF (Extended Kalman Filter)- for current estimation, the path following guidance systems and AUV dynamic model identification were examined. This thesis provides an answer to the following question:

"Can nonlinear observers be used to enhance the localisation of AUVs and can a guidance system be improved for the path-following tasks?"

In achieving the research objectives, the literature review focused on research that improved the AUV's localization performance by estimating and compensating for the current and designed new guidance systems to enhance an AUV's path following performance. Comparing the nonlinear estimator options available, it was decided to use the HGO and the EKF to estimate current velocities because of their efficiency and proficiency in terms of representing nonlinear dynamic models for AUVs.

In the first step, the current velocity was estimated to validate the performance of the HGO in estimating current velocities around an AUV. The current velocities were estimated by calculating the difference between the vehicle's absolute velocities over the ground and the relative velocities through the water estimated from the AUV model based HGO. The observer gain was obtained by solving the Linear Matrix Inequalities (LMIs) which represents the error dynamics equation. In the numerical simulation, the vehicle's relative velocities were firstly estimated through the HGO and then the current velocity was further calculated by subtracting the vehicle's relative velocities from the absolute velocities.

Furthermore, a Gavia AUV was used to conduct a straight-line, constant depth mission to record the current velocities and vehicle velocities by utilising an on-board ADCP (acoustic Doppler current profiler) and DVL (Doppler velocity log) respectively. The AUV dynamic model that represented the Gavia AUV behaviour was developed. For the AUV dynamic model, hydrodynamics parameters were identified by applying real-time system identification utilising the RLS identification method. The Recursive Least Squares (RLS) identification technique was used as it has the advantages of simple calculation and good convergence properties. The real-time model identification algorithm allowed the AUV model to be continuously updated in response to the operational environment.

The HGO was used as a nonlinear estimation algorithm to obtain the vehicle velocities through the water. Stability of the estimation error dynamics was investigated via the Lyapunov function. During the AUV simulation, the vehicle velocities through the water were obtained by applying the equivalent control commands which were executed during the field test. Once the vehicle velocities through the water were available, the current velocities were calculated by subtracting the vehicle velocities through the water from the vehicle velocities over the ground recorded by the DVL-aided INS. The estimated current velocities were found to be well matched with the measured current from the AUV-onboard ADCP.

A path following control method for an AUV using the HGO based on a dynamic model was investigated. The control objective of the path following was to ensure the vehicle followed a given desired path and maintain a desired constant relative surge velocity. The update law and guidance law were utilised to provide pitch and yaw references to the controllers, so that the AUV could follow the desired path described by the Serret-Frenet frame. In order to study the effectiveness of the HGO using the LMI approach, estimation errors from both the HGO and the state observer using the pole placement (PP) approach were quantitatively analysed (Chapter 4).

Finally, the performance of the proposed path-following guidance system, ‘PPNAPG (Pure Proportional Navigation and Pursuit Guidance)’ was validated via both simulation and experiment using the MUN (Memorial University of Newfoundland) Explorer AUV. The proposed guidance system combines the pure proportional navigation guidance (PPNG) law and pursuit guidance (PG) law.

First of all, the MUN Explorer AUV’s dynamic model was built by using the component build-up method, and the model was validated by utilising data from sea trials. The AUV track from the simulation were closely matched with the AUV’s actual track within a thin margin of discrepancy at the turning point of the waypoints. The performance of the PPNAPG guidance system was quantitatively validated by analysing the cross-track error compared with the counterparts from the experiment. The EKF was applied to estimate the current velocity by using measurements from GPS, rpm and heading angle (Chapter 5).

6.2 Findings

The major findings of the research are listed below.

6.2.1 Current estimation using nonlinear observers

- In order to quantify the differences between the estimated current by the HGO and measured current velocities by ADCP, standard deviations were calculated. Furthermore, the current estimation results from the AUV model-based observer were also compared with the estimation results from the WVAM (water velocity components of a turbulent water column using the AUV motion response). While the estimation error from using the WVAM was 1.283%, the counter part from using the HGO was 1.222% which resulted in an estimation improvement of 5% (Chapter 2).

- The estimated current velocities by using the HGO were well matched with the actual current velocities. In order to verify the improvement of the HGO using the LMI, the estimation error means for the HGO using the LMI as well as the pole placement approach were quantitatively analysed. While the estimation error mean for the HGO using the pole placement had 1.1219 %, the counter part of the HGO using the LMI had 0.6217 % which contributed an estimation improvement of 44.92 % (Chapter 3).
- The standard deviations of the estimated current velocity by the HGO lay within the uncertainty margin of the ADCP which was $\pm$ 0.1 m/s for both simulation cases (Chapter 4).
- The estimated current velocities were compared with the current measurement from a TriAXYS ADCP buoy, which validated that the EKF can estimate current velocities in x and y axes with a standard deviation around 0.483 and 0.488 respectively (Chapter 5).

6.2.2 AUV path following guidance system

- For the path following study, the desired curved path was represented by using a Serret-Frenet frame which propagated along the curve. Two path-following cases consisting of a straight-line and a helix path were simulated to validate the performance of the proposed control system. Both cases have shown that the AUV reached and converged to the desired path with in 50 and 100 seconds of transient period respectively. (Chapter 4).
- The HGO exhibits more accurate and robust path following performance and stability with smaller path error (0.0094) than the state observer using the pole placement method (0.00245) which contributed for 62% error reduction (Chapter 4).
- The PPNAPG allowed the vehicle to pass the waypoint with shorter time than the conventional LOS guidance law, which resulted in 11% reduction in the time compared with the time taken in the experiment (Chapter 5).
- The cross-track error mean and standard deviation for the simulation using the PP-NAPG was 0.76 and 1.15 while the counter parts using the conventional LOS was 0.91 and 1.85, which means that the PPNAPG exhibited better path following accuracy and stability with smaller average and standard deviation of cross-track error than the conventional LOS guidance system (Chapter 5).

6.2.3 AUV dynamic model identification

- For the AUV dynamic model, the real-time system identification utilising the RLS (Recursive Least Squares) identification method was able to determine hydrodynamics parameters (Chapter 2).
- In highly dynamic environments, the parameters of the mathematical model fluctuate with time due to environmental forces. Therefore, in this study, a real-time model identification algorithm was utilised to identify the dynamics parameters with continuous updates, which allowed the AUV model to produce the vehicle's motion response in the present environment (Chapter 2).
- The AUV's dynamic model was able to represent the forces and moments that are not captured by the kinematic motion model. Thus, the HGO based on the dynamic model has the potential to improve the performance of the path following problem and current estimation (Chapter 4).
- The MUN Explorer AUV's dynamic model was built by using the 'component build-up method', and the model was validated by utilising data from sea trials. The AUV track from the simulation were closely matched with the AUV's actual track within a thin margin of discrepancy at the turning point of the waypoints (Chapter 5).

6.3 Conclusions

In this study, it was shown that the nonlinear observers, the high-gain observer (HGO) and the Extended Kalman filter (EKF) methods, can estimate the ocean current velocity based on the AUV's dynamic model representing the force and moments that are not captured by the kinematic motion model. The AUV's dynamic models established by the 'component build-up method' and system identification utilising the RLS contributed to improve the performance of the path following problems as well.

In terms of the guidance system, the proposed PPNAPG allowed the vehicle to follow a desired path without overshoot, which reduced the time to reach the last waypoint.

Overall, these results suggest that the nonlinear observers based on an AUV dynamic model and the PPNAPG is an effective combination to estimate and compensate for the current and complete a path-following mission. These outcomes and methods enable other researchers and students in the field of AUV control and navigation systems to adapt and extend the methods to other AUV models without using an ADCP to measure the current. The insight gained from this study can also be of assistance to an oceanographic mission by optimising the guidance law to reduce mission completion time.

6.4 Limitation and Future Work

Based on limitations in this study, the following future work is recommended for the continuance of this research program.

- The HGO which was used to estimate the current velocity in this study is based on the idea of selecting a sufficiently large gain in such a way as to dominate the nonlinear contribution to the dynamics of the estimation error. Unfortunately, such a large gain is the source of the well-known peaking phenomenon, which may introduce destabilization into the loop. In order to reduce peaking, a time- varying observer can be suggested with the structure of the standard high-gain observer, but with the possibility to assign a small gain in the first-time instants and then increases over time up to the point of maximum.
- Time varying and nonuniform currents are considered important, but animation was required to simulate time-varying current states. However the process to create an animated line simulator for time-varying states is computationally expensive. In this thesis, only nonuniform currents were considered due to limited resources and time scheduling, so it is suggested in future to study current estimations using the HGO which considers both nonuniform and time-varying currents.
- Since applying the covariance matching technique is beyond the research scope, the standard deviations for the noise covariance matrices were estimated based on typical error bounds associated with the process, measurement. Therefore, it is suggested to apply the covariance matching technique in which the estimates of the process noise covariance (Q) and measurement noise covariance (R) are computed at every sampling instant.
- The RLS algorithm was used to identify the nonlinear parameters of the AUV model using an offline analysis. However, the dynamic characteristics of an AUV is affected when it is reconfigured with different payloads. It is desirable to have an updated model, such that the control and guidance law can be redesigned to obtain better performance. Hence, it is recommended to establish an online identification of AUV dynamics via in-field experiments, which enable the operator to obtain an updated dynamic model whenever there is a change in payload configuration or vehicle geometry.
- The real ocean environment is harsher and more complex than considered in the simulations here, and this may result in more serious parameter perturbations, model

uncertainties, and external disturbances than considered in this study. Therefore, a study of the adaptability of the proposed PPNAPG is suggested to conduct further verification in the real ocean environment.

Appendix A

MUN Explorer AUV Modelling

A.1 Kinematics

An underwater vehicle moving in 3D space has six degrees of freedom (DOF), so six coordinates are necessary to determine the position and orientation of the vehicle as indicated in Figure A.1. The moving coordinate frame **XYZ** is conveniently fixed to the vehicle and is called the body-fixed reference frame. The origin **O** of the body-fixed frame is chosen to coincide with the centre of gravity(CG).

The motion of the body-fixed frame is described relative to an Earth-fixed reference frame. The position and orientation of the vehicle should be described relative to the inertial reference frame while the linear and angular velocities of the vehicle should be expressed in the body-fixed coordinate system [79]. The six different motion components are conveniently defined as : *surge*, *sway*, *heave*, *roll*, *pitch* and *yaw*, see Table A.1.

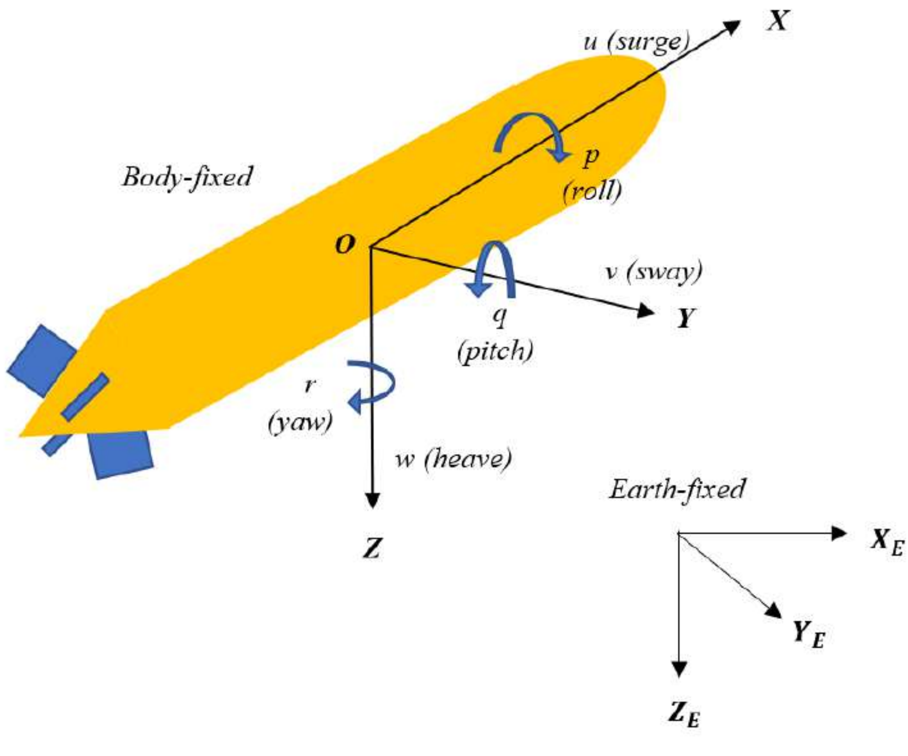

Figure A.1: AUV's body-fixed and Earth-fixed reference frames.

Table A.1: Notation used for marine vehicle

Degree-of Freedom		Force and moments	Linear and angular vel	Position and Euler angles
1	Motion in the x -direction (surge)	X	u	x
2	Motion in the y -direction (sway)	Y	v	y
3	Motion in the z-direction (heave)	Z	w	z
4	Motion in the x-direction (roll)	K	p	ϕ
5	Motion in the y-direction (pitch)	M	q	θ
6	Motion in the z-direction (yaw)	N	r	ψ

Based on the notation in Table A.1, the general motion of the vehicle in 6 DOF can be described by the following vectors:

$$\begin{aligned}
\boldsymbol{\eta} &= [\boldsymbol{\eta}_1^T, \boldsymbol{\eta}_2^T]^T; & \boldsymbol{\eta}_1 &= [x, y, z]^T; & \boldsymbol{\eta}_2 &= [\phi, \theta, \psi]^T \\
\boldsymbol{\nu} &= [\boldsymbol{\nu}_1^T, \boldsymbol{\nu}_2^T]^T; & \boldsymbol{\nu}_1 &= [u, v, w]^T; & \boldsymbol{\nu}_2 &= [p, q, r]^T \\
\boldsymbol{\tau} &= [\boldsymbol{\tau}_1^T, \boldsymbol{\tau}_2^T]^T; & \boldsymbol{\tau}_1 &= [X, Y, Z]^T; & \boldsymbol{\tau}_2 &= [K, M, N]^T
\end{aligned}$$

Here $\boldsymbol{\eta}$ is the position and orientation vector with coordinates in the inertial frame, $\boldsymbol{\nu}$ denotes the linear and angular velocity vector with coordinates in the body-fixed frame. $\boldsymbol{\tau}$ describes the forces and moments acting on the vehicle in the body-fixed frame.

The vehicle's trajectory relative to the inertial coordinate system is given by a velocity transformation :

$$\dot{\boldsymbol{\eta}}_1 = \boldsymbol{J}_1(\boldsymbol{\eta}_2)\boldsymbol{\nu}_1 \tag{A.1}$$

$\boldsymbol{J}_1(\boldsymbol{\eta}_2)$ is a transformation matrix which is related through the functions of the Euler angles : roll(ϕ), pitch(θ) and yaw(ψ) as de shown below :

$$\boldsymbol{J}_1(\boldsymbol{\eta}_2) = \begin{bmatrix} c\theta c\psi & -c\phi s\psi + s\phi s\theta c\psi & s\phi s\psi + c\phi s\theta c\psi \\ c\theta s\psi & -c\phi c\psi + s\phi s\theta s\psi & -s\phi c\psi + c\phi s\theta s\psi \\ -s\theta & c\theta s\phi & c\theta c\phi \end{bmatrix} \tag{A.2}$$

where $s\cdot = \sin(\cdot)$ and $c\cdot = \cos(\cdot)$.

The body-fixed angular velocity vector $\boldsymbol{\nu}_2 = [p, q, r]^T$ and the Euler rater vector $\dot{\boldsymbol{\eta}}_2 = [\dot{\phi}, \dot{\theta}, \dot{\psi}]^T$ are related through a transformation matrix $\boldsymbol{J}_2(\boldsymbol{\eta}_2)$ according to :

$$\dot{\boldsymbol{\eta}}_2 = \boldsymbol{J}_2(\boldsymbol{\eta}_2)\boldsymbol{\nu}_2 \tag{A.3}$$

where

$$\boldsymbol{J}_2(\boldsymbol{\eta}_2) = \begin{bmatrix} 1 & s\phi t\theta & c\phi t\theta \\ 0 & c\phi & -s\phi \\ 0 & s\phi / c\theta & c\phi / c\theta \end{bmatrix}.$$

Therefore, the kinematic equation A.1 and A.2 can be expressed in vector form as :

$$\begin{bmatrix} \dot{\boldsymbol{\eta}}_1 \\ \dot{\boldsymbol{\eta}}_2 \end{bmatrix} = \begin{bmatrix} \boldsymbol{J}_1(\boldsymbol{\eta}_2) & \boldsymbol{0}_{3\times3} \\ \boldsymbol{0}_{3\times3} & \boldsymbol{J}_2(\boldsymbol{\eta}_2) \end{bmatrix} \begin{bmatrix} \boldsymbol{\nu}_1 \\ \boldsymbol{\nu}_2 \end{bmatrix} \quad \Longleftrightarrow \quad \dot{\boldsymbol{\eta}} = \boldsymbol{J}(\boldsymbol{\eta})\boldsymbol{\nu} \tag{A.4}$$

A.2 Rigid Body Dynamics

The coordinate of the vehicle's centres of gravity and buoyancy are defined in terms of the body-fixed coordinate system as in the following equation and the values are in Table A.2:

$$\boldsymbol{r}_g = \begin{bmatrix} x_g \\ y_g \\ z_g \end{bmatrix} \qquad \boldsymbol{r}_b = \begin{bmatrix} x_b \\ y_b \\ z_b \end{bmatrix}$$

Table A.2: Centre of Gravity and Buoyancy

Parameter	Value	Units
x_G	-1.87337e-01	m
y_G	0	m
z_G	7.53006e-03	m
x_B	-1.87337e-01	m
y_B	0	m
z_B	-1.38144e-03	m

The equations of motion for a rigid body in six degrees of freedom are represented as follows:

$$\begin{aligned}
m[\dot{u} - vr + wq - x_G(q^2+r^2) + y_G(pq - \dot{r}) + z_G(pr + \dot{q})] &= \Sigma X_{ext} \\
m[\dot{v} - wp + ur - y_G(r^2+p^2) + z_G(qr - \dot{p}) + x_G(qp + \dot{r})] &= \Sigma Y_{ext} \\
m[\dot{w} - uq + vq - z_G(p^2+q^2) + x_G(rp - \dot{q}) + y_G(rq + \dot{p})] &= \Sigma Z_{ext} \\
I_x\dot{p} + (I_z - I_y)qr - (\dot{r} + pq)I_{xz} + (r^2 - q^2)I_{yz} + (pr - \dot{q})I_{xy} & \\
+m[y_G(\dot{w} - uq + vp) - z_G(\dot{v} - wp + ur)] &= \Sigma K_{ext} \qquad \text{(A.5)} \\
I_y\dot{q} + (I_x - I_z)rp - (\dot{p} + qr)I_{xy} + (p^2 - r^2)I_{zx} + (qp - \dot{r})I_{yz} & \\
+m[z_G(\dot{u} - vr + wq) - x_G(\dot{w} - uq + vp)] &= \Sigma M_{ext} \\
I_z\dot{r} + (I_y - I_x)pq - (\dot{q} + rp)I_{yz} + (q^2 - p^2)I_{xy} + (rq - \dot{p})I_{zx} & \\
+m[x_G(\dot{v} - wp + ur) - y_G(\dot{u} - vr + wq)] &= \Sigma N_{ext}
\end{aligned}$$

where m is the vehicle mass. The first three equations in Equation A.5 represent the translational motion while the last three equations represent the rotational motion. The value of m and the *MUN Explorer* AUV's moments of inertia are tabulated in Table A.3. Equation A.5 can be expressed in a more compact form as:

$$\boldsymbol{M}_{RB}\dot{\boldsymbol{\nu}} + \boldsymbol{C}_{RB}(\boldsymbol{\nu})\boldsymbol{\nu} = \boldsymbol{\tau}_{RB} \qquad \text{(A.6)}$$

where $\boldsymbol{M}_{RB}$ is the parametrization of the rigid-body inertia matrix; $\boldsymbol{C}_{RB}(\nu)$ is the rigid-body Coriolis and centripetal matrix; $\boldsymbol{\nu}$ is the velocity vector (i.e., $[u\ v\ w\ p\ q\ r]$ where p,q and

r are the angular velocities around the x,y and z axes) and $\boldsymbol{\tau}_{RB}$ is a generalised vector of external forces and moments:

$$\boldsymbol{\tau}_{RB} = [\Sigma X_{ext}, \Sigma Y_{ext}, \Sigma Z_{ext}, \Sigma K_{ext}, \Sigma M_{ext}, \Sigma N_{ext}]$$

Table A.3: Vehicle Mass and Moment of Inertia [75]

Parameter	Value	Units	Description
m	1432.7	kg	Vehicle mass
I_x	1.708+e01	kg m^2	Moment of Inertia
I_y	1.88171+e03	kg m^2	Moment of Inertia
I_z	1.87719+e03	kg m^2	Moment of Inertia
I_{xz}	-3.09+e00	kg m^2	Moment of Inertia
I_{yz}	-2.90-e01	kg m^2	Moment of Inertia
I_{xy}	-9.80-e01	kg m^2	Moment of Inertia

A.3 Restoring Forces and Moments

The weight of the *MUN Explorer* AUV can be different between missions depending on the payload sensors and the amount of ballast. The weight and buoyancy used in this study were referenced from [75] and are shown in Table A.4.

Table A.4: Vehicle Weight and Buoyancy

Parameter	Value	Units	
W	1.4055e+04	N	Vehicle Weight
B	1.4041e+04	N	Vehicle Buoyancy

In order to express the weight and buoyancy force in terms of the body-fixed frame, the transformation matrix was used as below:

$$\begin{aligned} \boldsymbol{f}_G(\boldsymbol{\eta}_2) &= \boldsymbol{J}_1^{-1}(\boldsymbol{\eta}_2)\begin{bmatrix}0\\0\\W\end{bmatrix} \\ \boldsymbol{f}_B(\boldsymbol{\eta}_2) &= -\boldsymbol{J}_1^{-1}(\boldsymbol{\eta}_2)\begin{bmatrix}0\\0\\B\end{bmatrix} \end{aligned} \tag{A.7}$$

where $\boldsymbol{J}_1(\boldsymbol{\eta}_2)$ is the Euler angle coordinates transformation matrix defined in Equation A.2. Consequently, the restoring force and moment vector can be expressed in the body-fixed coordinate system as :

$$\boldsymbol{g}(\boldsymbol{\eta}_2) = -\begin{bmatrix}\boldsymbol{f}_G(\boldsymbol{\eta}_2) + \boldsymbol{f}_B(\boldsymbol{\eta}_2)\\ \boldsymbol{r}_G \times \boldsymbol{f}_G(\boldsymbol{\eta}_2) + \boldsymbol{r}_B \times \boldsymbol{f}_B(\boldsymbol{\eta}_2)\end{bmatrix} \tag{A.8}$$

Expanding Equation A.9 yields:

$$\boldsymbol{g}(\boldsymbol{\eta}_2) = \begin{bmatrix} (W-B)\sin\theta \\ -(W-B)\cos\theta\sin\phi \\ -(W-B)\cos\theta\cos\phi \\ -(y_GW - y_BB)\cos\theta\cos\phi + (z_GW - z_BB)\cos\theta\sin\phi \\ (z_GW - z_BB)\sin\theta + (x_GW - x_BB)\cos\theta\cos\phi \\ -(x_GW - x_BB)\cos\theta\sin\phi - (y_GW - y_BB)\sin\theta \end{bmatrix} \tag{A.9}$$

A.4 Hydrodynamic Damping

1. Axial Drag

The parameters of the *MUN Explorer* AUV including the diameter and frontal area, A_f are tabulated in Table A.4 while c_d was given from the AUV manufacturer, ISE (International Submarine Engineering Ltd.).

Table A.5: Centre of Gravity and Buoyancy

Parameter	Value	Units	Description
ρ	1.025	kg/m^3	Seawater Density
d	0.69	m	Maximum Hull Diameter
A_f	0.3739	m^2	Hull Frontal Area
c_d	0.252255	n/a	Axial Drag Coefficient

The nonlinear cross-flow drag coefficients were calculated by the flowing equation:

$$\begin{aligned}
Y_{v|v|} &= -\frac{1}{2}\rho c_{y\beta}\int_{x_1}^{x_2} 2R(x)dx \\
Z_{w|w|} &= -\frac{1}{2}\rho c_{z\alpha}\int_{x_1}^{x_2} 2R(x)dx \\
M_{w|w|} &= \frac{1}{2}\rho c_{m\alpha}\int_{x_1}^{x_2} 2xR(x)dx \\
N_{v|v|} &= -\frac{1}{2}\rho c_{n\beta}\int_{x_1}^{x_2} 2xR(x)dx \\
Y_{r|r|} &= -\frac{1}{2}\rho c_{yr}\int_{x_1}^{x_2} 2x|x|R(x)dx \\
Z_{q|q|} &= \frac{1}{2}\rho c_{zq}\int_{x_1}^{x_2} 2x|x|R(x)dx \\
M_{q|q|} &= -\frac{1}{2}\rho c_{mq}\int_{x_1}^{x_2} 2x^3R(x)dx \\
N_{r|r|} &= \frac{1}{2}\rho c_{nr}\int_{x_1}^{x_2} 2x^3R(x)dx
\end{aligned} \tag{A.10}$$

where $c_\star$ are the drag coefficients as tabulated in Table A.6, and $R(x)$ is the hull radius as a function of axial position. See Table A.7 and Figure A.2 for the limits of integration and the vehicle's geometric parameters.

Table A.6: Cross-flow Drag Coefficients

Parameter	Value	Units	Description
$c_{y\beta}$	-3.26011	n/a	Cross-flow Drag Coefficient
$c_{z\alpha}$	-3.96196	n/a	Cross-flow Drag Coefficient
$c_{m\alpha}$	0.20773	n/a	Cross-flow Drag Coefficient
$c_{n\beta}$	0.102575	n/a	Cross-flow Drag Coefficient
c_{yr}	-0.555803	n/a	Cross-flow Drag Coefficient
c_{zq}	0.818787	n/a	Cross-flow Drag Coefficient
c_{mq}	-0.591503	n/a	Cross-flow Drag Coefficient
c_{nr}	-0.647825	n/a	Cross-flow Drag Coefficient

Table A.7: *NUM Explorer* Geometric Parameters

Parameter	Value	Units	Description
l_1	0.69	m	Length of nose cone
l_2	1.3208	m	Length of forward payload section
l_3	0.9906	m	Length of faired tail section
l_4	0.2921	m	Length of tail con section
d	0.69	m	Maximum Hull Diameter
ω	4.36	radians	Included tail angle
x_1	-2.4170	m	Hull coordinate for aft end of tail section
x_2	+2.083	m	Hull coordinate for fwd end of bow section
x	$x_1 \leq x \leq x_2$	m	Axial position x
$R(x)$	$0 < R(x) \leq d$	m	Hull radius as a function of axial position x

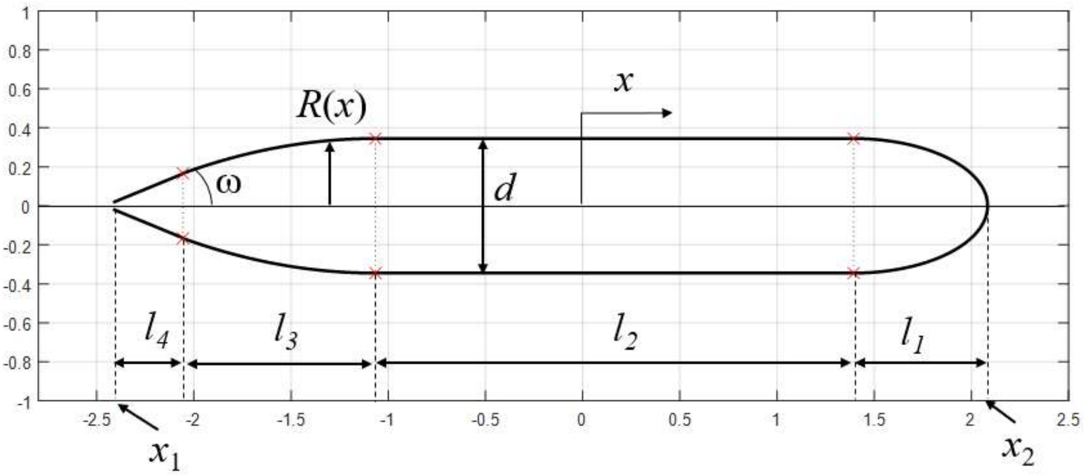

Figure A.2: *MUN Explorer* AUV Profile : vehicle hull radius as a function of axial position.

A.5 Added Mass

Added mass matrix for the *MUN Explorer* AUV with its 'X' tail configuration was expressed as:

$$\boldsymbol{M}_A = \begin{bmatrix} X_{\dot{u}} & X_{\dot{w}} & X_{\dot{w}} & X_{\dot{p}} & X_{\dot{q}} & X_{\dot{r}} \\ Y_{\dot{u}} & Y_{\dot{w}} & Y_{\dot{w}} & Y_{\dot{p}} & Y_{\dot{q}} & Y_{\dot{r}} \\ Z_{\dot{u}} & Z_{\dot{w}} & Z_{\dot{w}} & Z_{\dot{p}} & Z_{\dot{q}} & Z_{\dot{r}} \\ K_{\dot{u}} & K_{\dot{w}} & K_{\dot{w}} & K_{\dot{p}} & K_{\dot{q}} & K_{\dot{r}} \\ M_{\dot{u}} & M_{\dot{w}} & M_{\dot{w}} & M_{\dot{p}} & M_{\dot{q}} & M_{\dot{r}} \\ N_{\dot{u}} & N_{\dot{w}} & N_{\dot{w}} & N_{\dot{p}} & N_{\dot{q}} & N_{\dot{r}} \end{bmatrix}$$

$$= \begin{bmatrix} -15.6 & 0.0 & 0.1 & 0.1 & 0.5 & 0.0 \\ 0.0 & -4.8.2 & 0.0 & -8.2 & 0.0 & 102.1 \\ 0.1 & 0.0 & -468.2 & 0.0 & -66.8 & 0.0 \\ 0.0 & -8.2 & 0.0 & -43.9 & 0.0 & 3.7 \\ 0.5 & 0.0 & -66.8 & 0.0 & -555.7 & 0.0 \\ 0.0 & 102.1 & 0.0 & 3.7 & 0.0 & -549.8 \end{bmatrix} \tag{A.11}$$

$$Units : \begin{bmatrix} kg & kg & kg & kg \cdot m & kg \cdot m & kg \cdot m \\ kg & kg & kg & kg \cdot m & kg \cdot m & kg \cdot m \\ kg & kg & kg & kg \cdot m & kg \cdot m & kg \cdot m \\ kg \cdot m & kg \cdot m & kg \cdot m & kg \cdot m^2 & kg \cdot m^2 & kg \cdot m^2 \\ kg \cdot m & kg \cdot m & kg \cdot m & kg \cdot m^2 & kg \cdot m^2 & kg \cdot m^2 \\ kg \cdot m & kg \cdot m & kg \cdot m & kg \cdot m^2 & kg \cdot m^2 & kg \cdot m^2 \end{bmatrix}$$

The hydrodynamic Coriolis and Centripetal matrix $\boldsymbol{C}_A(\boldsymbol{\nu})$ can be defined as followed:

$$\boldsymbol{C}_A(\boldsymbol{\nu}) = \begin{bmatrix} \boldsymbol{0}_{3\times 3} & -\boldsymbol{S}(A_{11}\nu_1 + A_{12}\nu_2) \\ -\boldsymbol{S}(A_{21}\nu_1 + A_{12}\nu_2) & -\boldsymbol{S}(A_{21}\nu_1 + A_{22}\nu_2) \end{bmatrix} \tag{A.12}$$

where the matrix $\boldsymbol{S}(\lambda)$ which is skew-symmetrical and A_{ij} $(i, j = 1, 2)$ are be represented as:

$$\boldsymbol{S}(\lambda) = \begin{bmatrix} 0 & -\lambda_3 & \lambda_2 \\ \lambda_3 & 0 & -\lambda_1 \\ -\lambda_2 & \lambda_1 & 0 \end{bmatrix}$$

$$\boldsymbol{M}_A = \begin{bmatrix} A_{11} & A_{12} \\ A_{21} & A_{22} \end{bmatrix}$$

A.6 *MUN Explorer* AUV's Control Planes

The *MUN Explorer* has six planes for manoeuvring as illustrated in Figure A.3. According to the numbering in the manufacturer's manual, the two bow planes are numbered 1 and 2 while the stern planes are 3 and 4 on the port side and 5 and 6 on the starboard side. The two forward planes control the depth. The x-configuration rudders, which are staggered at 45 degrees from the '+' configuration, will couple roll, pitch and yaw control into all four planes. The aft 'x' plane's configuration has been found to be best for the *MUN Explorer* AUV as it provides optimal stability, redundancy and limited protrusion [82].

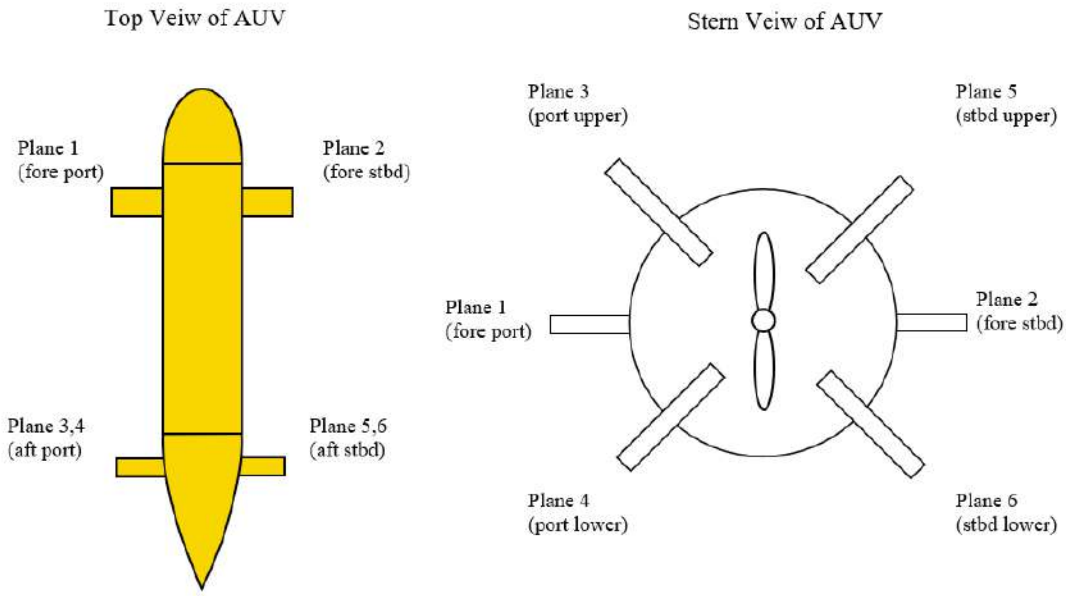

Figure A.3: *MUN Explorer* Control Plane numbering

A sign for the plane's deflection complies with the "right hand rule" as illustrated in Figure A.4: positive direction is indicated by the curl of the fingers when the right thumb points away from the central axis of the AUV.

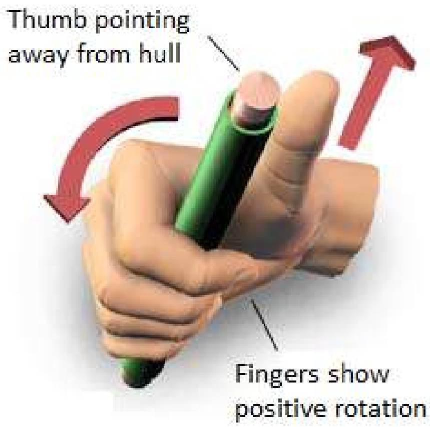

Figure A.4: Right hand rule for planes

The planes have a symmetrical cross-section of NACA 0024 [83] whose profile is illustrated in Figure A.4 [101]. The *MUN explorer* AUV's control planes have an aspect ratio of 1; values for the plane's chord, span and thickness are tabulated in Table A.8 [72].

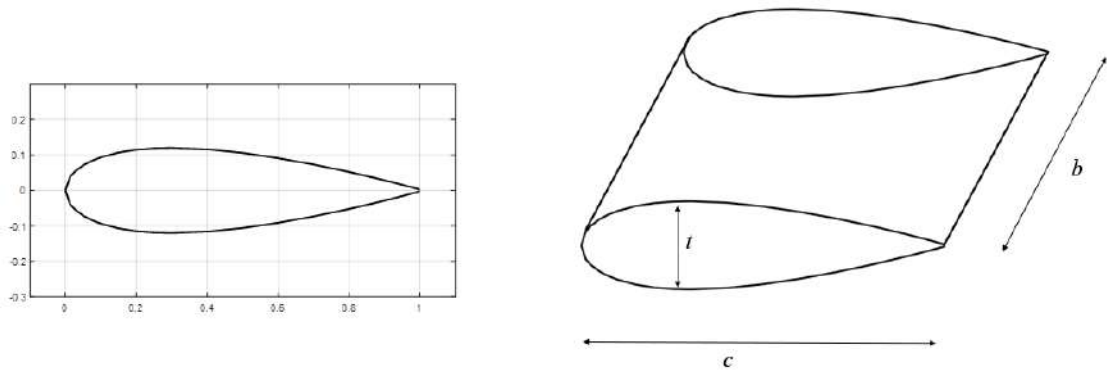

Figure A.5: NACA 0024 Profile(Left) and dimension of control plane of *MUN Explorer* AUV

Table A.8: *MUN Explorer* Control Plane Geometric Parameters

Parameter	Value	Units	Description
c	0.36	m	Chord Length
b	0.36	m	Span Length
t	0.085	m	Maximum thickness

A.7 Dynamics of Control Planes

1. Fore planes

The depth of the vehicle is controlled by two fore horizontal planes. For the fore control planes, the empirical formula for the lift is given as :

$$\begin{aligned} L_{plane} &= -\frac{1}{2}\rho c_L S_{plane}\delta_e v_e^2 \\ M_{plane} &= x_{plane} L_{plane} \end{aligned} \tag{A.13}$$

where c_L is the fin lift coefficient, S_{plane} the planform area, δ_e the effective plane angle in radians, v_e the effective plane velocity, and x_{plane} the axial position of the plane post in the body-referenced coordinates.

The lift and drag coefficients for an NACA 0024 airfoil section are about the same as for an NACA 0025 airfoil section, for which extensive experimental research has been performed and reported in [102]. The NACA tests were conducted for airfoils of aspect ratio (AR) 6, but the *MUN Explorer* has planes of 1 AR. By applying the formulae from [103], the drag, lift and moment coefficients for NACA 0025 with AR = 1 were calculated as shown in Figure A.6.

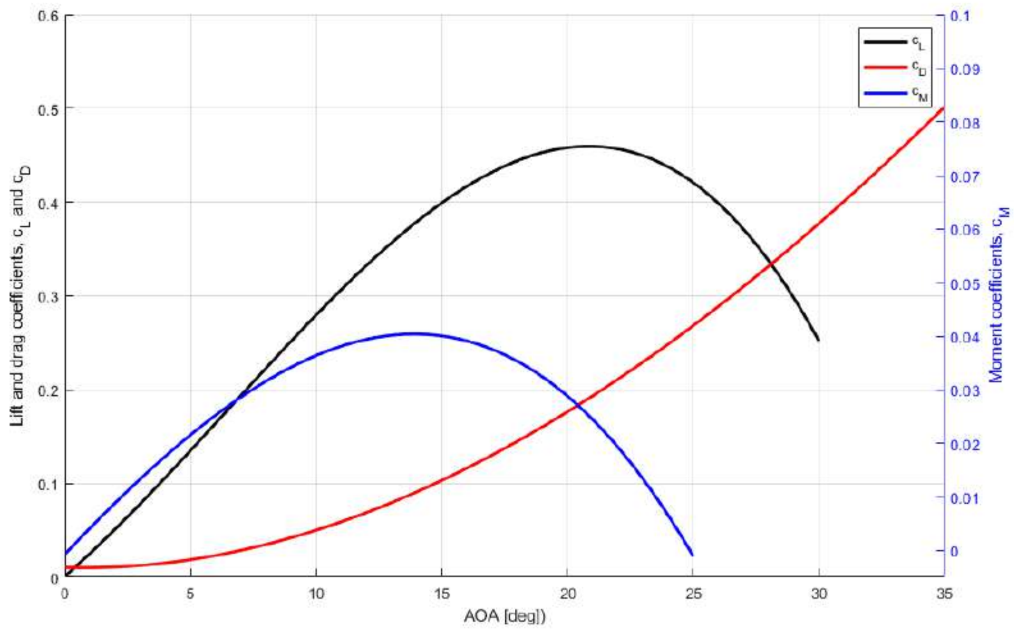

Figure A.6: Lift, drag and pitching moment coefficients for the control planes; NACA 0025 airfoils corrected for AR = 1

As the fore planes are located at a certain offset from the origin of the vehicle coordinate system, the effective velocity was used as:

$$\begin{aligned} u_{plane} &= u + z_{plane}q - y_{plane}r \\ v_{plane} &= v + x_{plane}r - z_{plane}p \\ w_{plane} &= w + y_{plane}p - x_{plane}q \end{aligned} \tag{A.14}$$

where x_{plane}, y_{plane} and z_{plane} are the coordinates of the fore planes' post in the body-referenced frame, but y_{plane} and z_{plane} terms are dropped due to their small values. The coordinates of the fore and aft planes' post are illustrated in Figure A.7 and tabulated in Table A.9.

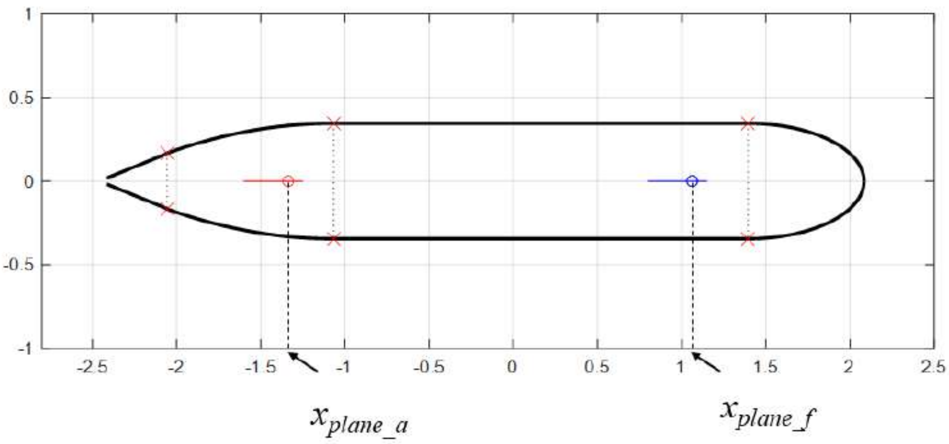

Figure A.7: Coordinates of the post for the planes

Table A.9: *NUM Explorer* Coordinate of the planes post

Parameter	Value	Units	Description
x_{plane_a}	-1.25	m	Body-referenced coordinate of the aft plane post
x_{plane_f}	+1.15	m	Body-referenced coordinate of the fore plane post

The effective plane angles was expressed as:

$$\delta_e = \delta + \beta_e \tag{A.15}$$

where δ is the plane angle, β_e the effective angles of attack as shown in Figure A.8. Based on the Equation A.14, the effective angles of attack can be expressed as:

$$\beta_e = \frac{w_{plane}}{u_{plane}} \approx \frac{1}{u}(w - x_{plane}q) \tag{A.16}$$

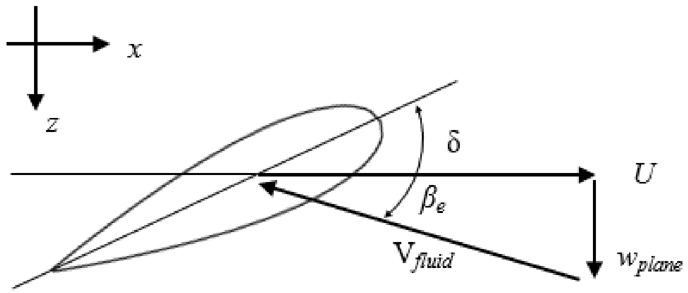

Figure A.8: Effective angle of attack for fore planes.

Substituting Equations A.14, A.15 and A.16 into Equation A.13 results in the following equations for fore plane lift and moment:

$$\begin{aligned} Z_{p1} &= -\frac{1}{2}\rho c_L S_{plane}[u_2\delta + uw - x_{plane_f}(uq)] \\ M_{p1} &= \frac{1}{2}\rho c_L S_{plane} x_{plane_f}[u_2\delta + uw - x_{plane}(uq)] \end{aligned} \tag{A.17}$$

2. Aft 'x'-configuration planes

The view of the aft control planes looking behind is shown in Figure A.9 where u,v r are the vehicle's surge, sway velocity and yaw rate. The angle between the axis of rotation for each stern-plane and the horizontal is called the X-angle which was designed as $\xi = 45$ degree. As mentioned in Equation A.14, the effective velocity was used as:

$$v_{plane} = v + x_{plane} r \tag{A.18}$$

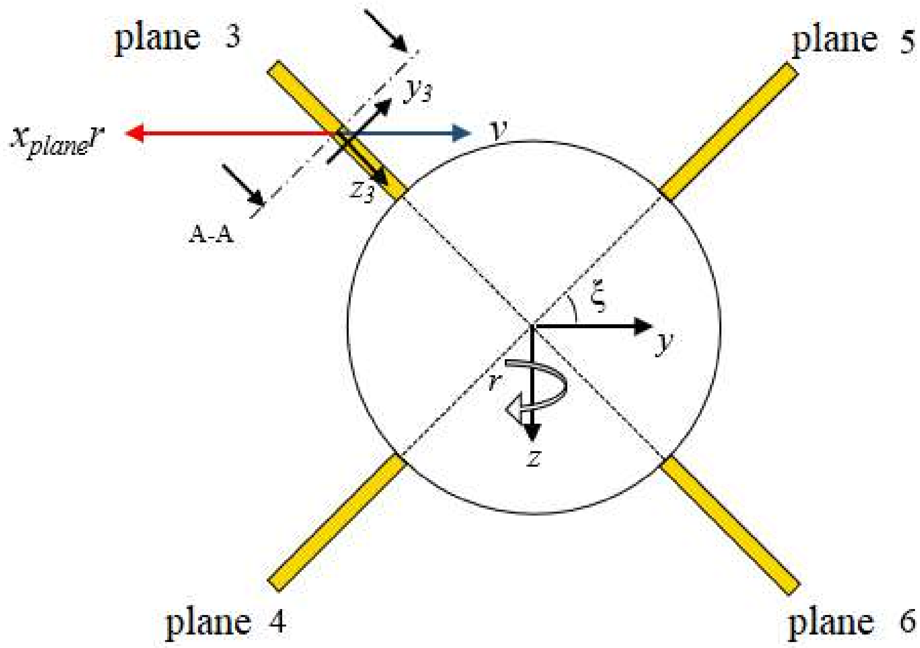

Figure A.9: Rare view of the 'X' configuration control planes.

The top view of plane 3 cut by the line A-A in Figure A.9 is shown in Figure A.10 with the plane deflection δ. The effective lateral velocity of the plane shown in Equation A.18 was corrected for the X-angle, ξ, as:

$$v'_{plane} = (v + x_{plane}r)\sin(\xi) \tag{A.19}$$

As illustrated in Figure A.10 (b), the angle between the plane 3 and the flow can be expressed as:

$$\beta_e = \frac{-v_{plane}}{u} \tag{A.20}$$

The effective angle for the plane 3 is expressed as :

$$\delta_e = \delta + \beta_e \tag{A.21}$$

where δ is the plane 3 angle, β_e the effective angles of attack as shown in Figure A.10 (a). Based on Equation A.14, the effective angles of attack can be express as:

$$\beta_e = \frac{v'_{plane}}{u_{plane}} \approx \frac{1}{u}(v + x_{plane}r) \tag{A.22}$$

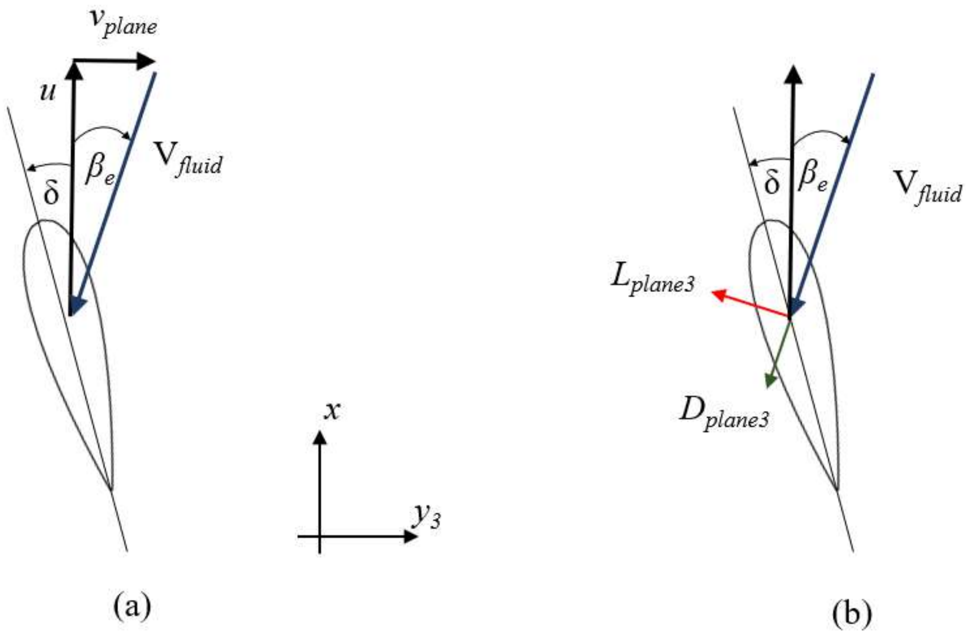

Figure A.10: Top view of plane 3 : (a) the perpendicular cut A-A in Figure A.6, (b) the resultant inflow velocity and drag angle.

As the direction of the plane deflection is equal for all four aft planes, the equation of effective angle shown in Equation A.22 can be applied for Plane 3 to plane 6. In order to calculate the net axial force and sway force generated by the control planes, the drag and lift forces shown in Figure A.10 (b) should be projected along the xy-axis of the vehicle coordinate system. The sway force generated by the plane 3 along y_3 axis can be expressed as:

$$F'_{y,plane3} = L_{plane3}\cos(\beta_e) + D_{plane3}\sin(\beta_e) \tag{A.23}$$

Therefore, the net sway force produced by the four aft planes was obtained by summing each sway forces from each planes using Equation A.23:

$$F'_{y,planes} = F'_{y,plane3} + F'_{y,plane4} + F'_{y,plane5} + F'_{y,plane6} \tag{A.24}$$

The net sway force in Equation A.24 should be corrected for the X-angle as:

$$\begin{aligned} F_{y,planes} &= F'_{y,planes}\sin(\xi) \\ &= [F'_{y,plane3} + F'_{y,plane4} + F'_{y,plane5} + F'_{y,plane6}]\sin(\xi) \\ &= [(L_{plane3} + L_{plane4} + L_{plane5} + L_{plane6})\cos(\beta_e) \\ &\quad + (D_{plane3} + D_{plane4} + D_{plane5} + D_{plane6})\sin(\beta_e)]\sin(\xi) \end{aligned} \tag{A.25}$$

A.8 Propulsion Model

The *MUN Explorer* AUV is propelled by a high-efficiency two-blade propeller with diameter 0.65m which enables the vehicle to reach a maximum speed of 2.5 m/s. A first-order approximation of the developed thrust T and torque Q for a propeller can be derived from lift force calculations (see [104]). Let n denote the propeller revolutions, D is the propeller diameter, ρ the water density and V_a the advanced speed at the propeller (speed of the water going into the propeller). Hence the following expressions for the propeller thrust can be established:

$$T = \rho D^4 K_T(J_0)|n|n \tag{A.26}$$

where $J_0 = V_a/(nD)$ is the advance number and k_T is the thrust coefficient as shown in Figure A.11. The advance speed V_a is related through the speed of the vehicle V according to :

$$V_a = (1 - \omega)V \tag{A.27}$$

where ω is the wake fraction number, and ω=0.1 is used in this study.

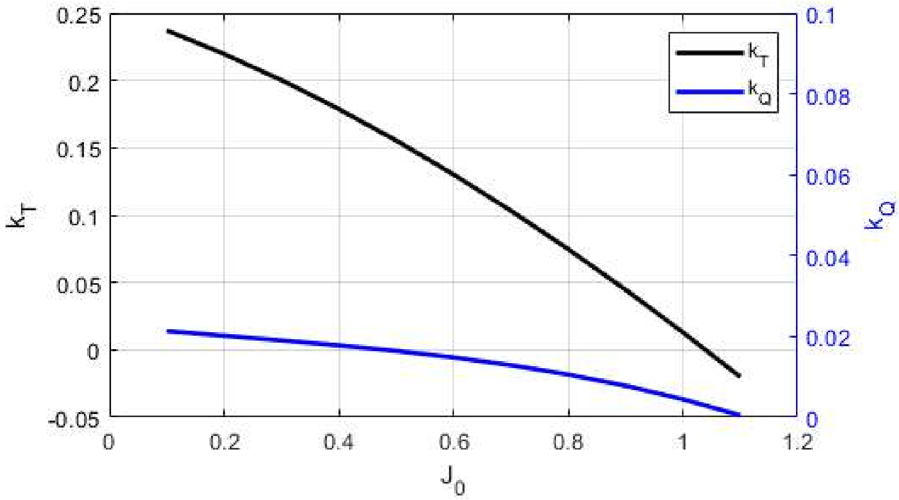

Figure A.11: $k_T$curve as a function of J_0.

BIBLIOGRAPHY

[1] E. Kim, S. Fan, and N. Bose. “Estimating Water Current Velocities by Using a Model-Based High-Gain Observer for an Autonomous Underwater Vehicle”. In: *IEEE Access* 6 (2018), pp. 70259–70271. ISSN: 2169-3536.

[2] E. Kim, S. Fan, and N. Bose. “Autonomous Underwater Vehicle Model-Based High-Gain Observer for Ocean Current Estimation”. In: *2018 IEEE/OES Autonomous Underwater Vehicle Workshop (AUV)*. 2018, pp. 1–6.

[3] E. Kim et al. “Path Following for an Autonomous Underwater Vehicle (AUV) by Using a High-Gain Observer based on an AUV Dynamic Model”. In: *The 12th IFAC Conference on Control Applications in Marine Systems, Robotics, and Vehicles (CAMS 2019)*. Vol. 52. 21. 2019, pp. 218–223. DOI: https://doi.org/10.1016/j.ifacol.2019.12.310. URL: http://www.sciencedirect.com/science/article/pii/S2405896319321950.

[4] Eonjoo Kim et al. “Current Estimation and Path Following for an Autonomous Underwater Vehicle (AUV) by Using a High-gain Observer Based on an AUV Dynamic Model”. In: *International Journal of Control, Automation and Systems* (2020). ISSN: 2005-4092. DOI: 10.1007/s12555-019-0673-5. URL: https://doi.org/10.1007/s12555-019-0673-5.

[5] D. Richard Blidberg. “The Development of Autonomous Underwater Vehicles (AUV); A Brief Summary”. In: 2001.

[6] M. Breivik and T. I. Fossen. “Guidance-based path following for autonomous underwater vehicles”. In: *Proceedings of OCEANS 2005 MTS/IEEE*. 2005, 2807–2814 Vol. 3.

[7] M. L. Seto. “Application of On-Board Evolutionary Algorithms to Underwater Robots to Optimally Replan Missions with Energy Constraints”. In: *Journal of Robotics* 2012 (2012), p. 542124. ISSN: 1687-9600. DOI: 10.1155/2012/542124. URL: https://doi.org/10.1155/2012/542124.

[8] Mohammadreza Bayat et al. “Range-based underwater vehicle localization in the presence of unknown ocean currents: Theory and experiments”. In: *IEEE Transactions on control systems technology* 24.1 (2015), pp. 122–139.

[9] Keith Vickery. “Acoustic positioning systems. A practical overview of current systems”. In: *Proceedings of the 1998 Workshop on Autonomous Underwater Vehicles (Cat. No. 98CH36290)*. IEEE. 1998, pp. 5–17.

[10] James C Kinsey, Ryan M Eustice, and Louis L Whitcomb. "A survey of underwater vehicle navigation: Recent advances and new challenges". In: *IFAC Conference of Manoeuvering and Control of Marine Craft*. Vol. 88. Lisbon. 2006, pp. 1–12.

[11] Thor I. Fossen. "Models for Ships, Offshore Structures and Underwater Vehicles". In: *Handbook of marine craft hydrodynamics and motion control*. 2011. URL: http://www.books24x7.com/marc.asp?bookid=41700.

[12] Bjørn Jalving et al. "DVL velocity aiding in the HUGIN 1000 integrated inertial navigation system". In: (2004).

[13] Lashika Medagoda et al. "Water column current profile aided localisation for autonomous underwater vehicles". In: *OCEANS'10 IEEE SYDNEY*. IEEE. 2010, pp. 1–10.

[14] S. Fan et al. "Nonlinear observer design for current estimation based on underwater vehicle dynamic model". In: *OCEANS 2016 - Shanghai*. 2016, pp. 1–5.

[15] Bruce Butler. *Into the Labyrinth: The Making of a Modern-Day*. Nov. 15, 2018.

[16] Shuangshuang Fan and Craig A. Woolsey. "Dynamics of underwater gliders in currents". In: *Ocean Engineering* 84 (2014), pp. 249 –258. ISSN: 0029-8018. DOI: https://doi.org/10.1016/j.oceaneng.2014.03.024. URL: http://www.sciencedirect.com/science/article/pii/S0029801814001139.

[17] Sungsu Park. "Design of Three-Dimensional Path Following Guidance Logic". In: *International Journal of Aerospace Engineering* (2018).

[18] L. Medagoda et al. "Water column current aided localisation for significant horizontal trajectories with Autonomous Underwater Vehicles". In: *OCEANS'11 MTS/IEEE KONA*. 2011, pp. 1–10.

[19] S. A. T. Randeni P. et al. "Parameter identification of a nonlinear model: replicating the motion response of an autonomous underwater vehicle for dynamic environments". In: *Nonlinear Dynamics* 91.2 (Jan. 2018), pp. 1229–1247. ISSN: 1573-269X. URL: https://doi.org/10.1007/s11071-017-3941-z.

[20] Mustafa Dinc and Chingiz Hajiyev. "Integration of navigation systems for autonomous underwater vehicles". In: *Journal of Marine Engineering & Technology* 14.1 (Jan. 2015), pp. 32–43. ISSN: 2046-4177. DOI: 10.1080/20464177.2015.1022382. URL: https://doi.org/10.1080/20464177.2015.1022382.

[21] O. Hegrenas, E. Berglund, and O. Hallingstad. "Model-aided inertial navigation for underwater vehicles". In: *2008 IEEE International Conference on Robotics and Automation*. 2008, pp. 1069–1076.

[22] A. Hegrenaes and O. Hallingstad. "Model-Aided INS With Sea Current Estimation for Robust Underwater Navigation". In: *IEEE Journal of Oceanic Engineering* 36.2 (2011), pp. 316–337. ISSN: 2373-7786.

[23] P. S.A.T. Randeni et al. "Numerical investigation of the hydrodynamic interaction between two underwater bodies in relative motion". In: *Applied Ocean Research* 51 (June 2015), pp. 14–24. ISSN: 0141-1187. URL: http://www.sciencedirect.com/science/article/pii/S0141118715000279.

[24] Xiao Liang et al. "Nonlinear dynamics modeling and performance prediction for underactuated AUV with fins". English. In: *Nonlinear Dynamics* 84.1 (2016), pp. 237–249. DOI: 10.1007/s11071-015-2442-1.

[25] Zheping Yan et al. "Recursive Subspace Identification of AUV Dynamic Model under General Noise Assumption". In: *Mathematical Problems in Engineering* 2014 (2014), p. 10. DOI: 10.1155/2014/547539. URL: http://dx.doi.org/10.1155/2014/547539.

[26] Lennart Ljung. *System identification : theory for the user*. Prentice Hall information and system sciences series. Upper Saddle River, NJ : Prentice Hall PTR, c1999. 2nd ed., 1999. ISBN: 0136566952. URL: https://login.ezproxy.utas.edu.au/login?url=http://search.ebscohost.com/login.aspx?direct=true&db=cat02831a&AN=UTas.b1479143&site=eds-live.

[27] P. Supun Randeni et al. "Determining the Horizontal and Vertical Water Velocity Components of a Turbulent Water Column Using the Motion Response of an Autonomous Underwater Vehicle". In: *Journal of Marine Science and Engineering* 5.3 (2017), p. 25. ISSN: 2077-1312. URL: http://www.mdpi.com/2077-1312/5/3/25.

[28] K. Reif and R. Unbehauen. "The extended Kalman filter as an exponential observer for nonlinear systems". In: *IEEE Transactions on Signal Processing* 47.8 (1999), pp. 2324–2328. ISSN: 1941-0476.

[29] S. J. Julier and J. K. Uhlmann. "Unscented filtering and nonlinear estimation". In: *Proceedings of the IEEE* 92.3 (2004), pp. 401–422. ISSN: 1558-2256.

[30] J. Carpenter, P. Clifford, and P. Fearnhead. "Improved particle filter for nonlinear problems". In: *IEE Proceedings - Radar, Sonar and Navigation* 146.1 (1999), pp. 2–7. ISSN: 1350-2395.

[31] Binqi Zheng et al. "A Robust Adaptive Unscented Kalman Filter for Nonlinear Estimation with Uncertain Noise Covariance". In: *Sensors* 18.3 (2018), p. 808. ISSN: 1424-8220. URL: http://www.mdpi.com/1424-8220/18/3/808.

[32] H. K. Khalil. "High-gain observers in nonlinear feedback control". In: *2008 International Conference on Control, Automation and Systems*. 2008, pp. xlvii–lvii.

[33] Hassan K. Khalil. "Cascade high-gain observers in output feedback control". In: *Automatica* 80 (June 2017), pp. 110–118. ISSN: 0005-1098. URL: http://www.sciencedirect.com/science/article/pii/S000510981730105X.

[34] C. Treagle, M. Farza, and M. M'Saad. "A simple filtered high gain observer for a class of uncertain nonlinear systems". In: *2017 18th International Conference on Sciences and Techniques of Automatic Control and Computer Engineering (STA)*. 2017, pp. 396–401.

[35] Angelo Alessandri and Anna Rossi. "Time-varying increasing-gain observers for nonlinear systems". In: *Automatica* 49.9 (Sept. 2013), pp. 2845–2852. ISSN: 0005-1098. URL: http://www.sciencedirect.com/science/article/pii/S0005109813003099.

[36] Jeremy G. VanAntwerp and Richard D. Braatz. "A tutorial on linear and bilinear matrix inequalities". In: *Journal of Process Control* 10.4 (Aug. 2000), pp. 363–385.

ISSN: 0959-1524. URL: http://www.sciencedirect.com/science/article/pii/S0959152499000566.

[37] D. Rudolph and T. A. Wilson. "Doppler Velocity Log theory and preliminary considerations for design and construction". In: *2012 Proceedings of IEEE Southeastcon.* 2012, pp. 1–7. DOI: 10.1109/SECon.2012.6196918.

[38] Timothy Prestero. "Verification of a six-degree of freedom simulation model for the REMUS autonomous underwater vehicle". Thesis. Massachusetts Institute of Technology. Dept. of Ocean Engineering., 2001. URL: http://hdl.handle.net/1721.1/65068.

[39] H. Porgilsson. "Control of a small undermanned underwater vehicle using zero optimizing controllers". Thesis. Master's thesis, Department of Electrical and Computer Engineering, University of Iceland, Reykjavík, Iceland, 2006.

[40] MathWorks. *LMI Applications.* 2018. URL: https://www.mathworks.com/help/robust/ug/lmi-applications.html?searchHighlight=lmi&s_tid=doc_srchtitle.

[41] Peter G. Thomasson. "Equations of Motion of a Vehicle in a Moving Fluid". In: *Journal of Aircraft* 37.4 (2000), pp. 630–639. DOI: 10.2514/2.2645. URL: https://arc.aiaa.org/doi/abs/10.2514/2.2645.

[42] C. Woolsey. *Vehicle Dynamics in Currents.* Report. Virginia Polytechnic Institute and State University, 2011.

[43] Jean-Paul Gauthier and Ivan Kupka. *Deterministic Observation Theory and Applications.* Cambridge: Cambridge University Press, 2001. DOI: 10.1017/cbo9780511546648. URL: https://www.cambridge.org/core/books/deterministic-observation-theory-and-applications/13100E3A17F8003F8297696E1E174D82.

[44] P. G. Thomasson and C. A. Woolsey. "Vehicle Motion in Currents". In: *IEEE Journal of Oceanic Engineering* 38.2 (2013), pp. 226–242. ISSN: 2373-7786.

[45] Angelo Alessandri and Anna Rossi. "Increasing-gain observers for nonlinear systems: Stability and design". In: *Automatica* 57 (July 2015), pp. 180–188. ISSN: 0005-1098. URL: http://www.sciencedirect.com/science/article/pii/S0005109815001685.

[46] Xianbo Xiang, Caoyang Yu, and Qin Zhang. "On intelligent risk analysis and critical decision of underwater robotic vehicle". In: *Ocean Engineering* 140 (Aug. 2017), pp. 453–465. ISSN: 0029-8018. URL: http://www.sciencedirect.com/science/article/pii/S0029801817303153.

[47] Zewei Zheng, Linping Ruan, and Ming Zhu. "Output-constrained tracking control of an underactuated autonomous underwater vehicle with uncertainties". In: *Ocean Engineering* 175 (Mar. 2019), pp. 241–250. ISSN: 0029-8018. URL: http://www.sciencedirect.com/science/article/pii/S0029801818314653.

[48] Thor I. Fossen and Kristin Y. Pettersen. "On uniform semiglobal exponential stability (USGES) of proportional line-of-sight guidance laws". In: *Automatica* 50.11 (Nov. 2014), pp. 2912–2917. ISSN: 0005-1098. URL: http://www.sciencedirect.com/science/article/pii/S0005109814003999.

[49] E. Borhaug, A. Pavlov, and K. Y. Pettersen. “Integral LOS control for path following of underactuated marine surface vessels in the presence of constant ocean currents”. In: *2008 47th IEEE Conference on Decision and Control.* 2008, pp. 4984–4991. ISBN: 0191-2216. DOI: 10.1109/CDC.2008.4739352.

[50] Walter Caharija et al. “Topics on Current Compensation for Path Following Applications of Underactuated Underwater Vehicles”. In: vol. 45. 5. 2012, pp. 184–191. DOI: https://doi.org/10.3182/20120410-3-PT-4028.00031. URL: http://www.sciencedirect.com/science/article/pii/S1474667016306000.

[51] W. Caharija et al. “Path following of underactuated autonomous underwater vehicles in the presence of ocean currents”. In: *2012 IEEE 51st IEEE Conference on Decision and Control (CDC).* 2012, pp. 528–535.

[52] Walter Caharija et al. “A Comparison Between the ILOS Guidance and the Vector Field Guidance”. In: *IFAC-PapersOnLine* 48.16 (Jan. 2015), pp. 89–94. ISSN: 2405-8963. URL: http://www.sciencedirect.com/science/article/pii/S2405896315021540.

[53] T. I. Fossen, K. Y. Pettersen, and R. Galeazzi. “Line-of-Sight Path Following for Dubins Paths With Adaptive Sideslip Compensation of Drift Forces”. In: *IEEE Transactions on Control Systems Technology* 23.2 (2015), pp. 820–827. ISSN: 2374-0159.

[54] W. Caharija et al. “Integral Line-of-Sight Guidance and Control of Underactuated Marine Vehicles: Theory, Simulations, and Experiments”. In: *IEEE Transactions on Control Systems Technology* 24.5 (2016), pp. 1623–1642. ISSN: 2374-0159.

[55] Thor I. Fossen and Anastasios M. Lekkas. “Direct and indirect adaptive integral line-of-sight path-following controllers for marine craft exposed to ocean currents”. In: *International Journal of Adaptive Control and Signal Processing* 31.4 (2017), pp. 445–463. DOI: 10.1002/acs.2550. eprint: https://onlinelibrary.wiley.com/doi/pdf/10.1002/acs.2550. URL: https://onlinelibrary.wiley.com/doi/abs/10.1002/acs.2550.

[56] Guanxue Wang et al. “Fuzzy Iterative Sliding Mode Control Applied for Path Following of an Autonomous Underwater Vehicle with Large Inertia”. In: *Mathematical Problems in Engineering* 2019 (2019), p. 14. DOI: 10.1155/2019/8650243. URL: https://doi.org/10.1155/2019/8650243.

[57] Dennis Belleter et al. “Observer based path following for underactuated marine vessels in the presence of ocean currents: A global approach”. In: *Automatica* 100 (Feb. 2019), pp. 123–134. ISSN: 0005-1098. URL: http://www.sciencedirect.com/science/article/pii/S0005109818305405.

[58] S. Moe et al. “Path following of underactuated marine surface vessels in the presence of unknown ocean currents”. In: *2014 American Control Conference.* 2014, pp. 3856–3861.

[59] Even Borhaug and Kristin Y. Pettersen. “LOS path following for underactuated underwater vehicle”. In: *7th IFAC Conference on Manoeuvring and Control of Marine Craft.* 2006, pp. 20–22.

[60] Yu-lei Liao, Ming-jun Zhang, and Lei Wan. “Serret-Frenet frame based on path following control for underactuated unmanned surface vehicles with dynamic uncertainties”.

In: *Journal of Central South University* 22.1 (Jan. 2015), pp. 214–223. ISSN: 2227-5223. URL: https://doi.org/10.1007/s11771-015-2512-z.

[61] Xiao Liang et al. “Three-dimensional path following control of underactuated autonomous underwater vehicle based on damping backstepping”. In: *International Journal of Advanced Robotic Systems* 14.4 (Feb. 2017), p. 1729881417724179. ISSN: 1729-8814. DOI: 10.1177/1729881417724179. URL: https://doi.org/10.1177/1729881417724179.

[62] Peter Thomasson. “Equations of Motion of a Vehicle in a Moving Fluid”. In: *Journal of Aircraft - J AIRCRAFT* 37 (July 2000), pp. 630–639.

[63] Yingkai Xia et al. “Improved line-of-sight trajectory tracking control of under-actuated AUV subjects to ocean currents and input saturation”. In: *Ocean Engineering* 174 (Feb. 2019), pp. 14–30. ISSN: 0029-8018. URL: http://www.sciencedirect.com/science/article/pii/S0029801818317281.

[64] Katsuhiko Ogata. *Modern Control Engineering*. Prentice Hall PTR, 2001, p. 964. ISBN: 0130609072.

[65] Guangjie Zhang et al. “High-gain observer-based model predictive control for cross tracking of underactuated autonomous underwater vehicles”. In: *2016 IEEE International Conference on Underwater System Technology: Theory and Applications (USYS)*. 2016, pp. 115–120.

[66] A. Alessandri. “Design of observers for lipschitz nonlinear systems using LMI”. In: *IFAC Proceedings Volumes* 37.13 (Sept. 2004), pp. 459–464. ISSN: 1474-6670. URL: http://www.sciencedirect.com/science/article/pii/S1474667017312661.

[67] Signe Moe. “Guidance and Control of Robot Manipulators and Autonomous Marine Robots”. Thesis. Faculty of Information Technology, Norwegian University of Science and Technology, 2016.

[68] S. Fan and C. A. Woolsey. “Underwater vehicle control and estimation in nonuniform currents”. In: *2013 American Control Conference*. 2013, pp. 1400–1405. ISBN: 0743-1619. DOI: 10.1109/ACC.2013.6580032.

[69] S. Fan et al. “Impact of Current Disturbances on AUV Docking: Model-Based Motion Prediction and Countering Approaches”. In: *IEEE Journal of Oceanic Engineering* 43.4 (2018), pp. 888–904. ISSN: 2373-7786.

[70] Derek A. Fong and Nicole L. Jones. “Evaluation of AUV-based ADCP measurements”. In: *Limnol. Oceanogr. Methods.* 4.3 (Feb. 2006), pp. 58–67. ISSN: 1541-5856. DOI: 10.4319/lom.2006.4.58. URL: https://doi.org/10.4319/lom.2006.4.58.

[71] Gene F. Franklin, David J. Powell, and Abbas Emami-Naeini. *Feedback Control of Dynamic Systems*. 4th. USA: Prentice Hall PTR, 2001. ISBN: 0130323934.

[72] Farhood Azarsina and Christopher D. Williams. “Manoeuvring simulation of the MUN Explorer AUV based on the empirical hydrodynamics of axi-symmetric bare hulls”. In: *Applied Ocean Research* 32.4 (Oct. 2010), pp. 443–453. ISSN: 0141-1187. URL: http://www.sciencedirect.com/science/article/pii/S014111871000074X.

[73] M. T. Issac et al. “Manoeuvring Trials with the MUN Explorer AUV: Data Analysis and Observations”. In: *OCEANS 2007*. 2007, pp. 1–8.

[74] Gps Nautical Chart. *HOLYROOD Marine Chart.* 2020. URL: http://www.gpsnauticalcharts.com/main.

[75] Manoj Thomas Issac. "Analysis of full-scale sea-trials manoeuvring data and development and validation of a motion-simulation model for the AUV MUN Explorer". PhD thesis. Memorial University of Newfoundland, 2011.

[76] Douglas Edward Perrault. "Autonomous underwater vehicles (AUV) sensitivity of motion response to geometric and hydrodynamic parameters and AUV behaviours with control plane faults". PhD thesis. Memorial University of Newfoundland, 2002.

[77] Jason Evans and Meyer Nahon. "Dynamics modeling and performance evaluation of an autonomous underwater vehicle". In: *Ocean Engineering* 31.14 (2004), pp. 1835 –1858. ISSN: 0029-8018. DOI: https://doi.org/10.1016/j.oceaneng.2004.02.006. URL: http://www.sciencedirect.com/science/article/pii/S0029801804000708.

[78] Mohinder S. Grewal, Lawrence R. Weill, and Angus P. Andrews. *Global Positioning Systems, Inertial Navigation, and Integration.* USA: Wiley-Interscience, 2007. ISBN: 0470041900.

[79] Thor I. Fossen. *Guidance and control of ocean vehicles.* English. Includes bibliographical references (p. [455]-474) and index. Chichester ; New York : Wiley, 1994. ISBN: 0471941131.

[80] John Nicholas Newman. *Marine hydrodynamics / J. N. Newman.* English. MIT Press Cambridge, Mass, 1977, xiii, 402 p. : ISBN: 0262140268.

[81] George D. Watt. "Estimates for the Added Mass of a Multi-Component, Deeply Submerged Vehicle. Part 1. Theory and Program Description". In: 1988.

[82] E. Hayashi et al. "Customizing an Autonomous Underwater Vehicle and developing a launch and recovery system". In: *2013 IEEE International Underwater Technology Symposium (UT).* 2013, pp. 1–7. DOI: 10.1109/UT.2013.6519831.

[83] M. T. Issac et al. "Manoeuvring Experiments Using the MUN Explorer AUV". In: *2007 Symposium on Underwater Technology and Workshop on Scientific Use of Submarine Cables and Related Technologies.* 2007, pp. 256–262.

[84] Y. Goh and S. Fan. "Path Planning for AUV Area Coverage Mission based on MOOS-IvP". In: *2019 IEEE Underwater Technology (UT).* 2019, pp. 1–10. DOI: 10.1109/UT.2019.8734467.

[85] Paul Zarchan. *Tactical and strategic missile guidance.* Fourth edition. Reston, Va. : American Institute of Aeronautics and Astronautics, [2002] ©2002, 2002. URL: https://search.library.wisc.edu/catalog/999939176902121.

[86] P. Encarnacao and A. Pascoal. "Combined trajectory tracking and path following: an application to the coordinated control of autonomous marine craft". In: *Proceedings of the 40th IEEE Conference on Decision and Control (Cat. No.01CH37228).* Vol. 1. 2001, 964–969 vol.1. DOI: 10.1109/CDC.2001.980234.

[87] Sanghyuk Park, John J. Deyst, and Jonathan P. How. "A New Nonlinear Guidance Logic for Trajectory Tracking". In: 2004.

[88] P. Vandrish et al. "Side-scan sonar image registration for AUV navigation". In: *2011 IEEE Symposium on Underwater Technology and Workshop on Scientific Use of Submarine Cables and Related Technologies*. 2011, pp. 1–7. DOI: 10.1109/UT.2011.5774096.

[89] R. Stokey et al. "Very shallow water mine countermeasures using the REMUS AUV: a practical approach yielding accurate results". In: *MTS/IEEE Oceans 2001. An Ocean Odyssey. Conference Proceedings (IEEE Cat. No.01CH37295)*. Vol. 1. 2001, 149–156 vol.1. DOI: 10.1109/OCEANS.2001.968696.

[90] A. S. Gadre and D. J. Stilwell. "A complete solution to underwater navigation in the presence of unknown currents based on range measurements from a single location". In: *2005 IEEE/RSJ International Conference on Intelligent Robots and Systems*. 2005, pp. 1420–1425. DOI: 10.1109/IROS.2005.1545230.

[91] E. Wolbrecht et al. "Estimating and compensating for water currents: Field testing". In: *OCEANS 2016 MTS/IEEE Monterey*. 2016, pp. 1–5. DOI: 10.1109/OCEANS.2016.7761364.

[92] J. Vaganay, P. Baccou, and B. Jouvencel. "Homing by acoustic ranging to a single beacon". In: *OCEANS 2000 MTS/IEEE Conference and Exhibition. Conference Proceedings (Cat. No.00CH37158)*. Vol. 2. 2000, 1457–1462 vol.2. DOI: 10.1109/OCEANS.2000.881809.

[93] J. Osborn et al. "AUV state estimation and navigation to compensate for ocean currents". In: *OCEANS 2015 - MTS/IEEE Washington*. 2015, pp. 1–5. DOI: 10.23919/OCEANS.2015.7401906.

[94] K. Myers and B. Tapley. "Adaptive sequential estimation with unknown noise statistics". In: *IEEE Transactions on Automatic Control* 21.4 (1976), pp. 520–523. ISSN: 1558-2523. DOI: 10.1109/TAC.1976.1101260.

[95] Vinay A. Bavdekar, Anjali P. Deshpande, and Sachin C. Patwardhan. "Identification of process and measurement noise covariance for state and parameter estimation using extended Kalman filter". In: *Journal of Process Control* 21.4 (2011), pp. 585 – 601. ISSN: 0959-1524. DOI: https://doi.org/10.1016/j.jprocont.2011.01.001. URL: http://www.sciencedirect.com/science/article/pii/S0959152411000023.

[96] Marian Muste, Dongsu Kim, and Juan A. González-Castro. "Near-Transducer Errors in ADCP Measurements: Experimental Findings". In: *Journal of Hydraulic Engineering* 136.5 (2010), pp. 275–289. DOI: doi:10.1061/(ASCE)HY.1943-7900.0000173.

[97] Planet Ocean Ltd. *TRIAXYS DIRECTIONAL WAVE BUOYwith currents*. 2007. URL: http://www.planet-ocean.co.uk/PDF/TRIAXYS.pdf.

[98] Eric Davis. In: 2019.

[99] Ocean Networks Canada. *Data Tools*. 2020. URL: https://www.oceannetworks.ca/DATA-TOOLS.

[100] Adam Schneider, ed. *GPS Visualizer*. 2020. URL: https://www.gpsvisualizer.com/map_input?form=data.

[101] Airfoil Tools. *NACA 0024 - NACA 0024 airfoil.* 2020. URL: `http://airfoiltools.com/airfoil/details?airfoil=naca0024-il`.

[102] W. Kenneth. Bullivant. *Tests of the NACA 0025 and 0035 airfoils in the full-scale windtunnel. NACA report No. 708.* Report. Langley Memorial Aeronautical Laboratory, 1941.

[103] R. Von Mises et al. *Theory of Flight.* Dover Publications, 1959. URL: `https://books.google.fm/books?id=CRcOAAAAMAAJ`.

[104] Mogens Blanke. "Ship propulsion losses related to automatic steering and prime mover control". Thesis. The Technical University of Denmark, Lyngby, 1981.